catalysts

MDPI

Review

Recent Advancements and Future Prospects in Ultrathin 2D Semiconductor-Based Photocatalysts for Water Splitting

Xiaoyong Yang [1], Deobrat Singh [1] and Rajeev Ahuja [1,2,*]

[1] Condensed Matter Theory Group, Materials Theory Division, Department of Physics and Astronomy, Uppsala University, Box 516, 75120 Uppsala, Sweden; xiaoyong.yang@physics.uu.se (X.Y.); deobrat.singh@physics.uu.se (D.S.)

[2] Applied Materials Physics, Department of Materials Science and Engineering, Royal Institute of Technology (KTH), S-100 44 Stockholm, Sweden

* Correspondence: rajeev.ahuja@physics.uu.se

Received: 23 August 2020; Accepted: 21 September 2020; Published: 25 September 2020

Abstract: Ultrathin two-dimensional (2D) semiconductor-mediated photocatalysts have shown their compelling potential and have arguably received tremendous attention in photocatalysis because of their superior thickness-dependent physical, chemical, mechanical and optical properties. Although numerous comprehensions about 2D semiconductor photocatalysts have been amassed up to now, low cost efficiency, degradation, kinetics of charge transfer along with recycling are still the big challenges to realize a wide application of 2D semiconductor-based photocatalysis. At present, most photocatalysts still need rare or expensive noble metals to improve the photocatalytic activity, which inhibits their commercial-scale application extremely. Thus, developing less costly, earth-abundant semiconductor-based photocatalysts with efficient conversion of sunlight energy remains the primary challenge. In this review, it begins with a brief description of the general mechanism of overall photocatalytic water splitting. Then a concise overview of different types of 2D semiconductor-mediated photocatalysts is given to figure out the advantages and disadvantages for mentioned semiconductor-based photocatalysis, including the structural property and stability, synthesize method, electrochemical property and optical properties for H_2/O_2 production half reaction along with overall water splitting. Finally, we conclude this review with a perspective, marked on some remaining challenges and new directions of 2D semiconductor-mediated photocatalysts.

Keywords: ultrathin semiconductor-based photocatalysts; hydrogen evolution reaction; oxygen evolution reaction; overall water splitting

1. Introduction

Nowadays, the biggest technological challenges for human beings are the increasing consumption of resources and energy and the related environmental pollution problem all over the world. For example, the worldwide energy consumption will expect to reach up to 815 quadrillion Btu in 2040 due to the growing global production and population [1,2]. However, the huge energy resources in the earth mainly originate from non-renewable coal, oil, natural gas and nuclear energy, and their reserves are limited. Although the energy is released by combustion on the application of these fossil fuels, a series of critical environmental problems—water contamination, greenhouse gas emissions, global warming and the emergence of a hole in the ozone layer—occur at the same time. Thus, lots of scientists, politicians, industry groups are encouraged to seek new and sustainable alternative energy resources. Every day the sun radiates an enormous amount of energy for our planet, which has attracted great attention as a promising alternative energy source for cutting greenhouse

gas emissions and providing the current and future human energy demand. However, it is not nearly sufficient, therefore, the harvest and conversion of solar energy into other kinds of energy is a priority to resolve [3–5]. At present, photovoltaic cells are already a popular sight on rooftops to directly convert solar energy into electricity. However, electricity presents its own challenges in that it would have to be used immediately or be stored in a secondary device at a high energy density, such as capacitors or batteries. In comparison with converting solar energy into electricity, synthesizing storable, transportable chemical fuels via photocatalytic processes would be a more attractive approach, in which the harnessing of energy in sunlight would be stored in the form of molecular bonds through a thermodynamic "uphill reaction" (see Equation (1)). Up to now, a photocatalysis technique has been used in different application fields, such as water splitting to produce hydrogen [6,7], sterilization [8], wastewater treatment and self-cleaning materials [9], decomposition of crude spills [10,11], dye-sensitized solar cell and inactivation of cancer cells [12,13].

Hydrogen (H_2) is a clean and carbon-free fuel with high specific enthalpy. Whereas, until now, around 95% of the world's hydrogen fuel is mainly sourced from natural gas, by reacting methane with steam using fossil fuel to produce hydrogen and carbon dioxide (CO_2). Thus the production of hydrogen from methane is a kind of fossil fuel product rather than renewable energy. The critical method to utilize hydrogen production is developing an effective H_2-preparation approach without ever seeing fossil fuels. The method using photocatalytic materials to produce hydrogen has been demonstrated since 1972 according to the following reaction equation,

$$2H_2O \rightarrow 2H_2 + O_2, \quad (1)$$

$$\Delta E^0 = 1.23 \text{ eV}, \ \Delta G^0 = +237.2 \text{ kJ mol}^{-1},$$

This photocatalytic process is driven by a thermodynamic "uphill reaction" of solar energy with a large change of ΔG^0 = 1.23 eV (237.13 kJ mol^{-1}) per photon [14]. Here, the photocatalytic materials require four electron generations according to Equation (2) to endure this reaction of water,

$$2H_2O \rightarrow 4H^+ + 4e^- + O_2, \quad (2)$$

$$\text{NHE, pH} = 0, \textit{vs}. \ \Delta E^0 = 237.13 \text{ kJ mol}^{-1}$$

$$4H^+ + 4e^- \rightarrow 2H_2, \quad (3)$$

$$\text{NHE, pH} = 0, \textit{vs}. \ \Delta E^0 = 0 \text{ kJ mol}^{-1}$$

Therefore, the surface of the photocatalytic materials should be struck using a suitable energy with the corresponding photons. The estimated solar photon flux density (Q) is 2000 μmol $s^{-1}m^{-2}$ [15]. While the previous reports found the holes took less than 2 μs to react with the water vapor while the oxygen took 10–100 μs to capture the electrons in P25 TiO_2 [15,16], thus, gaining the solar photon flux of photocatalytic materials is a big challenge. Since Honda and Fujishima firstly discovered the Pt/TiO_2 electrode could be used to complete the water splitting reaction to generate H_2, utilizing artificial photosynthesis producing solar hydrogen production has become a promising strategy for converting and storing solar energy into chemical H_2 fuel [17]. To date, numerous efforts have been devoted to realizing photocatalytic H_2 production from water, including semiconductor-based heterogeneous systems [1,18–25], molecular material-based homogeneous systems [26–30], and organic-inorganic hybrid systems [31–33]. Subsequently, the research field is also expanding fast and attracting lots of scientists from chemistry and material science to physics and computational science. For example, chemists devote themselves to developing molecular photosensitizers and catalysts as well as

establishing the relationship between the structure of materials and the corresponding property for H_2 production systems [34–37]. For material scientists, they try their best to design and synthesize new architecture materials with high photocatalytic performance [38–40]. With regard to physicists, they focus themselves on dealing with the fundamental physical mechanisms of semiconductor-based heterogeneous photocatalysts and reduce the recombination of photon-electron pairs as well as their traveling distance [41–43]. This natural synergy could help in the development of materials science and generate big future for renewable energy.

There are three major steps to an overall photocatalytic split water for a semiconductor photocatalyst: (1) the absorption of photons on the surface of a semiconductor, with appropriate energy, which can stimulate electron transfer to the conduction band position from the valence band position and generate electron-hole pairs ($e^- - h^+$), (2) the separation and migration of charge carriers on the surface of the material at a short span of time; (3) the impingement between the corresponding free electrons and holes on the surface of the system to complete the water splitting reaction to generate H_2 or O_2, as depicted in Figure 1. Whereas, the recombination of the free electrons and the excited holes may readily happen in the second step, giving rise to a poor photocatalytic activity of the nanocrystal surface. Accordingly, the suitable bandgap and the corresponding levels of the conduction and valence bands could aid the light absorption on the surface of the semiconductor photocatalyst, even at a low solar energy flux density. In general, when semiconductor-based photocatalysts show a more negative level of the bottom of the conduction band than the reduction potential of H^+/H_2 (0 V vs. NHE, pH = 0) and a more positive level of the top of the valance band than the oxidation potential of O_2/H_2O (1.23 V vs. NHE, pH = 0), the photocatalysis of water is more thermodynamically feasible [44,45]. It should be mentioned that the extreme challenge for the overall process of photocatalytic water splitting is to reduce the recombination of four-electron-four-hole as well as shorten their traveling distance [46,47]. Equations (2) and (3) are the standard half-reactions for H_2 and O_2 evolution, respectively, the corresponding schematic illustration is shown in Figure 1. In addition, one of these half-reactions can be substituted by an appropriate sacrificial reductant in the half-reaction systems. For example, methanol [48], triethylamine [49], ethanol [50], Na_2S/Na_2SO_3 pairs [51] and triethanolamine [52] are the most commonly used sacrificial reductants. In addition, ascorbic/lactic acid [53,54], ethylene diamine tetra-acetic acid [55] and sacrificial oxidant [56] are also reported in the previous work. Over the past four decades, various semiconductor-based photocatalysts have been designed, synthesized and developed with a broader purpose to obtain a solar energy flux (step 1 in Figure 1) and efficient reduction of the charge carriers recombination, and to shorten the migration for the charge carriers (step 2 in Figure 1). For example, lots of bandgap engineering methods are applied to improve the sunlight absorption, even at a low flux density, for wide bandgap semiconductors, including ions/defects doping and forming solid solutions [57–59], hybridization with small bandgap semiconductors [60,61], disorder engineering [62], and surface plasmonic enhancement [63]. In addition, different kinds of nanostructured semiconductors have been synthesized to obtain the efficient charge separation and transportation, such as nanoparticles, porous nanospheres, nanowires, nanobelts, nanotubes and nanosheets [64,65]. It is worth mentioning that the formation of a vertical or in-plane hetero-junction using two or more than two semiconductors has been extensively explored to improve the charge carriers separation and shorten their traveling distance [66,67]. Until now, the first two steps in Figure 1 have made for a significant advancement in photocatalytic water splitting. The majority of research achievements are only efficient for either proton reduction or water oxidation. The co-photocatalysts, which could work for overall water splitting, have not been overwhelmingly investigated since the combination of a suitable bandgap, an appropriate bottom of the conduction band and an appropriate top of the valence band is difficult to engineer [68]. However, a few materials, such as $Rh_{2-y}Cr_yO_3$ [69] and Rh-Cr_2O_3 [70,71], are proposed as the most active co-catalysts. However, these noble-metal based co-catalysts can not be used in a large scale energy production because the resources of noble metals are limited. Hence, there is significance in exploring co-catalysts with low cost and high efficiency.

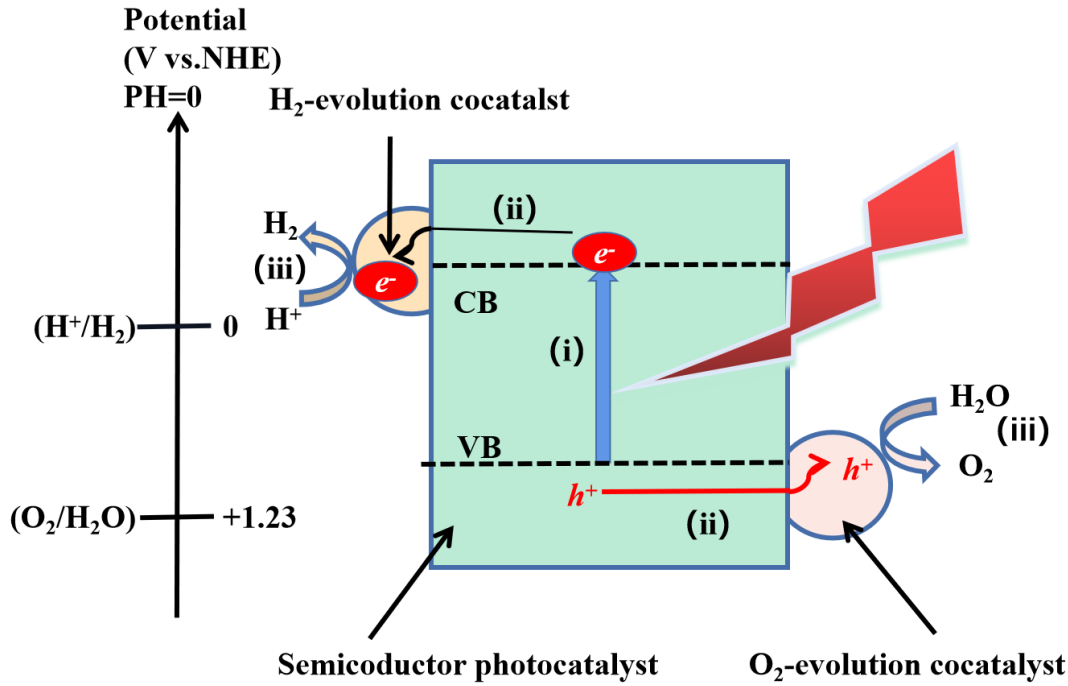

Figure 1. Schematic diagram of the three major steps of overall photocatalytic water splitting on a semiconductor photocatalyst [18].

On the other hand, nanoparticles, porous nanospheres, and nanowires have recently attracted a large amount of attention in the process of water splitting in that they possess unconventional and fancy physical and chemical properties, which may be easier to meet the requirements for overall photocatalytic splitting water compared to their bulk counterparts [30,72–76]. First, these different nanostructures could decrease the rate of charge carriers recombination and let them travel a very small distance, which largely enriches the selectivity of photocatalytic materials and paves a new path to design an effective photocatalysis. Second, 2D nanostructured photocatalysts could have more active sites for electrochemical reactions due to their larger surface areas. Third, quantum confinement effects in 2D metallic and semiconductor nanostructures dependent on size and morphology of photocatalysts could open a new approach to engineer the processes of sunlight harvesting. It is because the quantum size effects can restrict electrons in order to accommodate the additional atom, platelike nanoparticles, disk or cluster, resulting in the increasing of energy levels and HOMO-LUMO bandgap. For 1D quantum confined materials, it is found that the modification of the aspect ratio of nanorods could largely tune the optical response properties [77]. Last but not least, various 2D nanomaterials provide more sources to integrate heterogeneous structures with multiple functional properties. On the other hand, for the majority of 3D semiconductors, it is commonly ignored to distinguish the electronic and optical bandgaps due to the small exciton binding energy. While the distinction between electronic and optical bandgaps in 2D nanomaterials is significant and obvious. The Bethe–Salpeter equation is frequently used to predict the exciton binding energy and optical bandgap. Furthermore, most of the 2D materials exhibit more soft elastic constants, which could have extra application compared to bulk 3D counterparts. Particularly, the band edge positions and bandgaps are very sensitive to small strains with a significant extent, thus it could facilitate tuning the photocatalytic performance of 2D nanomaterials as photocatalysts. Herein, the current review work covers the fundamental mechanisms of overall photocatalytic water splitting and recent progress in the use of two dimensional (2D) semiconductor-based nanomaterials and their nanoheterostructure composites with a focus on the relationship between the structural property of the nanomaterials and their photocatalytic activity. It begins by introducing the various mechanisms of photoexcited carriers on different 2D semiconductor-based nanomaterials during photocatalytic overall

water splitting to provide a whole view for the principle of work on the basis of thermodynamics half-reactions. Then, we compare the general structural property, advantages in electronic and surface properties, and electrochemical performances to pursue high efficiency of water splitting on the different 2D semiconductors, including carbon nitride (g-C_3N_4), boron nitride, black phosphorus, transition metal oxides (TMOs), transition metal dichalcogenides (TMDs), MXenes, perovskite nanosheets, nanoheterostructure composites, metal organic frameworks (MOFs), covalent organic frameworks (COFs). Subsequently, some commonly used synthetic methods for 2D nanomaterials are summarized in Section 4. Toward the end, we conclude the current research status with a perspective on the challenges of 2D semiconductor-based photocatalysts for photocatalysis application.

2. Mechanisms of Overall Photocatalytic Water Splitting

In previous researches, the mechanisms of 2D and 3D materials as photocatalysts to split water have been extensively reported. With regard to semiconductors, the absorbed photon should possess a higher energy ($h\nu$) than the corresponding bandgap of the semiconductor in order to excite the electrons to the empty conduction band (CB) position from the filled valence band (VB) position of the semiconductor photocatalyst. Then the excited electrons and holes pair ($e^- - h^+$) is formed according to the following expression,

$$\text{Photonactivation}: \ \text{Semiconductor} + h\nu \rightarrow e^- + h^+, \tag{4}$$

$$\text{Oxygen adsorption}: \ (O_2)_{ads} + e^- \rightarrow O_2^{\bullet -}, \tag{5}$$

$$\text{Water ionization}: \ H_2O \rightarrow OH^- + H^+, \tag{6}$$

$$\text{Superoxide protonation}: \ O_2^{\bullet -} + H^+ \rightarrow HOO^{\bullet}. \tag{7}$$

The bandgap of a single semiconductor photocatalyst should meet the requirements of reduction reaction potential with 0 eV for catalyzing H_2O into H_2 (H^+/H_2) and oxidation reaction potential with +1.23 eV for oxidizing H_2O into O_2 (O_2/H_2O) in pH = 0 reactant solution at a normal hydrogen electrode (NHE), as shown in Figure 2a. This mechanism is called one-step water splitting. Alternatively, an appropriate water redox shuttle mediator can connect to two different semiconductors or even more to form a hybrid semiconductor. Detailedly, the H^+/H_2 reduction and O_2/H_2O oxidation can occur on two separately semiconductors in hybrid materials in order to make the photon-induced $e^- - h^+$ pairs separate and overall water splitting. This system is called the Z-scheme system [78,79].

In a system with a semiconductor electrode immersed in an electrolyte solution, the electrons transfer takes place spontaneously in order to keep the balance between the Fermi level (E_f) of the semiconductor photocatalyst and the redox potential of the electrolyte solution. Specifically, if E_f of the semiconductor photocatalyst is higher than the oxidation potential of the electrolyte solution, then the semiconductor photocatalyst will accept electrons from the electrolyte solution—and the converse is also true. It is known that, in a semiconductor, the electron density is finite but the valence band (VB) and conduction band (CB) positions at the interfaces are regarded as fixed, thus the electron transfer can cause band bending. The space charge layer could induce an intrinsic electric field, which is helpful to separate the charge [80]. For example, a n-type semiconductor can work as a photoanode for oxygen evolution, thus photon-generated holes will accumulate on the surface of the semiconductor, whereas the counter electrode will accept the corresponding electrons through an external circuit, as shown in Figure 2c [7]. In this oxidation reaction, the maximum valence band (MVB) of the photon-anode should be lower than the oxygen evolution potential of -5.67 eV by ΔE_V to allow the n-type semiconductor to generate oxygen. In contrast, the p-type semiconductors act as photocathodes for the reduction reaction to catalyze H_2O into H_2 if the minimum conduction band edge (MCB) is higher than the hydrogen evolution potential of -4.44 eV by ΔE_C, as depicted in Figure 2d. Accordingly, in both cases the excited carriers by sunlight could drive the photoelectrochemical reactions on photoanodes. While, if E_f of the counter electrode fails the redox reactions, an external

voltage can be used to compensate for the potential deficiency. It is worthy of mentioning that if the kinetic overpotential of ΔE_V or ΔE_C is larger, then the required bias voltage should be larger to make the redox reactions successful on the counter electrode. In the Z-scheme water splitting system, two different photocatalysts, i.e., photoanode and photocathode, are combined in tandem. Then the sunlight can be efficiently utilized than that in the one-step water splitting systems since the maximum energy required to drive the photoelectrodes is reduced, as shown in Figure 2e.

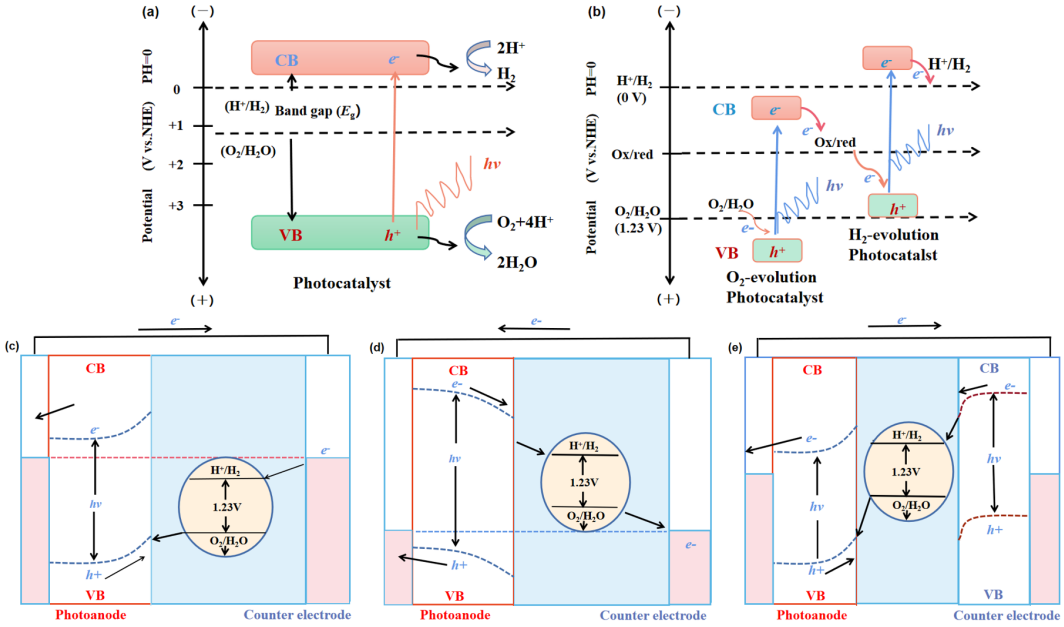

Figure 2. Energy schematic diagram based on (**a**) one-step water splitting and (**b**) Z-scheme mechanism; and photoelectrochemical water splitting using (**c**) a photoanode, (**d**) photocathode, and (**e**) photoanode and count electrode in tandem systems for photocatalytic water splitting, respectively [81].

3. Classification of 2D Semiconductors for Photocatalysts

To date, a great amount of 2D nanosheets have been synthesized by various chemical and/or physical methods, which are mainly divided into two types, layered and non-layer structural materials. With regard to layered materials, the in-plane layer is formed by connecting the in-plane atoms by strong chemical bonding. However, the weak van der Waals interaction plays an important role in stacking these monolayers to form bulk crystals [82]. The representative layered material is graphite crystal, which is stacked by many graphene layers via weak van der Waals force. In addition, nitrides (such as *g*-C_3N_4, *h*-BN, GaN, Ca_2N), black phosphorus (BP), Xenes, transition metal dichalcogenides (TMDs), transition metal oxides are also layered materials, as shown in Figure 3. The exfoliation of highly anisotropic layered materials into a 2D monolayer can use the micro-mechanical cleavage method, mechanical force-assisted liquid exfoliation method or ion intercalation-assisted liquid exfoliation, which are collectively known as top-down exfoliation methods. It is because highly anisotropic layered materials possess strong in-plane bonds in each layer with high covalent character but weakly stack the monolayers via ionic or Van der Waals interactions [82]. In contrast, other solid crystals, generally crystallized into three dimensions (3D) bulk via atomic or chemical bonding, including bulk metals, metal oxide matrices, metal chalcogenide matrices and polymers, can form 2D inorganic nanosheets by the bottom-up approach, which includes a wet-chemical route and chemical vapor deposition (CVD) [83–85]. Particularly, a variety of solid materials can be formed relying on the coordination mode and arrangement of atoms as well as the stacking orders among every monolayer [86–88]. All these factors could have a significant effect on the physical and chemical properties and functionalities of the crystal materials [86–91]. The promising ultrathin 2D photocatalysts for photocatalytic water splitting can mainly be categorized into metal-composite oxides,

metal hydroxides, TMDs, MXenes and metal-free photocatalysts, metal-organic frameworks (MOFs), covalent-organic frameworks (COFs) and so on. In this section, the crystal structural information and the photocatalysis properties of these widely explored 2D semiconductor-based photocatalysts will be detailedly introduced based on their composition.

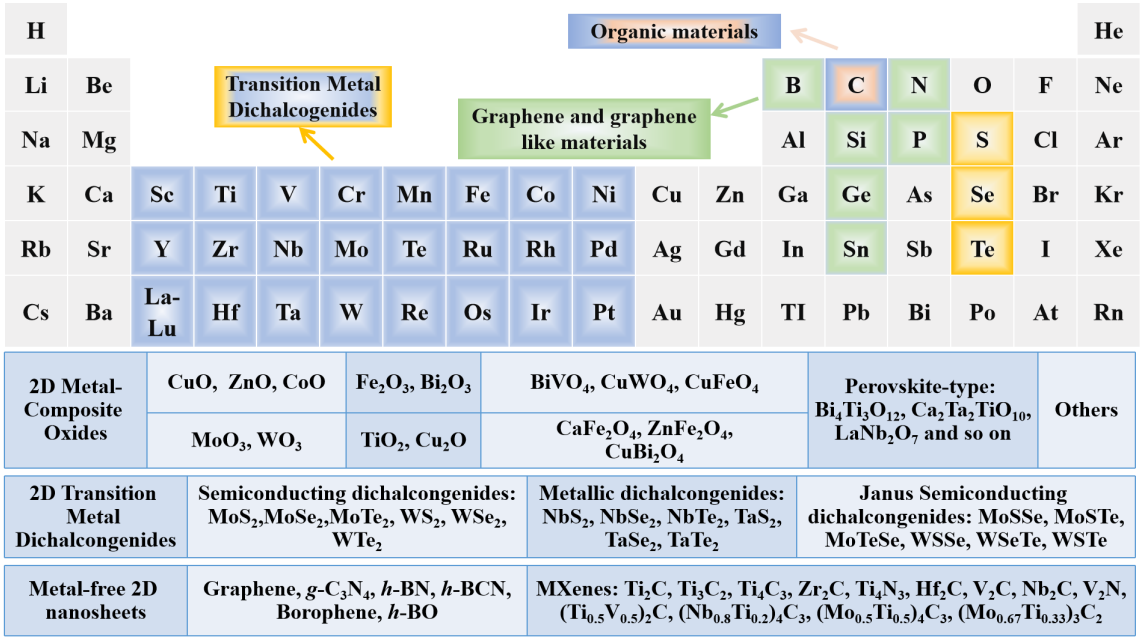

Figure 3. Periodic table with highlighted elements for typical ultrathin 2D materials.

3.1. Metal-Composite Oxides

So far, metal-composite oxides have been widely investigated as a photocatalyst to split water. Synthesizing ultrathin 2D metal-composite oxide materials via chemical bonding in three dimensions is considered as a practical and efficient method to enlarge the specific surface area for increasing the activity sets and optimizing charge carriers migration in order to achieve an efficient photocatalytic behavior. Until now, an incredible amount of metal-composite oxides with 2D structures have been successfully prepared and numerous investigations about their photocatalytic activities have been performed to seek the most efficient photocatalysts for splitting water, including TiO_2, CeO_2, ZnO, Cu_2O, WO_3, Fe_2O_3, In_2O_3, SnO_2, Mn_2O_3, Bi_2WO_6, Bi_2MoO_6, $ZnWO_4$, $BiVO_4$. Notably, these metal oxides show a different structural formula with different space group (SG), thus their structural properties and physical, chemical properties should be different to each other [92]. For example, CeO_2 exhibits a face center cubic (fcc) structure with the SG of *Fm*3*m*, in which the cations occupy the regular sites of the fcc unit cell whereas the anions occupy the eight tetrahedral interstitial sites, as shown in Figure 4a. One can see that Ce^{4+} ions are coordinated to eight equivalent anions (O^{2-}), and similarly, each O^{2-} is coordinated to 4 Ce^{4+} [93]. Comparably, MoO_3 shows an orthorhombic structure with the SG of *Pcmn*. While each layer consists of distorted MoO_6 octahedra, forming a layered structure, as shown in Figure 4c [94,95]. Furthermore, this octahedra shares the edges with its neighboring atoms for forming 2D layers via the weak van der Waals force [94,95]. In the vanadium oxide group, α-V_2O_5 is the most stable phase since the vanadium atoms exhibit a higher oxidation state [96]. In Figure 4d, one can see α-V_2O_5 shows a layered structure with the SG of *Pmmn* in which each layer is composed of a distorted trigonal bipyramidal polyhedral. In addition, the $(V_2O_4)_n$ zigzag chain is formed naturally by sharing the edges of every polyhedron along the (001) direction, giving rise to the formation of 2D layers [96,97]. However, some 2D metal-composite oxide nanosheets failed to facile synthesize by mechanical exfoliation from their parental bulk materials, which posses a nonlayer structured feature. Thus, some alternative routes are chosen for controlling the preparation

of the metal-composite oxide nanosheets. For example, ultrathin TiO_2 nanosheets can be obtained by performing a lamellar inorganic–organic hybrid intermediate approach [98]. As shown in Figures 4b and 5, through a hybridization reaction of Ti-isopropoxide and octylamine under 200 °C, the lamellar TiO_2-octylamine hybrid can be obtained. Then the clean TiO_2 flakes are acquired by washing to remove the octylamine. The average thickness of ultrathin TiO_2 could reach up to 1.66 nm in an experiment, which implies the successful preparation of TiO_2 monolayers. Notably, the similar synthetic strategy can be used to synthesize In_2O_3 [99] and Cu_2O [100].

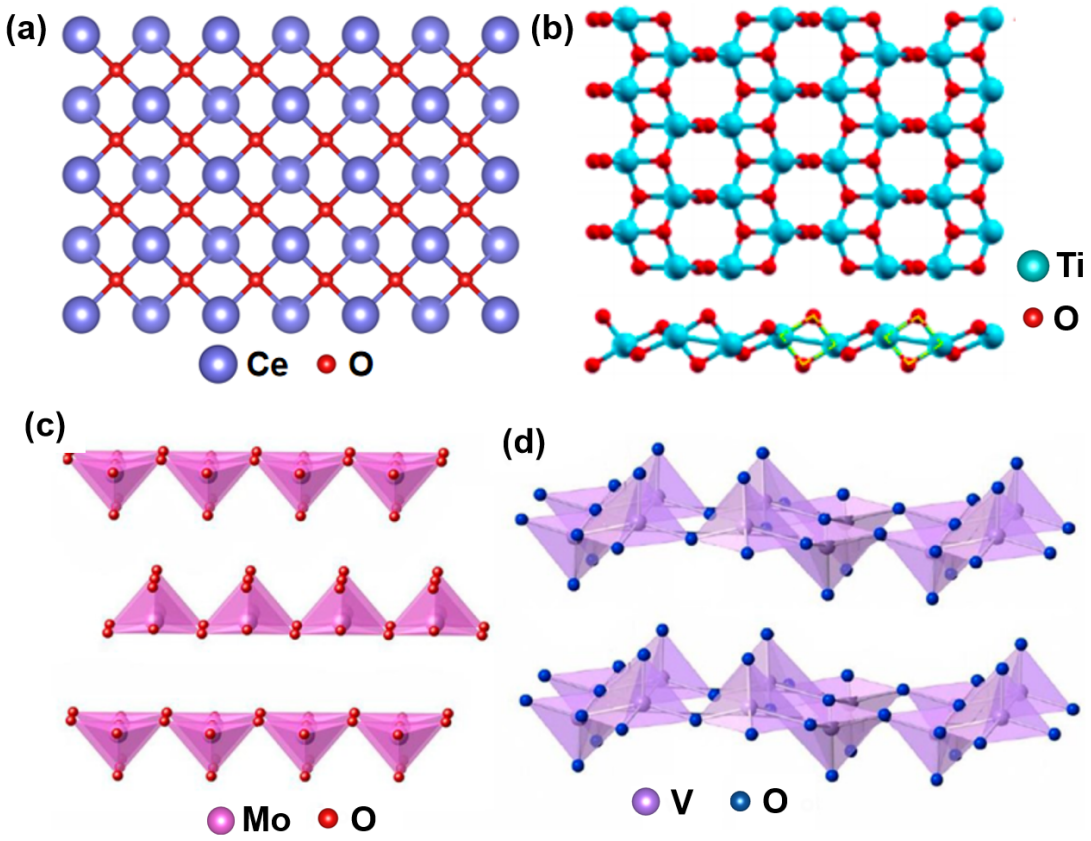

Figure 4. Crystal structures of (**a**) CeO_2. (**b**) TiO_2. Reproduced with permission from reference [101]. Copyright 2017, American Chemical Society. (**c**) MoO_3 and (**d**) α-V_2O_5. Reproduced with permission from reference [102]. Copyright 2015, Nature.

Among all the 2D metal-composite oxide nanomaterials, the TiO_2 nanosheet is one of the most widely used photocatalysts due to the high chemical stability, low cost and innocuous nurture. It is found that the obtained density of states (DOS) near the Fermi level and charge density on the surface of TiO_2 nanosheets are increased with the band gap of 3.2 eV and suitable band alignment to absorb the sunlight irradiation (shown in Figure 6), giving rise to 450 times higher photocatalytic activity under ultraviolet region than TiO_2 bulk material toward CO_2 reduction for format formation. Han et al. previously reported preparation of an anatase TiO_2 monolayer with 89% of reactive {001} facets on the two side surfaces via a hydrothermal method [103]. It is proven that a large percentage of {001} facets plays a significant role for enhancement the photocatalytic activity of a TiO_2 nanosheet. In addition, the hybridization of single Pt atom with TiO_2 exhibited an excellent photocatalytic efficiency for H_2 evolution compared to that of commercially available Evonik (formerly Degussa) P25 TiO_2 and pristine TiO_2 nanoparticles. This improved photocatalytic property of Pt/TiO_2 hybrid nanosheet originates the synergistic effects of surface fluorination and exposed {001} facets [104]. While it should be addressed that the photocatalytic activity of TiO_2 nanosheets only play a superiority in the ultraviolet region due to the large bandgap. In previous works, conventional approaches, such as the introduction of intrinsic

defects or impurities and combination of TiO_2 with electron acceptor materials were used to reduce the bandgap of TiO_2 nanosheets. One representative case for combination with electron acceptor materials is TiO_2/graphene composites, which shows an enhanced photocatalytic performance since the bandgap of TiO_2 is reduced via energy hybridization with C 2*p* orbitals, leading to a new valance band formed [11]. We conclude that TiO_2 has received significant attention as a metal-composite oxide photocatalyt owing to its advance photocatalytic activity under ultraviolet light irradiation. While, in order to extend the optical response of TiO_2 and other metal-composite oxides, like ZnO into the visible light spectrum region, different kinds of modifications of traditional photocatalysts have been developed, such as doping, dye sensitization, hybridization and synthetic multi-component oxides or nanocomposites. On the sides, due to the layered structure of $Bi_2W_2O_9$, which has $[W_2O_7^{2+}]$ and $[W_2O_2^{2+}]$ layers, the WO_3 nanosheet can be acquired through selective etching of $[W_2O_2^{2+}]$ layers, leading to the quantum confinement effect. As a result, the bandgap of the WO_3 nanosheet is increased to 2.8 eV [105], leading to a more positive position of the top valence band level than water oxidation potential, as shown in Figure 6. Thus WO_3 is the most widely used photocatalyst for producing O_2. Zhou et al. recently synthesized a Bi_2WO_6 monolayer with the assistance of cetyltrimethylammonium bromide based on a bottom-up wet-chemical method, where Bi atoms are unsaturated on the surface of Bi_2WO_6 nanosheets, giving rise to a great deal of photocatalytic active positions on the surfaces [106]. Accordingly, these large percentages of active sites lead to an excellent photocatalytic performance of Bi_2WO_6 by directly generating holes on the surfaces under visible light irradiation [106]. In addition, the calculated bandgap and band edge position of VBM and CBM relative to a vacuum is reported in previous work. More relative studies about bandgap and band edge levels of 2D metal-composite oxide nanomaterials are collected in Figure 6. Moreover, RuO_2 [107,108] and IrO_2 have shown an improved oxidation evolution efficiency under visible and [109,110]. Although the activity is still very low, the design of water splitting systems with these transition meter oxides and a sensitizer should be considered due to their unusual metal-like electronic structures.

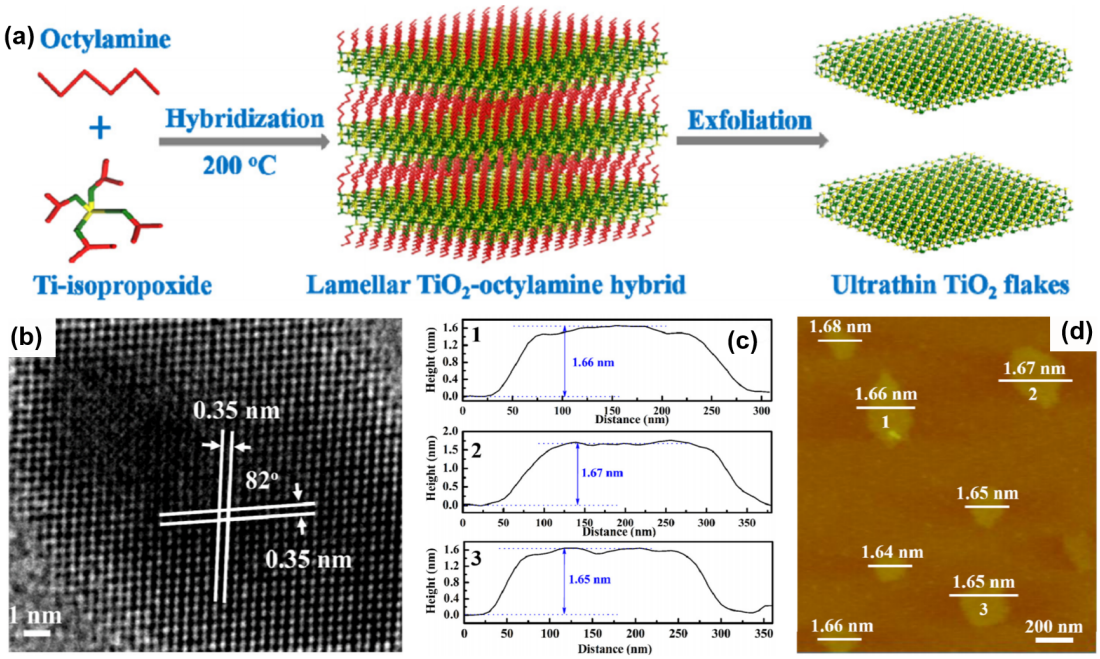

Figure 5. (**a**) Schematic drawing to form ultrathin TiO_2 nanosheets. (**b**) HRTEM image. (**c**) The height profiles corresponding to the AFM image in (**d**); the number from 1 to 3 in (**c**) corresponding to the numbers from 1 to 3 in (**d**). (**d**) AFM image of ultrathin TiO_2 flakes. Reproduced with permission from reference [98]. Copyright 1979, IOPscience.

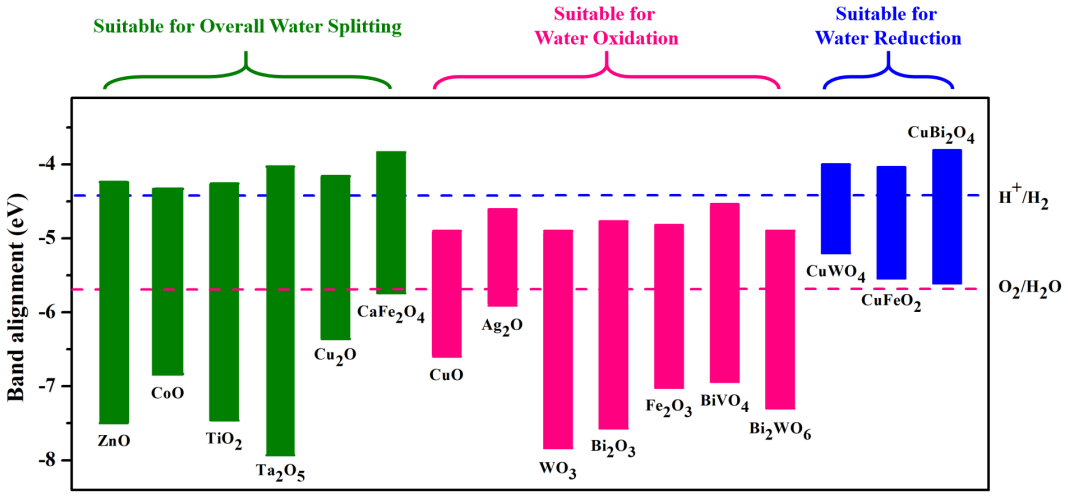

Figure 6. Band alignments of some typical 2D metal-composite oxides with respect to the water reduction and oxidation potential for photocatalytic water splitting. The band alignments data are from references [81,111–123].

3.2. Transition Metal Dichalcogenides (TMDs)

It is well known that the TMDs displayed layered compounds with the common chemical formula of MX_2, in which M represents the transition metal from group IV/V/VI (Ti, Zr, Hf, V, Nb, Ta, Mo and W), and X shows a chalcogen atom (S, Se, and Te) [86]. Every TMD monolayer is made by three atomic layers where the M layer is sandwiched between two chalcogen layers. Different kinds of exfoliation routes have been reported to synthesize the TMD monolayer using chemical intercalation of Li ion [124], adhesive tape exfoliation [125,126], sonication-assisted mechanical exfoliation using organic solvents or polymer surfactant [82,127] and electrochemical Li intercalation [128]. Whereas 2D nanosheet exfoliation has a critical influence on the geometric structure of TMD. Thus, TMD monolayers could stack together to form different crystal polytypes via the vdW force. For example, MoS_2 crystallization consists of mainly four crystal structures, such as 1H, 2H, 1T, 1T$^{'}$ (i.e., distorted 1T) and 3R structures, as depicted in Figure 7. The configuration of 2H has a stacking order of atoms with S-Mo-S$^{'}$ (ABA) in a closed packing symmetry with hexagonal arrangements and trigonal prismatic coordination, as shown in Figure 7d. The formation of the 1T structure is made by an atomic stacking sequence of S-Mo-S$^{'}$ (ABC) in the form of octahedral coordination with tetragonal symmetry, as shown in Figure 7b. The 1T$^{'}$, the distorted 1T structural arrangements, also contains an octahedral coordination, but it has a superstructure in each layer, as shown in Figure 7c, for example a tetramerization ($2a \times 2a$), with a trimerization ($\sqrt{3}a \times \sqrt{3}a$) and follows a zigzag chain ($2a \times a$). The 3R structure consists of three layers per primitive cell with different stacking arrangements between individual layers in comparison to the 2H phase, as shown in Figure 7e.

To date, a class of TMDs, such as MoS_2 [129–132], SnS_2 [133,134], TiS_2 [135], WS_2 [136], $MoSe_2$ [137], WSe_2 [138], has attracted tremendous research interest toward photocatalytic applications due to their unique electronic structure, relatively wide light absorption region, high electronic properties, sizable bandgap, natural abundances and excellent photocatalytic activities. For instance, MoS_2 bulk material displays an indirect bandgap of 1.2 eV, which is not very suitable for photocatalytic reactions owing to the insufficient reduction/oxidation potential to activating the photocatalytic mechanism [127]. Whereas, the MoS_2 monolayer possesses a bandgap of 1.96 eV (direct) due to the quantum confinement consequence, which provide a MoS_2 monolayer displayed by proper band positions and the capability for visible-light absorption, as shown in Figure 8 [127,139]. More importantly, it is reported that the edge S atoms in TMDs are more reactive for photocatalytic H_2 evolution with high mobility for charge carriers transport via the efficient bond formation by H^+ ions, resulting in an effective reduction to H_2 production [140]. Thus, Xie et al. tried to synthesize defect-rich ultrathin nanosheets

of MoS_2 in order to increase the active sites on the two surface layers [141]. Except, the introduction of oxygen defects can also enhance the active sites since the MoS_2 phase is changed to the octahedral metallic one, giving rise to the acceleration of the hydrogen evolution process [142]. Up to now, for photocatalyst mechanisms, using various 2D TMDs monolayers has been explored with diverse metal ions, for example, binary W/Mo/SnX_2 [134,143,144], Cd/Ge/CoX [145,146], In_2X_3 [58,147], ternary $CdZnX_2$ [148], $ZnInX_4$ [149,150], $MnSb_2X_4$ [151], In_4SnX_8 [152], quaternary Cu_2FeSnX_2 (X = S, Se, and Te) [153]. SnS_2 is another example with hexagonal arrangement, which can be prepared via refluxing the bulk SnS_2 matrix in formamide to break the interlayer vdW interactions [154]. The SnS_2 nanosheets displaying a nearly transparent feature is determined to be 0.61 nm via the AFM, implying the successfully synthesized ultrathin thickness, which is in better agreement with the single-nanolayered SnS_2 slab along the direction of (001). Particularly, the calculated electronic structure of SnS_2 monolayers shows a significant change with increased bandgap, significantly higher DOS at the VB edge and efficient interfacial charge transfer. All these novel properties have come from the single-layer configuration. Therefore, monolayers of SnS_2 provide a general photocatalytic performance division of water remarkably improved, which is 70 times higher than the SnS_2 bulk under visible light.

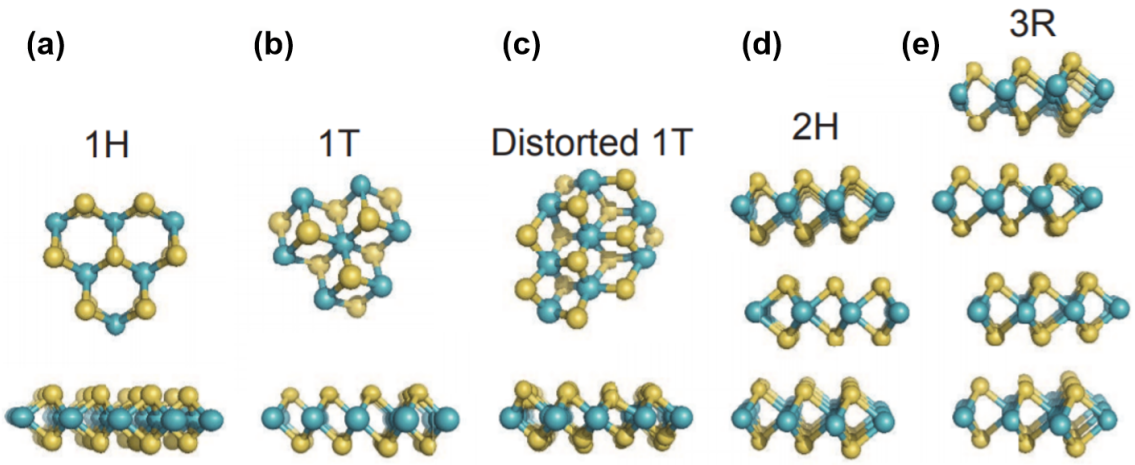

Figure 7. Crystal structures of predicted ground states for transition metal dichalcogenides (TMDs) with different polymorphisms. Reproduced with permission from ref [86]. Copyright 2016, American Chemical Society.

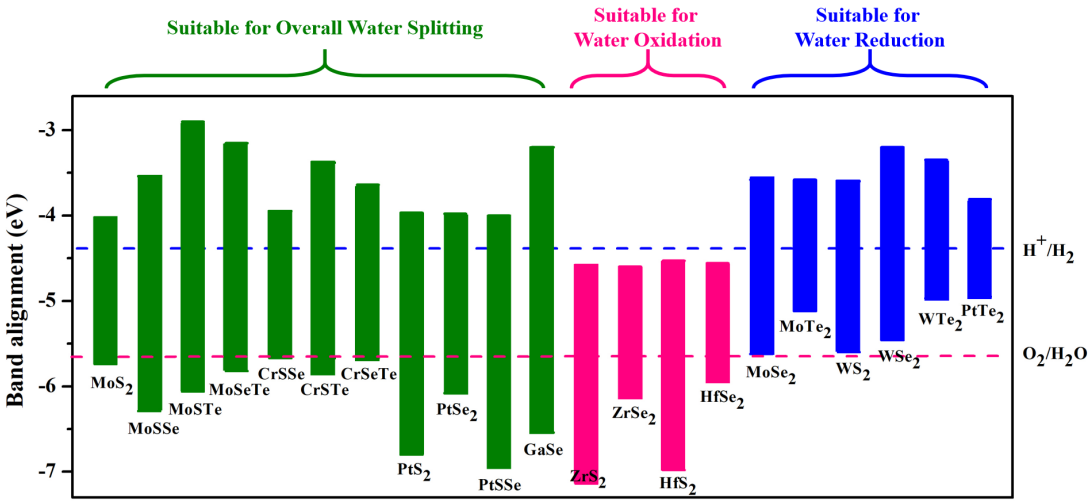

Figure 8. Band alignments of some typical 2D transition metal dichalcogenides with respect to the water reduction and oxidation potential for photocatalytic water splitting. The band alignments data are from references [121,155–161].

Recently it was reported by Zong et al. that the MoS_2 nanosheet directly deposited on the surface of CdS. It is seen that the H_2 production rate increased up to 36 times as compared to its pure CdS system, by including it with only 0.2 wt % of MoS_2. This co-catalyst is significantly larger than that of some amount of noble metal, for example Pt, Ru, or Rh used as a co-catalyst. In addition, the impact of a co-doped MoS_2/CdS hybrid nanostructure is examined for photocatalytic H_2. Surprisedly, due to the fast recombination of electron and hole pairs, the pristine MoS_2 and CdS monolayers did not show significant performance. In addition, doping at a certain wt % of MoS_2 also showed the enhancement of photocatalytic activity (14.10 mmol h^{-1} gh^{-1}) [162]. Moreover, when a finite number of layers of TMDs grew on the surface of CdS, synthesized MS_2-CdS (M = Mo or W), in which the monolayer MS_2 display a lateral size of 4–10 nm, can form on the Cd-rich (0001) surface of CdS wurtzite nanocrystals. Then anionic S donors MS_4^{2-} selectively connect to the Cd-terminated (0001) surface and form the nanohybrids, as presented in Figure 9a–d. Consequently, the number of active surface sites on these fabricated structures is increased, especially the hybrid composite area between the two structures, giving rise to the improved production output (WS_2-CdS 1984 mmol h^{-1} g^{-1} and MoS_2-CdS composite 1472 mmol h^{-1} g^{-1}) [163]. Furthermore, the CdS-Au/MoS_2 nanostructure is examined. It was found this heterostructure displayed superior H_2 evolution performance compared to their defect-free CdS nanorods. More importantly, a Schottky contact can be formed with the introduction of Au nanoparticles on the surface of CdS nanorods, which could also promote the formation of core and shell of MoS_2 nanolayers around it, as shown in Figure 9e [164].

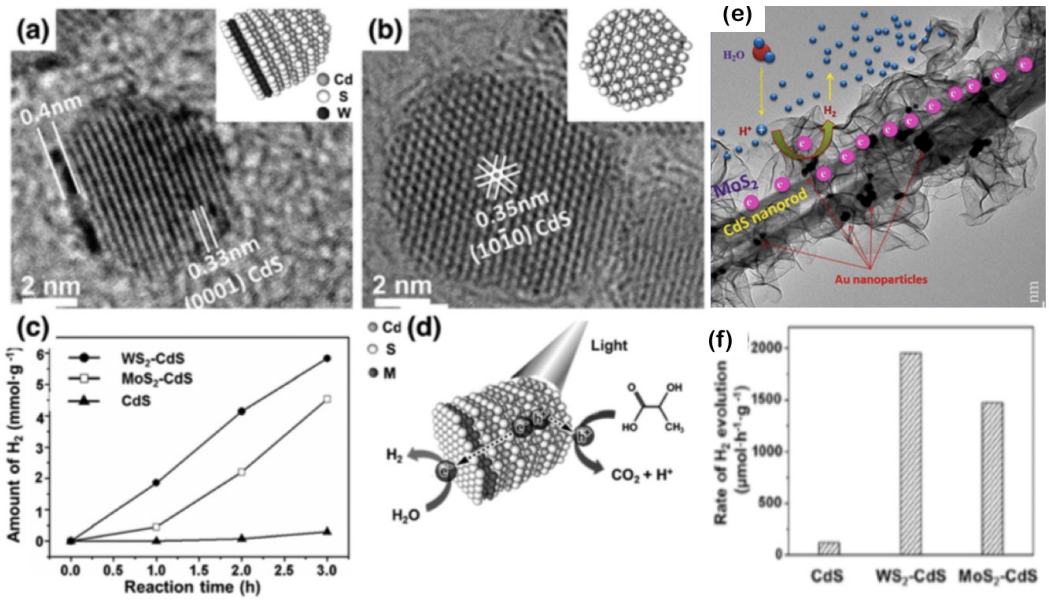

Figure 9. HR-TEM images of WS_2–CdS hybridized nanomaterial from (**a**) perpendicular view and (**b**) parallel side view; (**c**) H_2 production of hybridized nanomaterials. (**d**) The simplified schematic of the photocatalytic process for WS_2–CdS hybridized nanomaterial in lactic acid solution. Reproduced with permission from reference [163]. Copyright 2018, American Chemical Society. (**e**) TEM image of a 1D CdS-Au/MoS_2 hierarchical core/shell heteronanostructure with enhanced hydrogen evolution reaction (HER). Reproduced with permission from reference [164]. Copyright 2018, Elsevier. (**f**) Comparison of the H_2-evolution rate under visible sunlight irritation. Reproduced with permission from reference [163]. Copyright 2018, American Chemical Society.

In addition, the power conversion efficiency of phosphorene and TMD heterostructures was predicted reaching up to 20% by strain engineering [165], in which the interfaces formed in super-lattices and heterostructures play a key role in. Another example, MoS_2/AlN(GaN) heterostructure is not energetically costly, but its photocatalytic activity is significantly enhanced. Figure 10 shows the bandgap and band edge levels of this heterostructure are very near to the

standard necessity for overall water splitting. As a result, the light harvesting properties are largely boosted in visible-light and ultraviolet-ray wavelengths. Moreover, the oxidation and reduction mechanism are separately conducted at the opposite sides of the heterostructure, in which MoS_2 monolayer is an electron acceptor, and AlN(GaN) is an electron donor respectively, as shown in Figure 10b. Correspondingly, it will suppress the $e^- - h^+$ recombination rate and further increase the efficiency of the overall mechanism of photocatalytic water splitting. At present, transition metal dichalcogenides (TMDs) are the most popular cocatalysts to replace conventional noble-metal cocatalysts, and modifying the corresponding properties to them are largely explored, including new and effective synthetic methods, introducing intrinsic defects and impurity doping, hybridization and so on. Accordingly, MoS_2, WS_2 and other TMDs based photocatalysts have been vastly studied to modify with different materials, including oxides, sulfides and salts. Since the active positions of TMDs are mainly from their intrinsic defects and edges, thus synthesis of TMDs with some other smaller structures in order to expose more active sites are still scarce.

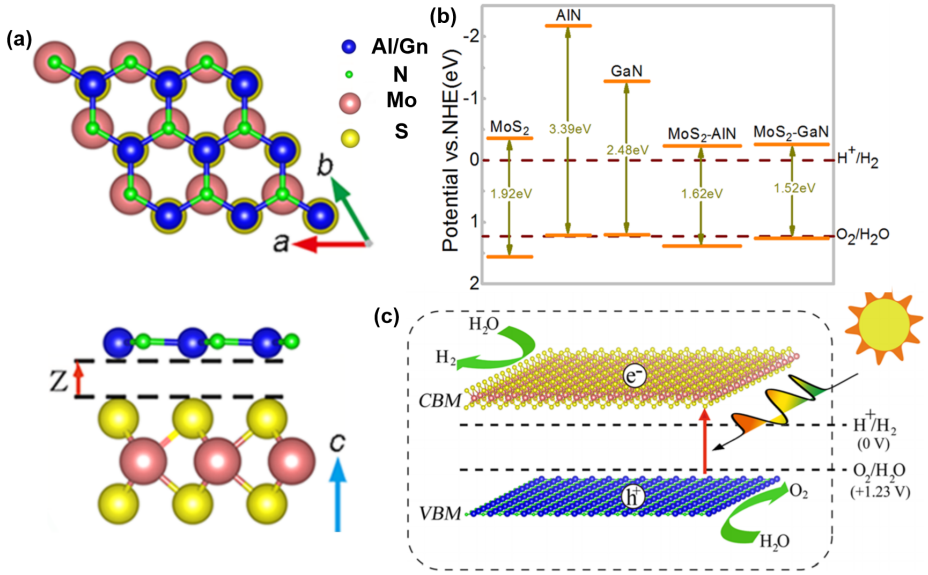

Figure 10. (**a**) Structure illustration of MoS_2/AlN(GaN) heterostructure. (**b**) Band alignment of MoS_2 hybrid hybridization materials. (**c**) Schematic drawing of photocatalytic water splitting for MoS_2/AlN(GaN) heterostructures, where VBM refers to valence band maximum and CBM refers to conduction band minimum. Reproduced with permission from reference [166]. Copyright 2016, American Institute of Physics

Very recently, a new class of layered materials synthesized called "Janus TMDs" have been reported by two independent groups [167,168]. MoSSe, one of Janus TMD monolayers, has been synthesized through two different synthetic pathways. One method is using a modified CVD-grown MoS_2 monolayer in which top-layer sulfur atoms are stripped off and replaced by H atoms, which is shown by a thermal selenization to get a structurally stable Janus MoSSe monolayer, in which Mo atoms are covalently bonded with both underlying S and top layer Se atoms [167]. Zhang et al. proposed an approach that starts from the CVD as-grown $MoSe_2$ monolayers on the surface of SiO_2/Si. Then the top layer Se is sulfurized with a controlled substitutional reaction by vaporized sulfur [168]. Dissimilar to the randomly alloyed MoS_xSe_{1-x}, both methods produce a result that breaks the reflection symmetry along the out-of-plane direction in more asymmetric Janus MoSSe monolayer, as shown in Figure 11a. Thus, Janus MoSSe structures could supply an intrinsic strain and electric field within the monolayer, provide an alternative way to modulating the HER activity in TMD catalysts [169]. The Janus MoSSe monolayer exhibits extraordinary visible-light absorption efficiency ($>1 \times 10^5$ cm^{-1}), suitable VBE and CBE positions for initializing the redox reactions of H_2O and high electron mobility of 0.53×10^3 cm^2 V^{-1} s^{-1} and hole mobility of 0.58×10^2 cm^2 V^{-1} s^{-1} [170].

Furthermore, the bandgap of the MoSSe monolayer is decreased, meanwhile, up tensile strain of the direct to indirect band gap transition appears, which can not only extend the light absorption range but also reduce the recombination for photogenerated electrons and holes, as displayed in Figure 11b [170]. Surprisingly, it is found the introduced chalcogen vacancy in MSSe could provide a better HER catalytic activity than that in pristine MSTe and MSeTe monolayers due to the more optimal amount of intrinsic lattice strain [171]. For example, Dequan et al. found the order of HER activities related to Janus WSSe monolayer is WSSe with Se-vacancy (ΔG_H = −264 meV) > WSSe with S-vacancy (ΔG_H = −174 meV) > pristine WSSe (ΔG_H = −158 meV) > pristine WS_2 or WSe_2, as shown in Figure 11c [171]. Similar works were also investigated by Ji et al. for the 2D Janus structure MoXY (X/Y = O, S, Se, and Te, X ≠ Y), as shown in Figure 11f [172]. Until now, numerous Janus TMDs monolayers were theoretically predicted for their structural stability and application as photocatalysts. Taking the Janus PtSSe monolayer as an example, Dai et al. demonstrated that it displayed high dynamic, thermal and mechanical stability, as shown in Figure 11d [155]. Remarkably, an indirect bandgap of 2.19 eV with a high absorption coefficient in the visible light region, suitable band edge positions and strong ability for electron-hole separation and transfer renders the 2D PtSSe monolayer a superior candidate for photocatalytic water splitting, as depicted in Figure 8. Additionally, band structural property together with band alignments and the versatile applications of Janus TM oxides and chalcogenides MXY (M =Cr, Ti, Zr, or Hf; Y = O, S, Se or Te; X =O, S, Se or Te; X ≠ Y) were theoretically investigated, the relevant results are summarized in Figures 11e–f and 8 [173]. Among them, it is found that MXY (M = Mo, Cr; X, Y = S, Se or Te; X ≠ Y), MSO (M = Ti, Zr, Hf) monolayers are superior candidates for photocatalysis because of their appropriate bandgaps and optimal redox potentials for overall water splitting, while the rest of the Janus monolayers can only work in half-reaction, either in a hydrogen evolution reaction or in an oxygen evolution reaction.

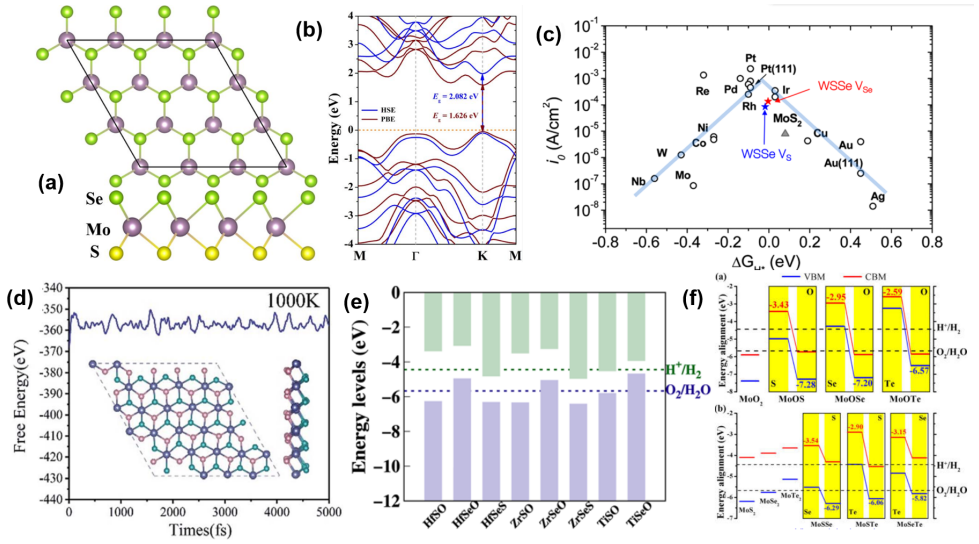

Figure 11. (**a**) Optimized crystal structures of Janus MoSSe monolayer from top and side views. (**b**) Band structures of MoSSe monolayer based on PBE and HSE06 functionals, respectively. Reproduced with permission from reference [174]. Copyright 2018, American Chemical Society. (**c**) HER volcano curve including Janus WSSe. Reproduced with permission from reference [171]. Copyright 2019, Royal Society of Chemistry. (**d**) The energy variations of PtSSe monolayer at 1000 K by AIMD calculations. Inset in (**d**) shows the snapshots of the equilibrium structure of SL PtSSe at 1000 K. Reproduced with permission from reference [155]. Copyright 2018, American Chemical Society. (**e**) Band alignment of Janus MXY monolayers (M = Ti, Zr, or Hf; X = S or Se; Y = O or S; X ≠ Y) with potential positions of reduction reaction (H^+/H_2) and oxidation reaction (O_2/H_2O), respectively. Reproduced with permission from reference [173]. Copyright 2018, American Chemical Society. (**f**) Band edge positions of pristine MoX_2 monolayers (X = O, S, Se, and Te) and Janus MoXY monolayers (X/Y = O, S, Se, and Te, with X ≠ Y) structures, reproduced with permission from reference [172]. Copyright 2017, Nature.

3.3. MXenes

The exfoliated thick transition metal carbides, nitrides or carbonitrides (MXene) possess many unique properties, such as excellent intrinsic electronic/ionic conductivity, high surface capacitive activity, high hydrophilicity and special layered structure with a tunable surface state through decorating terminal atoms [175–177]. Thus, MXene and MXENE-Polymer composite films are proposed as attractive candidates as building blocks for the solar energy conversion. Two-dimensional MXenes can be chemically extracted from the MAX phases with a general formula of $M_{n+1}AX_n$, where $_n$ could be 1, 2, or 3, M can be Ti, V, Cr, Nb, W, etc., transition metal, A is group IIIA or IVA elements of the periodic table (e.g., Al, Si, Sn, In, etc.), and X is carbon and/or nitrogen [178,179]. MXenes is generally expressed as $M_{n+1}X_nT_x$ because during the etching process, the surface might be bounded by some termination groups, such as -O, -OH or -F, x is the number of the corresponding terminating groups. As shown in Figure 12, the parental MAX phases show a hexagonal layered structure with the space groups of $P6_3/mmc$, in which M layers are hexagonal close-packed (hcp) structural and the octahedral sites are occupied by X atoms [178,180,181]. If A layers are selectively etched using strong etching solutions, one can obtain MXenes. Three different MXenes structures are collected in Figure 12e, they are M_2X, M_3X_2 and M_4X_3 [178]. In addition, many ordered double-Metal 2D MXenes ($MX'M''$Xene) are proposed and investigated theoretically and experimentally. For example, $Cr_2TiC_xT_x$, Mo_2 Ti_2C_3Tx, and Mo_2TiC_2Tx in Figure 13 have been successfully synthesized [182].

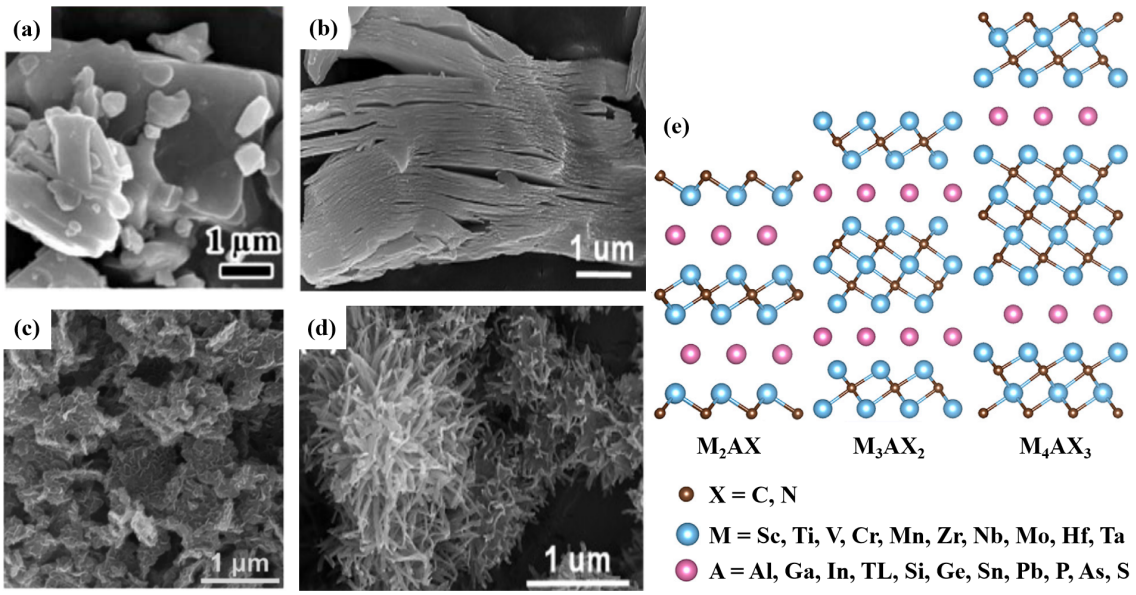

Figure 12. (**a**) SEM image of Ti_3AlC_2 particle before treatment. Reproduced with permission from reference [183]. Copyright 2018, Elsevier. (**b**) SEM image of Ti_3C_2 MXene. Reproduced with permission from reference [184]. Copyright 2017, Wiley-VCH. (**c**) SEM image of MoS_2/Ti_3C_2-MXene@C nanohybrids. Reproduced with permission from reference [185]. Copyright 2017, Royal Society of Chemistry. (**d**) Ti_3C_2-TiO_2 nanoflowers synthesized at 300 °C temperature. Reproduced with permission from reference [184]. Copyright 2017, Wiley-VCH.

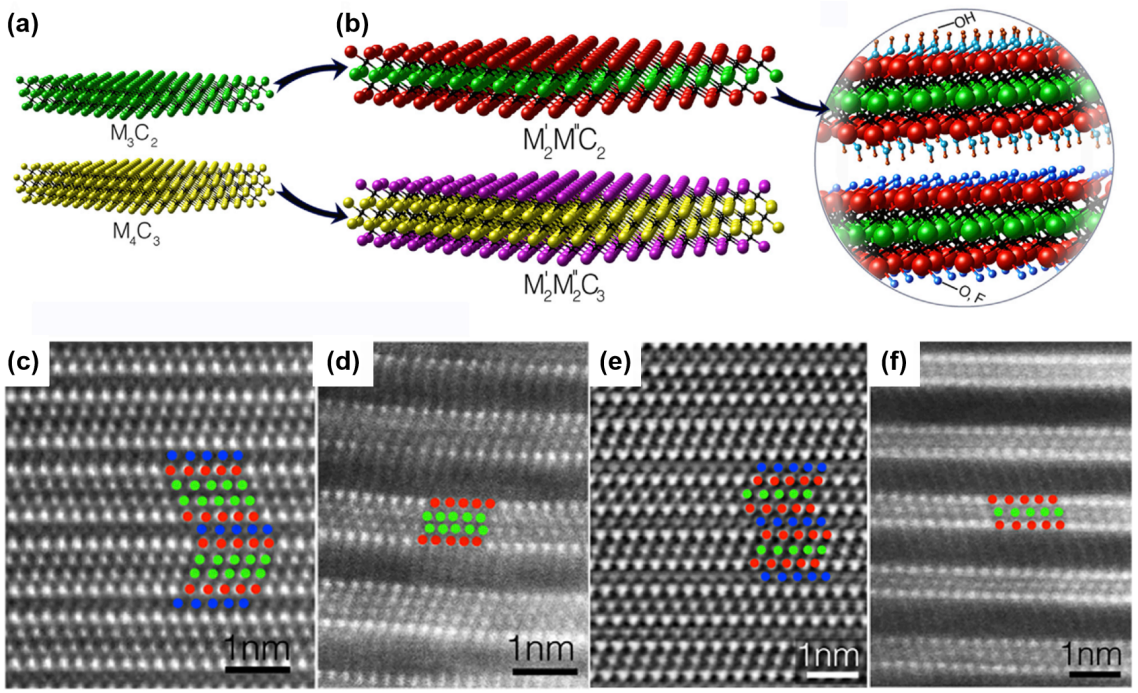

Figure 13. (**a**) Schematic of currently available single-transition-metal MXenes. (**b**) Schematic of double-transition-metal MXenes. (**c**–**f**) HRSTEM images of (**c**) $Mo_2Ti_2AlC_3$, (**d**) $Mo_2Ti_2C_3$, (**e**) Mo_2TiAlC_2, and (**f**) $Mo_2TiC_2T_x$. Red, green, blue, and black circles represent Mo, Ti, Al, and C atoms, respectively. Reproduced with permission from reference [186]. Copyright 2016, Wiley-VCH.

The previous investigations demonstrate the bare MXenes exhibits metallic properties [182], which do not favor the photocatalytic performance. However, they can be used as an effective hybridization support for photocatalyst materials, since the hybridization with MXenes could accelerate the migration of charge carriers, increase charge separation and strong electronic coupling as well as enhance the redox reactivity. For example, Wang et al. successfully synthesized TiO_2 and MXene-based hybrid photocatalysts ($TiO_2/Ti_3C_2T_x$), which shows high activity (Figure 14). In detail, the hybridization between Ti_3C_2 nanosheets and TiO_2 nanosheets with exposed (001) and/or (111) facets were successfully synthesized via hydrothermal partial oxidation reaction [187]. The obtained $TiO_2/Ti_3C_2T_x$ nanocomposite predicts a 400% enhancement in the photocatalytic hydrogen revolution reaction (HER) compared with bare TiO_2, where the uniformly grown TiO_2 interact with $Ti_3C_2T_x$ substrate, leading to a fast separation of photogenerated $e^- - h^+$ pairs, resulting in inhibiting the charge recombination. In addition, Nb_2CT_x and Ti_2CT_x are also hybridized with TiO_2 nanosheets as reduction cocatalysts to enhance the photoactivity in HER [187]. In particular, they show better HER catalytic performances than bare $Ti_3C_2T_x$ when hybridized with TiO_2 as co-catalysts, as shown in Figure 14b. It is because of Nb_2CT_x has the highest work function of 4.1 eV. The intrinsic reason is the dissimilar Fermi levels of MXene and TiO_2, which facilitate the transfer of photogenerated electrons from the bottom conduction band position of TiO_2 to MXene. Therefore, the conduction band and valence band levels of TiO_2 are bent upward according to the mechanism in Section 2, which drives the electrons accumulation in MXene and holes accumulation in TiO_2, as shown in Figure 14c, correspondingly, a Schottky barrier is formed at the heterointerfaces of TiO_2/MXene to restrain the electrons returning back to TiO_2 nanosheet sides. As a result, the reaction of the accumulated electrons with H^+ ions occurs on the MXene side with the production of H_2. Additionally, $Nb_2O_5/C/Nb_2C$ (MXene) ternary hybrid nanocomposites (NCN-x, x = 0.5, 1. and 1.5 h) are synthesized by Su et al. via oxidizing the surface of Nb_2CT_x to generate a Nb_2O_5 layer, in which CO_2 is used as the mild oxidant [188]. The results demonstrated the photoactivity of NCN-1.0 is four times higher toward HER than that of defect-free Nb_2O_5 monolayer, as shown in Figure 14d. Recently, hybridizing

between MXene and transition-metal chalcogenides has become a hot topic in the photocatalysis water splitting field for sunlight harvesting and energy conversion. Some metal sulfides/Ti_3C_2 (metal sulfides include CdS, ZnS or $Zn_xCd_{1-x}S$) have been synthesized, as shown in Figure 14e [175]. Among them, CdS/Ti_3C_2 exhibits excellent HER photoactivity with 14.342 μmol hr^{-1} g^{-1}, with an astonishingly large apparent quantum yield value of 40.1% at 420 nm, which is largely high than that of pristine CdS. It reveals that synthesized noble-metal-free metal sulfide photocatalytic systems are feasible in the near future. In addition, it has been supported by the relevant theoretical studies using DFT calculations. In addition, the developed Ti_2C/g-C_3N_4 shows a higher hydrogen production rate of 950 μmol hr^{-1} g^{-1} with an apparent quantum yield value of 4.3% at 420 nm [189,190]. Pandey et al. reported the functionalization with O termination is considered to be the most feasible method for HER, than that with -OH or -F termination [176,191]. For example, it is found O_2-terminated Ti_3C_2 is a promising hydrogen production cocatalyst [175]. Particular, Professor Zhou's group investigated 48 MXenes (M_2CT_x, M = Sc, Ti, Zr, Hf, V, Nb, Ta, Mo, T = O, OH, or F) in order to deeply understand their photocatalytic performance by analyzing the electronic structures, charge carriers mobility, and optical absorption property, as shown in Figure 15. Among which the bandgaps and band alignments of 2D Zr_2CO_x and Hf_2CO_x meet the requirements as the promising photocatalysts for high efficiency photocatalytic water splitting, as shown in Figure 15. While some other opinions also exist. For instance, Li et al. claimed that the Ti_2CF_2 monolayer has an excellent electrochemical property with highly efficient HER activity, demonstrated experimentally and theoretically [192]. Specifically, it illustrates that the novel surface state of the Ti_2C monolayer bounded by strong electronegative F termination groups could not only enhance the light absorption, promote the surface adsorption kinetics but also facilitates the migration of charge carriers, and thus improves the photo catalytic efficiency. This study claims that the Ti_2CF_2 monolayer shows a similar electrocatalysis performance with that of Ti_2CTF_2 (O-terminated), but $Ti_2C(OH)F_2$ nanosheets do not effectively generate either H_2 nor O_2. On the whole, MXene with O termination shows enhanced photocatalytic performance compared with -OH and -H terminations. In addition, raw MXene is widely used as a good photocatalytic substrate to support various 0D, 1D and 2D photocatalytic materials due to its large surface area and electronic conductivity. Thus, MXene-derived photocatalytic semiconductors should be abundantly investigated.

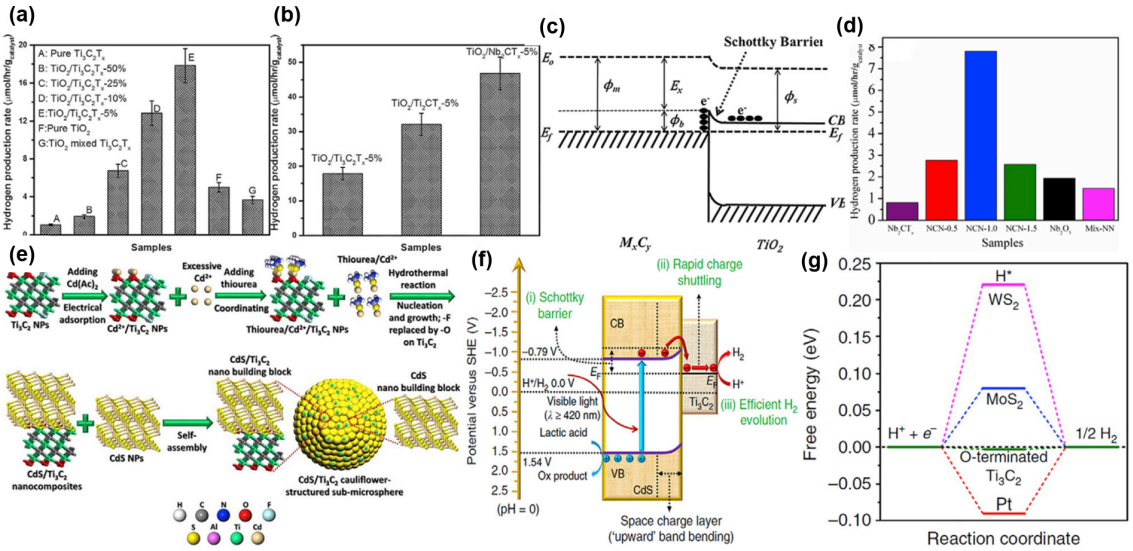

Figure 14. (**a**) The rate of hydrogen revolution reaction for $TiO_2/Ti_3C_2T_x$ and the corresponding control samples, (**b**) HER photocatalytic activity of TiO_2 loaded with different MXene as co-catalysts ($Ti_3C_2T_x$, Ti_2CT_x, and Nb_2CT_x), (**c**) the formation of a Schottky barrier at the MXene/TiO_2 heterointerface. Reproduced with permission from reference [187]. Copyright 2018, Wiley-VCH. (**d**) Photocatalytic

HER of $Nb_2O_5/C/Nb_2C$ samples. Reproduced with permission from reference [188]. Copyright 2018, Royal Society of Chemistry. (**e**) Synthesis procedure of CdS/Ti_3C_2 cauliflower-structured sub-microsphere, (**f**) charge carrier separation and transfer in the CdS/Ti_3C_2 system under visible light irradiation, (**g**) the obtained free energy for HER in Ti_3C_2 monolayer at the equilibrium potential. Reproduced with permission from reference [175]. Copyright 2016, Royal Society of Chemistry.

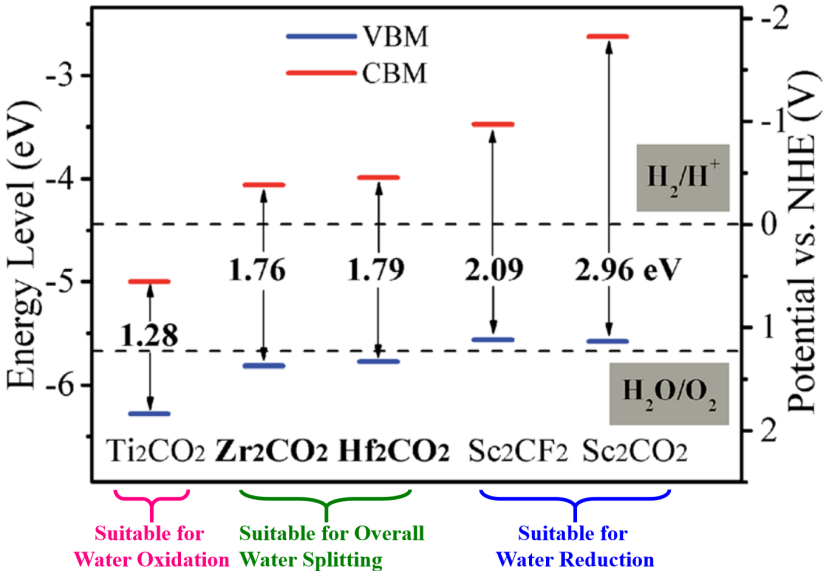

Figure 15. Band alignments of some typical 2D MXenes with respect to the water reduction and oxidation potential for photocatalytic water splitting. Reproduced with permission from reference [176]. Copyright 2016, Royal Society of Chemistry.

3.4. Graphitic Carbon Nitride

Graphitic carbon nitride (g-C_3N_4) possess an N substituted graphite structure, formed by sp^2 hybridization of C and N atoms, which is one of the famous metal-free photocatalysts [193,194]. Two different configurations are found for g-C_3N_4. One type configuration is defined as *s*-triazine, constructed by *s*-triazine units with a periodic array of single C vacancy, as shown in Figure 16d. Another one is condensed tri-*s*-triazine subunits in Figure 16e [193,194], which is connected with larger periodic vacancies in the lattice through the planar tertiary amino groups. The thermal oxidation exfoliation method and ultrasonication-assisted liquid exfoliation method were reported experimentally to obtain g-C_3N_4 ultrathin nanosheets [195–198]. Specifically, the thermal oxidation exfoliation route is proposed by Liu et al., where the thickness of the g-C_3N_4 crystal is gradually decreased through layer-by-layer etching with the extended times, as shown in Figure 16a [198]. Then a thickness of ~2 nm is prepared for the g-C_3N_4 nanosheet after the thermal oxidation for 120 min. While the quantum size effects result in a contrastable blue-shift of g-C_3N_4 nanosheets with increasing the temperature. In addition, due to the $n \rightarrow \pi^*$ transitions, an additional sunlight absorption peak appeared at ca. 500 nm at higher temperature >650 °C, giving rise to high visible light harvesting. In addition, the ultrasonication-assisted liquid exfoliation method is proposed because of the intrinsical layered structure of bulk C_3N_4. While the efficiency of this exfoliation method largely depends on the surface energies of the solvent molecules, which is calculated to be 115 mJ m^{-2}. Distinctly, it is consistent with the value of 102 mJ m^{-2} for the surface energy of water, a thickness of 2.5 nm is successfully gained for g-C_3N_4 by water-liquid exfoliation [199]. In addition, isopropanol [200] and other solvents [201,202] are also explored to further promote the exfoliation efficiency of bulk C_3N_4 since the thickness is a key factor to affect the performance of photocatalytic water splitting. The g-C_3N_4 monolayer possesses many extraordinary properties, such as wide surface area, good stability and an appropriate bandgap of ~2.7 eV for visible light absorption, thus it is applied into different kinds of photocatalytic applications, including hydrogen evolution, CO_2 reduction, pollutant gas molecules

removal, and disinfection. Compared with bulk g-C_3N_4, the electron migration rate is largely enhanced along the in-plane direction in g-C_3N_4 monolayer, and the corresponding hydrogen evolution activity is improved 5.4 times [203,204]. Meanwhile, several strategies, including morphology control [205–207], crystallinity control [208,209], vacancy introduction [210,211], chemical substitution [212,213] and surface activation [214,215] are performed in improving the photocatalytic performance of g-C_3N_4. For example, the synthesized holey g-C_3N_4, which possesses some carbon vacancies, shows promising possibilities to harvest the widening of sunlight and decrease the recombination of charge carriers for innovative photocatalytic systems [211]. On the other hand, the hybridization of g-C_3N_4 nanosheets with other species is developed as photocatalysts to improve the photocatalyst functionality of the system in whole water splitting, in that the self-aggregation from $\pi - \pi$ interaction in g-C_3N_4 nanosheets would severely hinder the transport of H_2O_2 intermediate and recycling performance [216]. Taking carbon nanosphere-incorporated g-C_3N_4 as an example, it shows 4.79 times higher photocatalytic activity than that of unhybridized g-C_3N_4, [217]. Moreover, not only the electron–hole recombination of hybridization with g-C_3N_4 is depressed, but also the oxidative reaction kinetics is accelerated, which remarkably enhances of photocatalytic activity for H_2 generation [218]. In addition, the recent researchers found the loading of 2D g-C_3N_4 on 1D $AgVO_3$ nanowire shows improved photocatalytic activity due to the more exposed photocatalytic sites, extended sunlight absorption region and promoted charge separation rate at the heterojunction interfaces [219]. Up to now, lots of g-C_3N_4-based hybrid photocatalysts with diverse inorganic materials have been constructed to improve the photocatalytic performance and durability, such as bismuth-based compounds [220,221], metal sulfides [222,223], metal oxides/hydroxide [224,225], carbon materials [217,226], spinel compounds [218,227], metal nanoparticles [228,229]. On the other hand, fabricating heterostructures of C_2N/InTe [230] and g-C_6N_6/g-C_3N_4 [231] were explored to improve the photocatalytic performances of C_2N and g-C_6N_6 by forming a built-in electric field across the interface. The results showed that the interface was effective at improving the separation of the electron-hole pair.

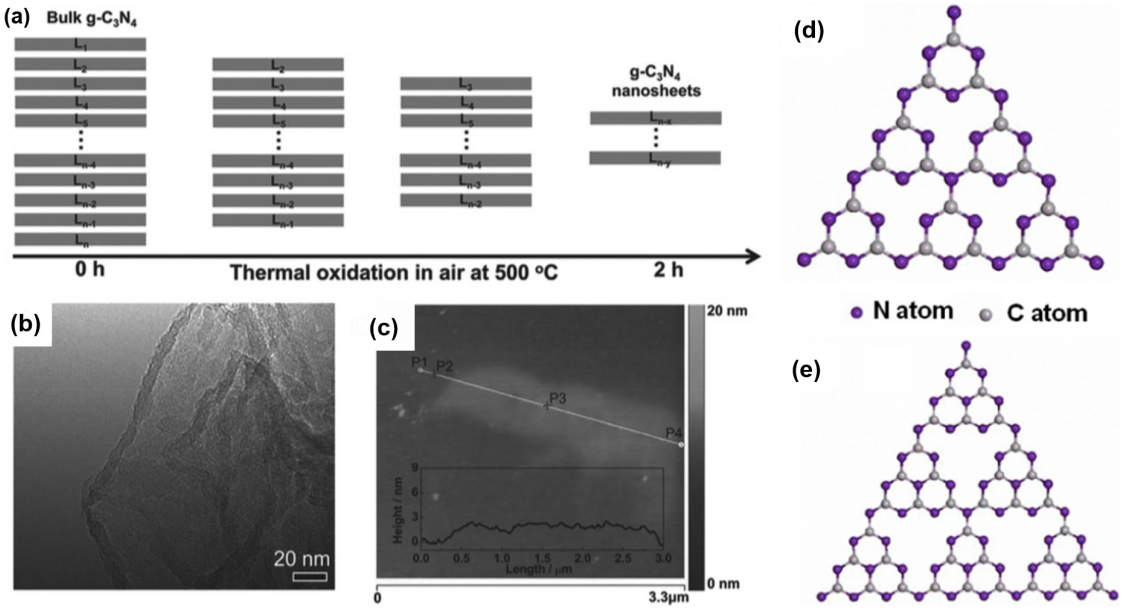

Figure 16. (**a**) Diagrammatic drawing of g-C_3N_4 monolayer by a direct thermal oxidation etching process at 500 °C. (**b**) TEM image and (**c**) AFM image of the g-C_3N_4 monolayer, with the insert showing the height profile along the P1-P4 line. Reproduced with permission from reference [198]. Copyright 2008, Royal Society of Chemistry. Schematic structural illustration of (**d**) *s*-Triazine and (**e**) tri-*s*-triazine structures of g-C_3N_4 monolayers, respectively. Reproduced with permission from reference [102]. Copyright 2015, Nature.

3.5. Boron Nitride

It is known that the bulk *h*-BN displayed a layered crystal structure analogous to that of graphite structure, which contains equal numbers of B and N atomic arrangements in the form of hexagonal structure with the space group of $P6_3/mmc$ [232]. In each layer of B and N, atoms are covalently bonded and these layers stack together by the vdW force to form the bulk crystalline structure (Figure 17) [233]. The Hexagonal Boron Nitride (*h*-BN) monolayer is considered as a graphene analog, which is generally known as the "white graphene" [232–234], as shown in Figure 17a. Usually, *h*-BN shows an indirect bandgap of 4.56 eV, which is not suitable for photocatalyst, as shown in Figure 17b,c. While intermediates of this layered material (named as ternary BCN compounds) could prepare the desired medium-bandgap semiconductors in which the bandgap and appropriate energy levels can be adjusted by chemical variations [235,236]. For instance, the bandgap of the "$B_{13}C_8N_{11}$" compound remarkably changes from 4.56 to 2.90 eV [237], as shown in Figure 17d–f [237]. Another case is "$B_{11}C_{12}N_9$" with a smaller bandgap of 2.00 eV, as displayed in Figure 17g–i. In the case of pure *h*-BN (Figure 17a), the partial DOS represents that the VBE and CBE of $B_{11}C_{12}N_9$ mainly originate from C 2*p* orbitals (Figure 17i) [237]. These BCN compounds are predicted as metal-free photocatalysts for water splitting under visible light. Hence, this investigation proved the doping of aromatic carbon into the *h*-BN lattice reduced its bandgap, constructing it as possible to induce visible light catalysis. On the other hand, semihydrogenated graphitic BN (*sh*-BN) monolayer, a strip-like antiferromagnetic semiconductor with a bandgap of 2.24 eV, is a potential metal-free visible-light driven photocatalyst for water splitting, as demonstrated in Figure 17j–l [238–240]. In addition, the hybridization of *h*-BN and CdS (*h*-BN/CdS) is a potential candidate for water splitting based on first principles calculations [234]. Through analyzing the Bader charge and charge density difference in the interfacial region of the heterostructure of *h*-BN/CdS, it is demonstrated that the electrons tend to transfer from the CdS side to the *h*-BN monolayer, which could efficiently separate the photogenerated electron-hole pairs. In addition, the bandgaps under 0–6% strain-driven meet the requirement to utilize visible light. Recently, the modified Pt electrode with *h*-BN nanosheets performed better hydrogen evolution reaction activity than Pt electrodes with a lower overpotential at a 10 mA cm^{-2} current density, a lower Tafel slope (29 ± 1 mV/decade) and high exchange current density (0.43 ± 0.05) × 10^{-4} A cm^{-2} [241].

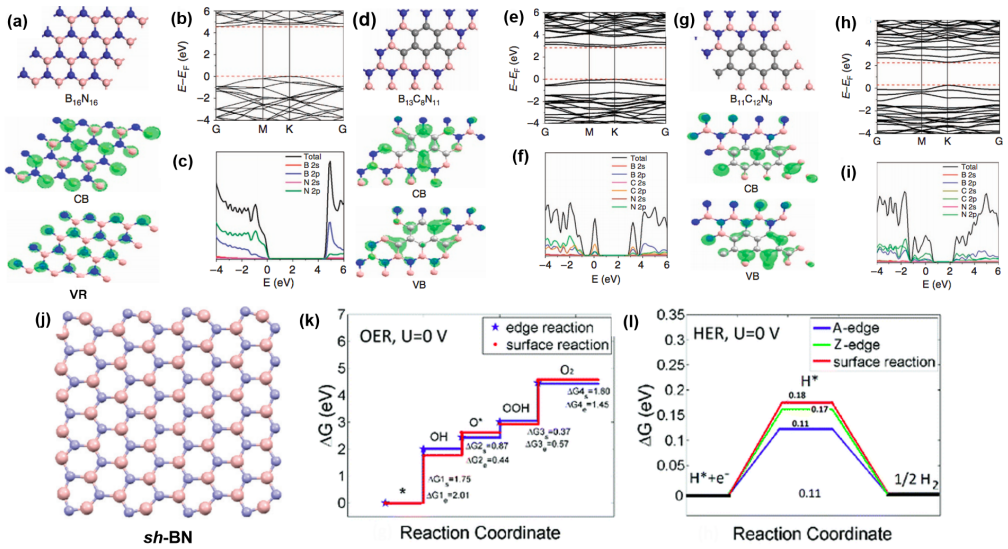

Figure 17. The optimized structures of *h*-BN and *h*-BCN with respect to (**a**) $B_{16}N_{16}$, (**d**) $B_{13}C_8N_{11}$ and (**g**) $B_{11}C_{12}N_9$ with the corresponding VBM and CBM, calculated energy band (**b**,**e**,**h**) and the corresponding total and projected electronic density of states (**c**,**f**,**i**). Reproduced with permission from reference [237]. Copyright 2015, Springer Nature. (**j**) The optimized structure of *sh*-BN monolayer and the free energy diagram of (j) the OER and (**k**) the HER for *sh*-BN monolayer. Reproduced with permission from reference [238]. Copyright 2020, Wiley-VCH.

3.6. Black Phosphorus (BP)

Another recently emerging 2D semiconductor-based photocatalyst for an alternative is phosphorence, which is analogous to graphene with a single atomic layer with three configurations of black phosphorus (BP), blue phosphorus (BP) and green phosphorus (GP) [242]. The well known phosphorene is formed by stacking of monolayers, which is interacted via van der Waals force, as shown in Figure 18a [243]. BP monolayer displays a puckered honeycomb structure, in which 3 P atoms are located in the same plane and the fourth P atom is located at the parallel adjacent plane. Each of them is connected with the three neighboring P atoms [243,244]. BP possesses many extraordinary physical and chemical properties, such as high electronic mobility (10,000 cm^2 V^{-1} S^{-1}), good electrical conductivity, tunable bandgap and anisotropic transport, thermodynamical stability and fast ion diffusivity [245,246]. More importantly, BP monolayer displays a p-type semiconductor. Thus, the constructed p-type BP with n-type TMDs was demonstrated as having excellent 2D electronics [247]. For example, the first BP transistor was obtained by micro-mechanical cleavage of the bulk material into a few nanosheet layers [248]. The previous experiment demonstrated that the charge carrier mobility could reach up to 1000 cm^2 V^{-1} S^{-1} in BP nanosheets with the thickness of 10 nm. On the other hand, this high charge carrier mobility along with the extraordinary optoelectronic property of BP monolayer has attracted increasing interest to researches for overall water splitting. Moreover, the bandgap of the BP monolayer increases to 2.1 from 0.3 eV in BP bulk [249]. Based on DFT calculations, it is found that the bottom conduction level of the BP monolayer is more negative than the reduction potential of H^+/H_2, which demonstrates the BP monolayer can be used as a photocatalyst to generate H_2 [250]. Whereas, the top valence band level of the BP monolayer fails to meet the condition of the redox potential of O_2/H_2O [250]. Furthermore, Lee et al. found the hybridization of BP with TiO_2 nanosheets displayed an improved photocatalytic performance in the visible light region [251]. In addition, the bandgap and band edge positions of this 2D layered BP could be adjusted simply by tuning the number of the atomic layers. Rudenko et al. demonstrated that the bandgap of BP was increasing with reducing the number of BP layers from four to one layer by applied general gradient approximation (GGA) as well as one-body-Green's function (GF) approximation, as shown in Figure 18d–g [252]. Experimental data for BP materials also confirmed that varying the number of BP layers allows bandgap tuning [252]. Inspired by this feature, the black phosphorus nanosheet is widely used as an efficient visible-light photocatalyst to generate O_2 [253]. For example, photocatalytic measurements verified the excellent visible-light-driven O_2 generation in few-layer black phosphorus, showing a quantum yield of ~0.91 at 530 nm excitation, as shown in Figure 18h [253]. Recently, a binary metal-free nanohybridization (BP/CN) of BP monolayer and graphitic carbon nitride (CN) was firstly proposed as a metal-free photocatalyst [254]. It is found the efficiency of H_2 evolution is largely higher than either the pristine BP monolayer or the CN monolayer under the sunlight irradiation with the wavelength of >420 and >780 nm, as shown in Figure 18c. It is found that the enhanced photocatalytic activity mainly originates from the interaction of P and N atoms at the interfacial interface in BP/CN hybridization. Specifically, the photogenerated electrons largely accumulate at the bottom of the conduction position of the BP monolayer, which can be regarded as an electron acceptor under visible light irradiation. Similar to the above mentioned Schottky barrier at the MXene/TiO_2 heterointerface, the trapped electrons at the interface of BP/CN heterostructure significantly improve the H_2 generation efficiency [254].

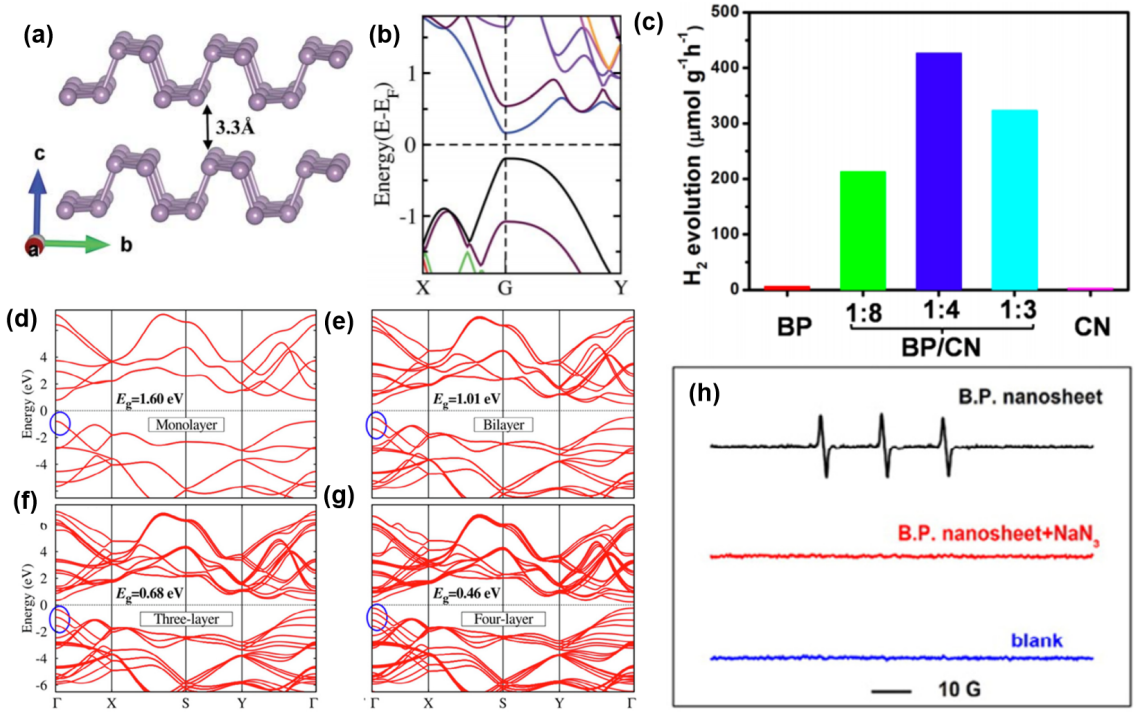

Figure 18. (**a**) Schematic crystal structure of the AA bilayer black phosphorus (BP) and (**b**) the corresponding band structure. Reproduced with permission from reference [255]. Copyright 2017, American Chemical Society. (**c**) Cycle stability test of BP/CN photocatalyst for H_2 evolution under visible light irradiation. Reproduced with permission from reference [254]. Copyright 2014, American Physical Society. (**d**–**g**) Band structures BP with different thicknesses calculated using the GF approach. Reproduced with permission from reference [252]. Copyright 2015, American Chemical Society. (**h**) Electron spin resonance (ESR)-trapping tests for detecting O_2 generation. Reproduced with permission from reference [253]. Copyright 1965, Wiley-VCH.

3.7. Metal-Organic Frameworks (MOFs)

MOFs are an interesting class that is crystallized by metal ions or cluster with organic ligands to form a porous crystal [256,257]. Thus numerous kinds of MOFs structures are formed with different coordination modes of metal ions or clusters and organic ligands. Accordingly, the formula of MOF crystals varies since they are crystallized into a layered configuration rather than a 3D structure. Recently, MOFs have exhibited numerous applications related to energy harvesting, energy conversion and energy storage. Especially the predominant photocatalytic performance of MOFs materials have been widely reported due to the unique porous structure with high surface area. In one instance, the photocatalytic behaviors of terephthalate (UiO-66) and 2-aminoterephthalate ligands [UiO-66(NH_2)] were first evaluated by Silva et al., as shown in Figure 19a [258]. It is found that UiO-66(NH_2) exhibited high photocatalytic activity for hydrogen production in methanol or water/methanol solution under sunlight irradiation with the wavelength of >300 nm. Another case to produce H_2 is an amino-functionalized titanium (IV) MOF, in which the organic linker was 2-amino-benzene dicarboxylic acid and Pt was photon-deposited [259]. Intriguingly, it is found the organic linker could motivate the sunlight harvesting capability, subsequently the adsorbed electrons can migrate to the titanium-oxo clusters, as depicted in Figure 19b. Very recently, the influence of $Co_xNi_{4-x}S_4$ loading on the surface of MOF (MIL-101) composite and the corresponding efficiency of H_2 generation were studied by Gao et al. [260]. They found the surface atomic structure showed an important role for fast electron transfer. It is well known that the process of hydrogen generation includes H^+ adsorption, H^+ reduction and the H_2 formation, as shown in Figure 1. Thus, the H^+ adsorption process is of great importance for the hydrogen evolution reaction, which can be evaluated by the activation energy (ΔG_H). Gao et al. found the $Co_2Ni_2S_4$@MIL-101 material displays the highest

activity since the adsorption energy and overpotential energy are lower in the system, as shown in Figure 19c [260].

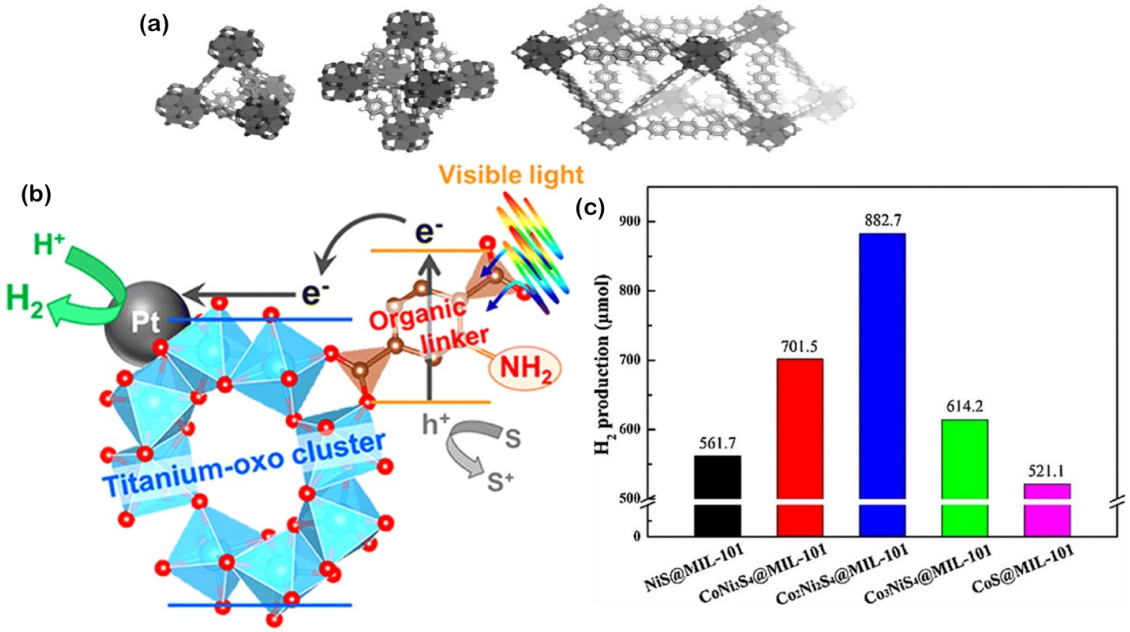

Figure 19. (**a**) Crystal structure of UiO-66. Reproduced with permission from reference [258,261]. Copyright 2018, American Chemical Society and 2010, Wiley-VCH, respectively. (**b**) Schematic illustration of H_2 generation in amino-functionalized titanium (IV) MOF. Reproduced with permission from reference [259]. Copyright 2017, Elsevier. (**c**) Hydrogen evolution reaction in NiS@MIL-101, $CoNi_3S_4$@MIL-101, $Co_2Ni_2S_4$@MIL-101, Co_3NiS_4@MIL-101 and CoS@MIL-101 photocatalysts in 100 mL 10% (v/v) TEOA aqueous solution (pH 9) under sunlight irradiation. Reproduced with permission from reference [260]. Copyright 2008, American Chemical Society.

3.8. Covalent-Organic Frameworks (COFs) and Polymers

Similar to MOFs, COFs are also porous crystalline materials, in which each organic building block units with light elements are covalently bonded, the light elements can be H, B, C, N, and O [262,263]. Up to now, various COFs building units have been synthesized and investigated, such as phenyl, biphenyl, naphthalene, anthracene, pyrene, triazine, have been explored [264,265]. Recently, Dichtel et al. found 2D COFs are commonly crystallized into a layered structure via strong covalent bonds in the layer, while the growth rate of COFs is related to the van der Waals surface and planarity of the linkers [266]. For instance, the 2D HHTP-DPB COF possesses a porous structure with 4.7 nm wide hexagonal pores, the corresponding space group is $P6_3/mmm$, as shown in Figure 20c [267]. The polymer stacking intermediate of larger aromatic cores could enhance the 2D COF formation due to the weak van der Waals interactions and appreciably lower activation energy. Recently, lots of attention has been given to the synthesis of highly porous 2D COFs using organic cores due to their conjugated structures and high mobility of charge carriers. Importantly, the amount of photocatalytic active sites of COFs could promote the electrons mobility on the surface [268]. In addition, the application of COFs has received much attention in photocatalysis, optoelectronics and photon/thermochromism. For example, Pradip et al. reported acetylene ($-C-$) and diacetylene ($-C-C-$) functionalized β-ketoenamine COFs, which displayed an excellent photocatalytic efficiency with the rate of 324 ± 10 μmol h^{-1} g^{-1}, as shown in Figure 20a,b [269]. The integrated electron-deficient 3-ethylrhodanine unit by Jiang et al. is an end-capping group to the periphery of a 2D sp^2 conjugated COF, sp^2c-COF_{ERDN} [270]. He reported the photocatalytic performance of hydrogen evolution reaction improved nearly 60%, compared to the unmodified COF under identical conditions, as depicted in Figure 20d. In addition, Pt dopped COF (Pt@COF) also exhibited an excellent photocatalytic property

to produce H_2 in sulfide oxidation with a turnover number of 25,000 and in hydrodebromination with a turnover number of 7313 reactions, as shown in Figure 20e [271].

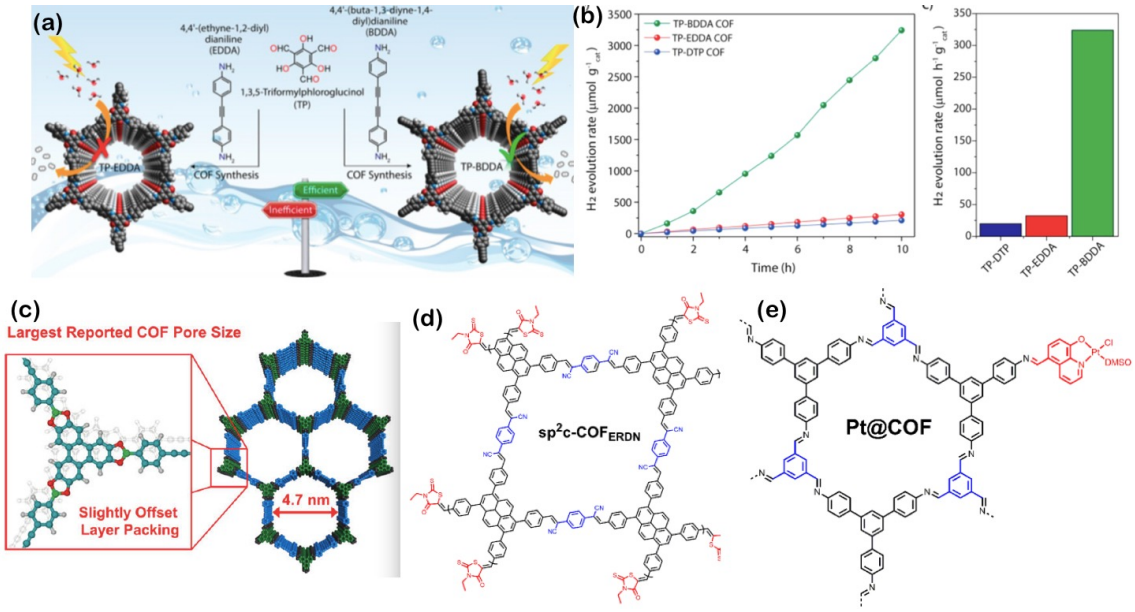

Figure 20. (**a**) Synthesis and characterization of TP-EDDA and TP-BDDA covalent organic frameworks (COFs) and (**b**) the comparison of hydrogen evolution performance and rate of TP-BDDA, TP-EDDA and TP-DTP catalysts under sunlight irradiation using TEOA as a sacrificial agent. Reproduced with permission from reference [269]. Copyright 2018, American Chemical Society. (**c**) Synthesis of HHTP-DPB COF in Model of the Idealized bnn Topology (right) and expansion of the region (left). Reproduced with permission from reference [267]. Copyright 2019, Elsevier. Structures of (**d**) $sp^2c\text{-}COF_{ERDN}$ and (**e**) Pt@COF (truncated monomer and the corresponding multitopic monomer are in red and blue, respectively. Reproduced with permission from reference [270,271]. Copyright 2020, Elsevier and 2012, Royal Society of Chemistry.

3.9. Perovskite Nanosheets

In recent years, perovskite-based layered materials have been taken extraordinary attention as photocatalysts to produce hydrogen, not only because the structures of layered perovskites are stable and could promote charge separation, but also they are cost effective, optical stability, corrosion resistance. In general, perovskite-based materials are derivatives of ABO_3 bulk perovskite oxides, where the A site is occupied by a rare earth cation or an alkaline cation while the B site is occupied by a transition metal cation [272,273]. These layered perovskite oxide materials possess a 3D configuration in which corner atoms share BO_6 octahedra with 12 A cations. Particularly, these layered materials are composed of 2D slabs of ABO_3 by weak electrostatic force. In addition, the interlayer cations are dispersed between the main 2D slabs in perovskites which are usually negatively charged, thus the whole system is electrically neutral. Normally, the lattice of perovskite-based layered materials display distortion since BO_6 octahedra tilts towards different directions, giving rise to different super-lattice configurations. Importantly, these distorted lattice structures show positive effects on excitation, transfer and separation of photogenerated e^--h^+. According to the slab layer stacking direction corresponding to the axis of bulk framework, the perovskite-based layered materials can be generally categorized into (100), (110) and (111) layered oxides [274]. Formulas of $A_{n-1}B_nO_{3n+1}$, $(Bi_2O_2)(A_{n-1}B_nO_{3n+1})$, $A'_2A_{n-1}B_nO_{3n+1}$ and $A'[A_{n-1}B_nO_{3n+1}]$ belong to (100) type perovskite oxides, (110) type pervskite structures can be described as $A_nB_nO_{3n+2}$ and (111) type pervskites is described as $A_{n+1}B_nO_{3n+3}$, in which n is the number of BO_6 octahedra, which is coordinated perpendicular to the surface of layers. Gang Liu et al. have systematically studied and summarized the structural properties

of perovskite-based layered materials [274]. Some types of perovskite-based layered materials are collected in Figure 21 [275].

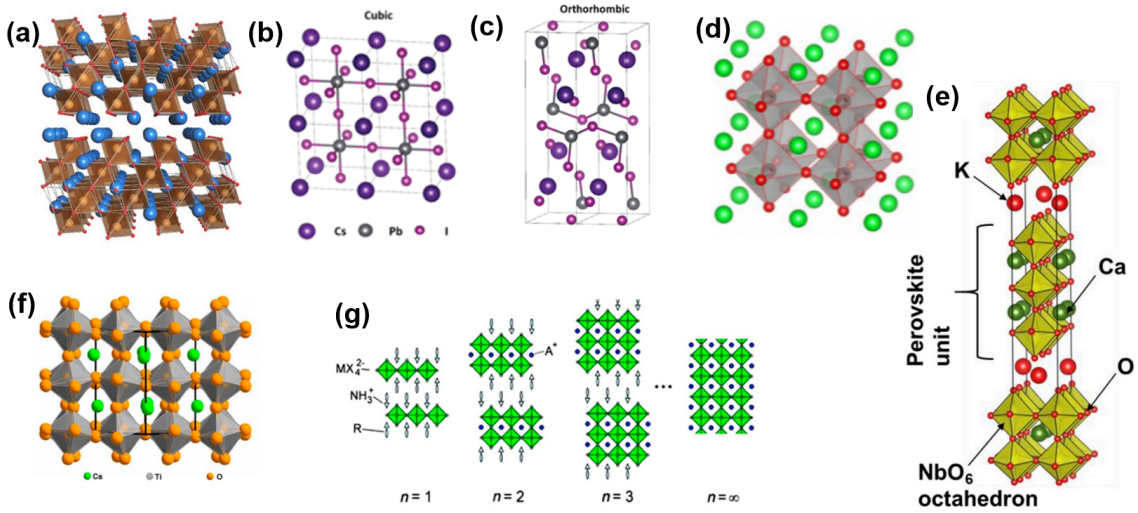

Figure 21. (**a**) Crystal structure of $Ba_5Nb_4O_{15}$, reproduced with permission from reference [276]. Copyright 2015, American Chemical Society. (**b**) Layered perovskite structures of $CsPbI_3$ in cubic and (**c**) orthorhombic phases, respectively. Reproduced with permission from reference [277]. Copyright 2015, Royal Society of Chemistry. (**d**) Perovskite oxide structure of $SrNbO_3$, reproduced with permission from reference [278]. Copyright 2013, American Chemical Society. (**e**) Dion–Jacobson structure of $KCa_2NaNb_4O_{13}$, reproduced with permission from reference [279]. Copyright 2020, Elsevier. (**f**) Perovskite oxide structure of $CaTiO_3$, reproduced with permission from reference [102]. Copyright 2017, American Chemical Society. (**g**) Layered perovskite structures of organic-inorganic materials, reproduced with permission from reference [280]. Copyright 2010, Royal Society of Chemistry.

$K_2La_2Ti_3O_{10}$ with bandgap of 3.5 eV is one kind of $A'_2A_{n-1}B_nO_{3n+1}$ phase layered perovskites, which shows excellent photocatalytic performance during loaded Pt atom with a H_2 production rate of 233.88 μmol g^{-1} h^{-1} [281]. In addition, Domen et al. found $Rb_2La_2Ti_3O_{10}$ is one of the most active photocatalysts when loaded Ni with H_2 and O_2 generation rates of 869 μmol g^{-1} h^{-1} and 430 μmol g^{-1} h^{-1}, respectively [282]. Moreover, extensive layered perovskite oxides with $(Bi_2O_2)(A_{n-1}B_nO_{3n+1})$ phase, such as $ABi_2Ta_2O_9$ (A = Cr, Br, Sr) [282], $ABi_2Ta_2O_9$ (A = Ca, Br, Sr, $K_{0.5}La_{0.5}$) [283] and $ABi_2Nb_2O_9$ (a = Ca, Ba, Sr, Pb) [284] have been also studied as photocatalysts for water splitting under visible sunlight. In principle, perovskite-based layered materials can chemically exfoliate into 2D nanosheets using tetrabuty-lammonium hydroxide [285]. Up to now, tremendous Ta, Nb, Ti perovskite nanosheets, chemically exfoliated from their parental bulk materials, have been found to be excellent photocatalysts for overall water splitting under UV sunlight. Beneficial for the molecular thickness and lateral dimensions with 100 nm-10mm, 2D perovskite nanosheets display great photocatalytic performance, including $TiNbO_5^-$, $Ca_2Nb_3O_{10}^-$, $Bi_2Nb_2O_9^-$ and $Nb_4O_{17}^-$ [286,287]. Previously, some reviews focused on the applications of both photocatalytic water splitting and CO_2 reduction, and challenges and prospects of nanoporous perovskite metal oxides have been reported [288,289]. It is found bandgaps of a series of $MTiO_3$ are larger than 3 eV, which will limit them to absorb the visible sunlight and the corresponding charge separation efficiency but only shows photocatalytic activity under ultraviolet light with approximately 5% of solar spectrum resulting. Nevertheless, these issues can be resolved by modification the bandgaps to enhance the charge separation and extend their spectral absorption to the region of visible light irradiation. With regards to perovskite-based layered materials, chemical component adjustment by doping Ni^{2+}, Fe^{3+}, Mo^{3+}, Cr^{3+}, Ti^{4+} and W^{6+} is usually introduced to substitute the B atoms in BO_6 octahedra, which can create an additional state in the bandgap to trap electrons or holes, leading to induced the recombination of $e^- - h^+$ pairs. In addition, the N element is also commonly used to substitute the

O atom. Commonly, doping different ions will exhibit different results for the photocatalytic activity. Previously, the effects of Zr substitution Ti atoms in $A'_2A_{n-1}B_nO_{3n+1}$ phase layered perovskites is investigated to photocatalytic split water under UV irradiation by Lee et al. [290]. Since the atomic radius of Zr is larger than Ti, the crystallinity of $KLaZr_xTi_{1-x}O_4$ is increased. While the highest photocatalytic activity is found to be $KLaZr_{0.3}Ti_{0.7}O_4$ [290]. In addition, the substitution of Cr for Ti was successfully introduced into the layer structure of $Sr_2Ti_xCr_{1-x}O_3$, and $Sr_2Ti_{0.95}Cr_{0.05}O_3$ showed excellent visible-light absorption with H_2 generation rate of 170 μmol $g^{-1}h^{-1}$. Surprisingly, it was 977 μmol $g^{-1}h^{-1}$ under full arc irradiation [291]. In all, the wide bandgaps due to the quantum confinement effect in these perovskite nanosheets can be solved by doping with proper atoms.

3.10. Nanoheterostructure Composites

In recent years, extensive efforts have been applied on the design and fabrication of novel nanoheterostructure composite photocatalysts, which can be capable of harvesting visible light. In the view of the physical and chemical property of composite materials, 2D based composites components can be categorized into four typical types: (1) the semiconductor/semiconductor (named as S–S); (2) semiconductor/metal (named as S–M) heterojunction; (3) the semiconductor/molecule heterojunction carbon group (named as S–Molecule); (4) the multicomponent heterojunction. S-S heterostructure is a very effective method to enhance the photocatalytic activity since the built-in potential at the interfacial contact can improve the electron-hole pairs to separate and directly migrate on the surface of the semiconductors. A representative example to study the charge separation is CdS/TiO_2 [292]. In addition, semiconductors with larger bandgaps could be sensitized to visible light conjunction with the semiconductor, which have smaller bandgaps. Furthermore, some semiconductors are cocatalysts that can promote the electrochemical reaction on the surface, including Nio, RuO_2, IrO_2 and so on [7,293]. Additionally, the semiconductors that possess good photochemical stability and electrochemical stability can act as an outside layer to enhance the structure stability of the photocatalysts. Many metal nanoclusters, such as Ag, Au, Pt and Pd play a critical role in enhancing the photoactivity of various semiconductor photocatalysts. First, the Schottky junction could be formed in M-S systems in which the band alignment of the Fermi level could generate a built-in electric field near the interfacial contacts of the metal and semiconductor. Second, the overpotential could be reduced by metal nanoclusters to make the surface electrochemical processes easier. The previous study demonstrated both Pt and Au nanoclusters can largely enhance the hydrogen evolution performance of TiO_2 [294]. Third, via a plasmonic enhancement effect, the metallic composite in M-S systems could improve the sunlight adsorption of semiconductors [76]. With regards to S–Molecule heterostructure composites, different kinds of molecules are widely used to modify the surface electronic states of the semiconductors. For example, many organic molecules, such as hydroxyl, silanyl, amino and carboxyl can act as a passivation layer to hinder electron-hole pair recombination and prevent the oxidation degradation of semiconductors [295]. In addition, the sensitization of transition metal complex dyes and inexpensive non-metal complex dyes could enhance the visible light harvest for the semiconductors with large bandgaps [293,295]. Particularly, multiple functional heterostructure composites, such as $CdS/Au/TiO_2$ [296] and $CdS/Pt/TiO_2$ [297] could be able to guide electrons and holes to occur the desired reaction, giving rise to decreased piling-up on the surface. Hence, it could enhance the photocatalytic activity and stability of multiple semiconductor composites.

On the other hand, the dimensionalities of different composites might be different. Thus, the dimensionality of individual components and the interfacial area in heterostructure composites display a large influence on the photocatalytic performance of the composite systems since the diffusion efficiency of a photogenerated electron is very sensitive to the structure character of the systems. Via manipulating the dimensionality and the size of individual components, four different types of interfacial contacts can be obtained, i.e., 0D/2D, 1D/2D and 2D/2D heterostructures. Generally, the small molecules, i.e., 0D materials, could adhere to the surface of 2D materials, whereas small size 2D nanosheets could grow or wrap on the surface of large size molecules. Pt, Au, Pd, Ru and RuO_2 are the typical

0D metal nanoclusters, which are usually introduced to various 2D nanosheets via in situ approaches and ex situ assembly methods to design high performance photocatalysts. For instance, averagely dispersed Pt nanoparticles on the surface of $KCa_2Nb_3O_{10}$ with size smaller than 1 nm displayed the highest photocatalytic performance for water splitting reactions [298]. Additionally, some 2D based photocatalysts have been investigated by introducing the 1D materials, including nanowires, nanorods, and nanotubes. However, the 2D/2D heterostructures shows better photocatalytic performance than 0D/2D and 1D/2D heterostructures since the better 2D/2D coupling hetero-interfaces promote the transfer of $e^- - h^+$ pairs and their separations. For instance, the interfacial contact in 2D graphene-TiO_2 is more intimate and adheres more sufficiently than that in 1D CNT-TiO_2, leading to higher photocurrent transient response of 2D graphene-TiO_2 under visible light irradiation [299]. Similar results are also found in graphene (nanoparticle, nanotube, nanosheet)-CdS composites [300]. It is found that 2D/2D heterostructure composites have stronger electronic coupling effects after analyzing the interfacial charge transfer kinetics, which could effectively promote the separation of $e^- - h^+$ pairs and their transfer across the heterojunction interface, leading to higher photocatalytic performance.

4. Synthesis Methods for 2D Materials

Various approaches have been explored to synthesize 2D monolayers or few-layer nanosheets and tailor the structure with corresponding physical and chemical properties in order to suit different kinds of applications. Generally the synthesis methods can be classified into two types based on the composition, crystal phase and surface property of materials: (1) the top-down method, which mainly depends on the exfoliation of 2D monolayers from their parental layered bulk material by overcoming the weak interlayer binding force; (2) the bottom-up method, which is more versatile in principle than most 2D nanosheets, might be gained by this method. In this section, some representative methods to prepare 2D materials are discussed and summarized.

4.1. Micromechanical Cleavage Using Scotch Tape

Micromechanical cleavage using scotch tape is a simple and conventional method to fabricate thin flakes by peeling and rubbing the surface of inorganic layered bulk materials. The weak van der Waals interaction between the layers of the materials is the key factor so that the applied mechanical force can peel of single or few layers of 2D materials without breaking the chemical bonding of the in-plane layer. The micromechanical cleavage technique is first used by Grim et al. to obtain a graphene monolayer from highly oriented graphite [301]. In addition, a more thin flake can be obtained by repeating this process several times. Then these thin flakes are washed with acetone and transferred on a clean, flat target surface of SiO_2/Si or quartz to further cleave it using plastic tweezers. The extension of this method has been widely employed to obtain various kinds of ultrathin 2D nanosheets from the bulk materials, such as *h*-BN [302], various TMD monolayers (TiS_2, TaS_2, MoS_2, WS_2, ReS_2, $TaSe_2$, $NbSe_2$, WTe_2, $Mo_xW_{1-x}S_2$, $ReS_{2x}Se_{2(1-x)}$, etc.) [303–311], topological insulators of Bi_2Te_3, Bi_2Se_3 [312,313], metal phosphorus trichalcogenides of MPS_3 (M = Fe, Ni, Zn, Mn and Cd) [314], BP [245,315] and $CuInP_2S_6$ [316].

This micromechanical cleavage technique is simple, fast and low cost and the size of exfoliated 2D materials can be up to tens of micrometers. In addition, no chemicals are utilized but shear force is applied during the fabrication process. Thus, the fabricated nanosheets keep the pristine structural integrity with minimum defects from the parental bulk materials, giving rise to many advantages. As a whole, the large lateral size, clean surface, "perfect" crystal quality, high crystallinity make mechanically cleaved 2D materials remarkable candidates to investigate the corresponding mechanical, electronic and optical properties and application in electronic and optoelectronic devices. However, there are some certain disadvantages that hinder their realistic applications. First, the production yield of this process is extremely low and the nanosheets always coexist with thick flakes on the substrate. Thus, it is suitable for laboratory scale studies but difficult to utilize in various high end technological applications, high yield and large-scale production. Second, the fundamental/intrinsic properties,

such as size, thickness, and the shape of the ultrathin 2D nanosheets are unstable and uncontrollable since the mechanical exfoliation technique by hand is shortage of precision and repeatability. Third, the utilized substrate is significantly important in the fabrication process. Recently, one advanced micromechanial cleavage method was reported by Sutter et al. to improve the production yield and increase the surface area of graphene and $Bi_2Sr_2CaCu_2O_x$ nanosheets [317]. The first significant key is using oxygen plasma to remove the ambient adsorbates on the substrate. Then a heat treatment is introduced during the fabrication process, which leads to a homogeneous interaction between the substrate and the crystal material [317]. Theoretically speaking, this advanced method can be further used to produce all kinds of ultrathin 2D nanosheets with larger area and enhanced production yield. Additionally, the evaporation of Au films onto SiO_2/Si before exfoliation is reported previously to enhance the surface area of TMD monolayers sine the interaction between Au and chalcogen layer is stronger, giving rise to a stronger contact between the substrate and TMD matrix process, which leads to a homogeneous interaction between the substrate and the crystal material [318].

4.2. Liquid Exfoliation

Liquid exfoliation actually also relies on the mechanical forces since the original idea of this technique is to apply the proper mechanical force on layered bulk crystals dispersed in liquid to exfoliate them into single- or few-layer 2D nanosheets. Thus, this technique is mechanical force-assisted liquid exfoliation, which can categorize into sonication-assisted liquid exfoliation and shear force-assisted liquid exfoliation. Compared to mechanical exfoliation of 2D nanosheets, liquid exfoliation is a reliable method with high quality and large quantity to produce mono and few-layer 2D sheets at bulk scale. Up to now, the exfoliation method in liquid media has been largely reported to gain ultrathin 2D materials from for their parental layered bulk crystals, such as MoS_2, WS_2, Bi_2Te_3, $MoSe_2$, $NbSe_2$, $TeSe_2$, *h*-BN, $NiTe_2$, $MoTe_2$ and so on [319–321].

Sonication-assisted liquid exfoliation is an established technique using the simple and common mechanical force to peel the layered bulk materials into 2D sheets in liquid media, in which the bulk crystals are dispersed into polar solvent and washed using bubbles induced by sonication in the solution. The cavitation bubbles generated by high energy ultrasonic waves could create high energy during the sudden burst with the release of pressure, hence the resultant dispersion is centrifuged to exfoliate layers in the solution. It is to be noted that the key parameter is the surface energies between the layered bulk materials and the liquid system should be matched. It is because the solvents have the surface tension, using the surface tension of solvent similar to the surface energy of layer bulk crystals could reduce the energetic cost of exfoliation and prohibit the restacking and aggregating between the 2D layers [82,319,322]. For example, it is reported that pure water or pure ethanol is not an efficient way to synthesize TMDs nanosheets due to the large surface energy of the solvent, but the mixing water with ethanol could effectively exfoliate and disperse TMDs. Thus, choosing the optimum solvent could largely utilize the potential of this technique. In addition, the sonication time and centrifugation rate are also significant factors, which are related to the quality and quantity of 2D materials. This method is first used to exfoliate graphite into graphene in 2008 [323]. They reported no that complicated equipment or expensive chemicals were used during their experiment. Subsequently, more than 25 solvents were studied to naturally exfoliate 2D nanosheets based on crystallinity, thickness, size and yield of the resultant layers [319]. It is summarized that dimethylformamide, cyclohexyl-pyrrolidinone, N-methyl-pyrrolidone, Ndodecyl-pyrrolidone, MDSO, NVP, ortho-dichlorobenzene and IPA are the most used solvents for ultrasonic exfoliation of MoS_2, WS_2, VS_2, *h*-BN and $MoTe_2$ [319,324–326]. The sonication-assisted liquid exfoliation as a simple method with high effectivity without complex equipment has paved a new way for large scale and high-yielding exfoliation of layered materials into ultrathin 2D monolayers.

Although the production of 2D nanosheets is increased with concentrations of $\sim$1 mg mL^{-1} by using the sonication-assisted liquid exfoliation method compared to the mechanical cleavage method, the production rate does not reach the industrial application's requirement. Hence, the shear

force-assisted liquid exfoliation method is proposed to further enhance the production rate of 2D nanosheets. Coleman et al. found that a high-shear rotor-stator mixer could create high shear rates in solvent containing bulk layered materials [327,328]. Similarly, the suitable solvent and polymer could minimize the exfoliation energy and stabilize the synthesized 2D nanosheets, leading to a more efficient exfoliation process. The shear-force device is set using a rotor and a stator to form a mixing head, which could exfoliate graphite into graphene with a lateral size of 300-800 nm in N-methyl-pyrrolidone [328]. Particularly, the volume of graphene production can be adjusted by tuning the size of the rotor. Therefore, the effects of rotor size and property of mixer-induced shear force were comprehensively studied previously [329]. It is demonstrated that the exfoliation of the bulk layered crystals is highly controlled by shear rate and that if it is lower than 10^4 S^{-1}, the production efficiency would be lower. However, when the shear rate is large than 10^4 S^{-1}, the exfoliation efficiency of graphene will be largely improved [329]. Broadly speaking, the production rate of graphene nanosheets is not only related to the rotor speed, but also with the nanomaterial concentration, volume of solution and mixing time. Currently, the production rate of graphene could reach up to 1.44 g h^{-1} with a thickness of 2–12 layers and length of 40–200 nm. These results demonstrate the commercial potential application of the shear force-assisted liquid exfoliation method for the high-yield and large-scale production of graphene.

4.3. Chemical Vapor Deposition

The chemical vapor deposition (CVD) technique is a common and traditional method to synthesize high-purity 2D layers of metal with large area and uniform thickness, such as Ti, W, Zr and Si on substrates, for large-scale electronic and flexible optoelectronic devices [330]. The CVD technique was first commercially applied in 1897 to reduce WO_6 in order to coat pure W on carbon filament [331]. Over the past decade, the highly purified polycrystalline Si has been largely produced using the CVD method in industry. In addition, the CVD method is already a reliable and developed technique for massive production of a mount of ultrathin nanosheets [330]. The growth of few-layer graphene on the polycrystalline Ni film by CVD method was first reported by Somani et al. in 2006 [332]. Subsequently, the graphene monolayer is obtained by the CVD technique on a Ni film deposited on SiO_2/Si substrate [333]. Here, not only did the Ni file played a role of substrate to support the growth of graphene, but it also acted as a catalyst to promote the formation of precursors to nuclear graphene sheets. Notably, the precursors, Ni film deposited on SiO_2/Si substrate, temperature, catalysts and atmospheres are the critical parameters to determine the structure property of graphene in CVD growth [334]. Thus, the production of graphene with controlled layer number, size and crystallinity can be obtained by optimizing those experimental parameters by the CVD method [333,334]. Similarly, the growth of a large number of 2D nanosheets is achieved on different substrates with different precursors in the CVD growth, including *h*-BN [335,335], Bi_2Se_3 [336], In_2Se_3 [337], borophenes [338], metal carbides [339,340] and silicene [341]. Taking MoS_2 nanosheets as an example, first the Mo metal film was deposited on SiO_2 substrate by an e-beam evaporator. Then S atoms were heated to 750 °C to generate vapor to react with Mo metal film to form large-area few-layer MoS_2 nanosheets [342]. In addition, controlling the thickness of the Mo thin layer as well as the size of the substrate could roughly adjust the size and thickness of MoS_2. Until now, MoS_2, WS_2, ZrS_2, ReS_2, $MoSe_2$, WSe_2 and so on have been successfully synthesized using the CVD technique on different substrates under different temperatures and atmosphere [342–347]. In addition, the CVD method exhibits the highest control ability than other synthetic methods to obtain 2D nanosheets with high crystal quality, high purity. Thus 2D nanomaterials synthesized by the CVD method are ideal candidates for fabrication of high performance electronic devices. More importantly, the CVD technique shows promising potential to produce ultrathin 2D sheets at an industrial scale with high yield and high production rate. However, the growth of 2D sheets by the CVD method should be deposited on substrates under high temperature and inert atmosphere, giving rise up to an expensive cost.

4.4. Van der Waal Epitaxial Growth on Substrate

There is one important synthesized form for the CVD method, and that is the van der Waal epitaxial growth on substrate in which the substrate surface usually plays as a seed crystal. However, it is known that the substrate often acts as a catalyst. The most predominant of van der Waal epitaxial growth on substrate is to grow large aspect ratio 2D nanosheets. The epitaxial growth of atom thick, in-plane heterostructure of graphene and *h*-BN was reported previously by Liu et al. [348]. Surprisingly, the orientation of *h*-BN material was dominated by graphene. In addition, this method was employed under UHV conditions with a pressure of 4×10^{-11} to fabricate periodically rippled graphene and islands on Ru(0001) by Vazquez de Parga et al. [349]. In this experiment, the C_2H_4 molecules were used as a precursor, while Ru as substrates. In detail, graphene monolayers are prepared by thermal decomposition of C_2H_4 at 1000 K, which is pre-adsorbed on Ru substrate [349]. In addition, it is demonstrated that single crystalline Ir can also be used as substrates for synthesis of the high quality atom thick, large area graphene monolayer [349]. Recent studies have proven that some 2D heteronanostructures can be obtained by van der Waal epitaxial growth of other TMDs on existing TMD nanosheets, such as WSe_2/WS_2, $MoSe_2/MoS_2$ and $MoSe_2/WSe_2$ [350–353]. Importantly, it is demonstrated that van der Waal epitaxial modes of lateral and vertical growth can be finely controlled to grow TMD heteronanostructures by adjusting the experimental conditions in the CVD technique [353]. The obtained lateral and vertical specifications are considered as a kind of p-n junction due to the different band gaps of different ultrathin 2D TMDs, which are promising candidates for utilizing in high-performance electronic devices as electronics or optoelectronics [354].

4.5. Hydrothermal Synthesis

Hydrothermal synthesis is another popular bottom-up method to crystallize substance at high pressure and high temperature. Particularly, it is suitable to synthesize the materials that possess high vapor pressure at the melting point. In addition, layered 2D nanosheets could be synthesized using the hydrothermal method. Taking MoS_2 as an example, MoO_3 or ammonium molybdate as the precursor of Mo and sulfur powder or potassium thiocyanate (KSCN) as the precursor of S are dissolved in hydrazine monohydrate solvent at 150-180 °C for 48 h for a full chemical reaction, then the Mo_2 and $MoSe_2$ monolayers can be initially synthesized and aggregated to form nanoflowers or nanotubes. [355]. It is worth to mention there is no tendency to restack in Mo_2 and $MoSe_2$ monolayers if not using surfactant. In addition, there are more intrinsic defects on TMDs by employing excess thiourea as a precursor to form the 2D nanosheets, which could provide more active sites of TMDs for catalytic applications [141]. Furthermore, Xie et al. applied a hydrothermal method to obtain O incorporated MoS_2 monolayer in water at 200 °C with the interlayer spacing of 9.5 Å, which is larger than 6.15 Å of pristine MoS_2 [356]. On the other hand, hydrothermal synthesis could generate a hybrid 1T/2H phase in the existing MoS_2 monolayers by a second solvothermal treatment [357]. The mixed 2H and 1T phase of MoS_2 nanosheets shows a robust ferromagnetism feature at room temperature due to the metallic property of the 1T MoS_2 monolayer. Subsequently, the hydrothermal-solvothermal approach is widely used to fabricate hybridization MoS_2-based adsorbents with other functional nanosheets, such as nano-Fe_3O_4 [358]. Groups IV and V transition metal chalcogenides from metal chloride can also be obtained hydrothermally/solvothermally in oleylamine [359]. CS_2 is used as the source of S atoms since it could produce H_2S, which could further react with the precursor of groups IV or V transition metal to form metal disulfides nanomaterials. Moreover, CSe_2, the precursor of Se gives a better layered crystalline structure than CS_2 due to the high structure stability of CSe_2 [359,360].

The hydrothermal method has recently been widely used in industrial incubation to large-scale synthesize nanosheets. For example, *h*-BN can be largely produced at 500 °C using boric anhydride, Zn powder and $N_2H_4\cdot2HCl$ or boric acid and urea at 900 °C [361]. In addition, TMDs, transition metal oxides and hydroxides have been extensively prepared on the gram scale via the hydrothermal method. Eu doped yttrium hydroxide nanomaterials can also be obtained hydrothermally/solvothermally using triethylamine as an alkaline and complexing source [362]. The VO_2 nanoribbons were prepared

under the hydrothermal reduction of V_2O_5 and graphene oxide. The thickness, width and length of VO_2 nanosheets could reach up to ~10 nm, 50–500 nm and ~10 μm, respectively, which could be used as a cathode in lithium ion batteries [363]. The more complex composites of $FeNi_2S_4$–graphene–MoS_2 and $FeNi_2S_4$–graphene–$MoSe_2$ can also be synthesized by using the hydrothermal method [364,365]. The hydrothermal synthesis method has a lot of advantages to synthesize ultrathin 2D nanosheets due to the fact that the process is simple, stable and scalable. Whereas, the micro growth mechanism of the hydrothermal method is hard to figure out in that the whole reaction happens in a sealed autoclave. More important, the hydrothermal synthesis method is very sensitive to the concentration of precursors, the solvent system, temperature, as well as whether surfactants or polymers are used, so it is difficult to design an experiment to produce other 2D nanosheets.

5. Conclusions, Perspectives and Challenges

In summary, we have attempted to provide a panorama of basic principles and mechanisms with regard to improving the structure stability, physical and chemical properties of low dimensional semiconductor-based photocatalysts. After reporting on a large amount of literature, various 2D semiconductor-based photocatalysts show a high electrochemical property and photocatalytic performance due to their ultrathin character, high specific surface area with more activity sites, tunable bandgap to absorb sunlight and versatile options in structural assembly with other nanosheets. Particularly, special focus has been placed on various strategies implemented to tackle problems associated with synthetic methods, structural stability and property, durability and photodecomposition of 2D semiconductors. From above, one can know extensive efforts have been devoted in the last few decades to construct various photocatalytic 2D semiconductors. Yet, co-photocatalysts made up of earth-abundant elements with low-cost are still required to further investigate and develop a mechanistic understanding and controllable synthetic strategy in order to achieve high-efficiency, stable and less costly 2D semiconductor-based photocatalysts. Many challenges, such as the low yield efficiency, stability, durability against etchant solution, kinetics of charge carriers absorption and migration, charge trap and recycling demand, need to be settled urgently in the near future.

Concurrently, advanced methods for tailoring the electronic and chemical structures of these 2D semiconductor materials have been developed, pushing its rapid development in various photocatalytic applications. For example, homogeneous doping has become a reality [66,366], but how to identify the dopand-induced electronic structures and what is the effect of doping elements on the stability of the system under reaction conditions are rarely being investigated. Until now, only a few examples of improved photocatalyst stability of photocatalysts have been reported in order to deal with the complicated synthetic processes during splitting water. Thus, the present studies on 2D semiconductor photocatalysts are still in the initial stage and further systematic investigations are required. On the other hand, in order to precisely control the dopant distribution, uniformity, composition and the surface states property of photocatalysts, seeking new doping approaches should be addressed for efficient photocatalyst design. In addition, the influence of intrinsic defects, structural shape, the quantity of layers and lateral interface size is barely evaluated on the photocatalytic performance, especially in composite photocatalysts. Importantly, an overall apparent efficiency of the entire photocatalytic system is the main topic in the current studies. While the charge transfer process, such as transfer minimum energy pathways, migration diffusivity, charge carrier lifetime recombination reason, etc., in photocatalysts should be addressed and detailedly investigated to further advance the field. With regard to the recycling problem, designing suitable devices or tuning the magnetic properties might be a good choice.

In the theoretical aspect, first-principles calculations based on density functional theory (DFT) are an efficient way to screen the photocatalytic potential spaces, however, a number of key bottlenecks are required to breakthrough. Firstly, the solvation effects are not considered in most of the present theoretical studies. Whereas it is well known that most photocatalytic reactions are related to solid–liquid reaction systems. Hence, it is significantly important and necessary to develop an

accurate solvation model as realistically as possible. For example, how the various molecules adsorb on the photocatalyst and influence the calculation of reaction energy and energy barrier heights should be considered in the photocatalyst system in order to realistically simulate the experimental testing conditions. Secondly, various previous theoretical data use the traditional DFT method, whereas the enlightenment of photocatalytic kinetic studies is still rarely studied due to the fact that it is technically challenging. The photoexcitation of a semiconductor photocatalyst, including 1D, 2D and 3D materials, produces photogenerated electrons and holes, leading to an excited state of the photocatalyst. However, the feature of the excited state and the corresponding reason for the energy barrier reduction under light irradiation are still secrets. Therefore, understanding the dynamics of excited electrons plays a significant role in understanding the whole photocatalytic processes [367,368]. Thirdly, the thermodynamic photocatalytic processess, such as energetic requirement, band edge alignment relative to the hydrogen revolution potential of H_2/H^+ and oxygen revolution potential of H_2O/O_2 needs to be deeply understood. For example, the migration behaviors of electrons and holes from substrates are not given much attention, which exhibits significant impacts on photocatalytic efficiency since 2D atomic thin photocatalysts are usually stabilized on various substrates. Last but not least, novel simulation methods or performing dynamic simulation algorithms rather than static crystal models are strongly required since the surfaces of photocatalysts are dynamically and frequently undergoing changes during the reaction proceeds. With rapid advances and rich knowledge about 2D materials in the many joint efforts of research and development sectors in the last few decades, it is the best time for us to do research on photocatalysis. At the same time, one can envision that utilization of the absorbed sunlight energy could largely reduce the fossil energy demand for human development, and further decrease the environmental pollution. Thus one can see photocatalysts play an increasingly important role in that we not only need to improve the performance of the existing photocatalysts but also invent new engineering approaches to better exploit new novel photocatalysts. Thus, joint efforts from various disciplines are needed. We wish that the present mini review serves as a catalyst to facilitate the discussions by various specialists from physics, chemistry, materials engineering, computer science, and so on.

Author Contributions: R.A. done the conception, designed & supervision. X.Y. wrote the first draft of the review. D.S. helped to improve the content of the article. All authors reviewed the manuscript. All authors have read and agreed to the published version of the manuscript.

Funding: This research received no external funding.

Acknowledgments: D.S. and R.A. thanks Olle Engkvists stiftelse (198-0390), Carl Tryggers Stiftelse for Vetenskaplig Forskning (CTS: 18:4) and Swedish Research Council (VR-2016-06014) for financial support. X.Y. sincerely appreciate the financial support by the National Natural Science Foundation of China (Grant No. 11705152 and 11625415) and Longshan academic talent research supporting program of Southwest University of Science and Technology (Grant No. 18LZX513 and 18LZXT04), and X.Y. gratefully acknowledges the financial support from the China Scholarship Council. SNIC and HPC2N are acknowledged for providing the computing facilities.

Conflicts of Interest: The authors have no conflict of interest.

References

1. Conti, J.; Holtberg, P.; Diefenderfer, J.; LaRose, A.; Turnure, J.T.; Westfall, L. *International Energy Outlook 2016 with Projections to 2040*; Technical Report; USDOE Energy Information Administration (EIA): Washington, DC, USA, 2016; Office of Energy Analysis.
2. Yang, X.; Yang, Y.; Lu, Y.; Sun, Z.; Hussain, S.; Zhang, P. First-principles GGA+U calculation investigating the hydriding and diffusion properties of hydrogen in PuH_{2+x}, $0 \leq x \leq 1$. *Int. J. Hydrogen Energy* **2018**, *43*, 13632–13638. [CrossRef]
3. Qu, Y.; Duan, X. Progress, challenge and perspective of heterogeneous photocatalysts. *Chem. Soc. Rev.* **2013**, *42*, 2568–2580. [CrossRef] [PubMed]

4. Colmenares, J.C.; Luque, R.; Campelo, J.M.; Colmenares, F.; Karpiński, Z.; Romero, A.A. Nanostructured photocatalysts and their applications in the photocatalytic transformation of lignocellulosic biomass: An overview. *Materials* **2009**, *2*, 2228–2258. [CrossRef]
5. Yang, X.; Lu, Y.; Zhang, P. First-principles study of native point defects and diffusion behaviors of helium in zirconium carbide. *J. Nucl. Mater.* **2015**, *465*, 161–166. [CrossRef]
6. Graetzel, M. Artificial photosynthesis: Water cleavage into hydrogen and oxygen by visible light. *Accounts Chem. Res.* **1981**, *14*, 376–384. [CrossRef]
7. Walter, M.G.; Warren, E.L.; McKone, J.R.; Boettcher, S.W.; Mi, Q.; Santori, E.A.; Lewis, N.S. Solar water splitting cells. *Chem. Rev.* **2010**, *110*, 6446–6473. [CrossRef] [PubMed]
8. Armelao, L.; Barreca, D.; Bottaro, G.; Gasparotto, A.; Maccato, C.; Maragno, C.; Tondello, E.; Štangar, U.L.; Bergant, M.; Mahne, D. Photocatalytic and antibacterial activity of TiO_2 and Au/TiO_2 nanosystems. *Nanotechnology* **2007**, *18*, 375709. [CrossRef]
9. Folli, A.; Pade, C.; Hansen, T.B.; De Marco, T.; Macphee, D.E. TiO_2 photocatalysis in cementitious systems: Insights into self-cleaning and depollution chemistry. *Cement Concerte Res.* **2012**, *42*, 539–548. [CrossRef]
10. Yue, X.Q. Effect of ZnO-loading method on adsorption and decomposition capacities of expanded graphite/ZnO composites for crude oil. *Adv. Mater. Res. Trans. Tech. Publ.* **2011**, *284*, 173–176. [CrossRef]
11. Kwon, S.; Fan, M.; Cooper, A.T.; Yang, H. Photocatalytic applications of micro-and nano-TiO_2 in environmental engineering. *Crit. Rev. Environ. Sci. Technol.* **2008**, *38*, 197–226. [CrossRef]
12. Cai, R.; Hashimoto, K.; Kubota, Y.; Fujishima, A. Increment of photocatalytic killing of cancer cells using TiO_2 with the aid of superoxide dismutase. *Chem. Lett.* **1992**, *21*, 427–430. [CrossRef]
13. Tian, C.Y.; Xu, J.J.; Chen, H.Y. A novel aptasensor for the detection of adenosine in cancer cells by electrochemiluminescence of nitrogen doped TiO_2 nanotubes. *Chem. Commun.* **2012**, *48*, 8234–8236. [CrossRef]
14. Kudo, A.; Miseki, Y. Heterogeneous photocatalyst materials for water splitting. *Chem. Soc. Rev.* **2009**, *38*, 253–278. [CrossRef] [PubMed]
15. Ganguly, P.; Byrne, C.; Breen, A.; Pillai, S.C. Antimicrobial activity of photocatalysts: Fundamentals, mechanisms, kinetics and recent advances. *Appl. Catal. B Environ.* **2018**, *225*, 51–75. [CrossRef]
16. Yalavarthi, R.; Naldoni, A.; Kment, Š.; Mascaretti, L.; Kmentová, H.; Tomanec, O.; Schmuki, P.; Zbořil, R. Radiative and non-radiative recombination pathways in mixed-phase TiO_2 nanotubes for PEC water-splitting. *Catalysts* **2019**, *9*, 204. [CrossRef]
17. Fujishima, A.; Honda, K. Electrochemical photolysis of water at a semiconductor electrode. *Nature* **1972**, *238*, 37–38. [CrossRef]
18. Yuan, Y.J.; Chen, D.; Yu, Z.T.; Zou, Z.G. Cadmium sulfide-based nanomaterials for photocatalytic hydrogen production. *J. Mater. Chem. A* **2018**, *6*, 11606–11630. [CrossRef]
19. Tong, H.; Ouyang, S.; Bi, Y.; Umezawa, N.; Oshikiri, M.; Ye, J. Nano-photocatalytic materials: Possibilities and challenges. *Nat. Rev. Mater.* **2012**, *24*, 229–251. [CrossRef] [PubMed]
20. Zhang, N.; Wang, L.; Wang, H.; Cao, R.; Wang, J.; Bai, F.; Fan, H. Self-assembled one-dimensional porphyrin nanostructures with enhanced photocatalytic hydrogen generation. *Nano Lett.* **2018**, *18*, 560–566. [CrossRef]
21. Ma, Y.; Wang, X.; Jia, Y.; Chen, X.; Han, H.; Li, C. Titanium dioxide-based nanomaterials for photocatalytic fuel generations. *Chem. Rev.* **2014**, *114*, 9987–10043. [CrossRef]
22. Che, W.; Cheng, W.; Yao, T.; Tang, F.; Liu, W.; Su, H.; Huang, Y.; Liu, Q.; Liu, J.; Hu, F.; et al. Fast photoelectron transfer in (Cring)-C_3N_4 plane heterostructural nanosheets for overall water splitting. *J. Am. Chem. Soc.* **2017**, *139*, 3021–3026. [CrossRef]
23. Cai, X.; Zhu, M.; Elbanna, O.A.; Fujitsuka, M.; Kim, S.; Mao, L.; Zhang, J.; Majima, T. Au nanorod photosensitized $La_2Ti_2O_7$ nanosteps: successive surface heterojunctions boosting visible to near-infrared photocatalytic H_2 evolution. *ACS Catal.* **2018**, *8*, 122–131. [CrossRef]
24. Singh, D.; Panda, P.K.; Khossossi, N.; Mishra, Y.K.; Ainane, A.; Ahuja, R. Impact of edge structures on interfacial interactions and efficient visible-light photocatalytic activity of metal–semiconductor hybrid 2D materials. *Catal. Sci. Technol.* **2020**, *10*, 3279–3289.
25. Singh, D.; Chakraborty, S.; Ahuja, R. Emergence of Si_2BN Monolayer as Efficient HER Catalyst under Co-functionalization Influence. *ACS Appl. Energy Mater.* **2019**, *2*, 8441–8448. [CrossRef]
26. Hartley, C.L.; DiRisio, R.J.; Screen, M.E.; Mayer, K.J.; McNamara, W.R. Iron polypyridyl complexes for photocatalytic hydrogen generation. *Inorg. Chem.* **2016**, *55*, 8865–8870. [CrossRef] [PubMed]

27. Zhang, L.Y.; Yin, S.Y.; Pan, M.; Liao, W.M.; Zhang, J.H.; Wang, H.P.; Su, C.Y. Binuclear Ru–Ru and Ir–Ru complexes for deep red emission and photocatalytic water reduction. *J. Mater. Chem. A* **2017**, *5*, 9807–9814.
28. Greene, B.L.; Schut, G.J.; Adams, M.W.; Dyer, R.B. Pre-Steady-State Kinetics of Catalytic Intermediates of an [FeFe]-Hydrogenase. *ACS Catal.* **2017**, *7*, 2145–2150. [CrossRef]
29. Singh, D.; Gupta, S.K.; Sonvane, Y.; Kumar, A.; Ahuja, R. 2D-HfS_2 as an efficient photocatalyst for water splitting. *Catal. Sci. Technol.* **2016**, *6*, 6605–6614.
30. Zhao, X.; Yang, X.; Singh, D.; Panda, P.K.; Luo, W.; Li, Y.; Ahuja, R. Strain-Engineered Metal-Free *h*-B_2O Monolayer as a Mechanocatalyst for Photocatalysis and Improved Hydrogen Evolution Reaction. *J. Phys. Chem. C* **2020**, *124*, 7884–7892. [CrossRef]
31. Hutton, G.A.; Reuillard, B.; Martindale, B.C.; Caputo, C.A.; Lockwood, C.W.; Butt, J.N.; Reisner, E. Carbon dots as versatile photosensitizers for solar-driven catalysis with redox enzymes. *J. Am. Chem. Soc.* **2016**, *138*, 16722–16730. [CrossRef] [PubMed]
32. Lv, H.; Ruberu, T.P.A.; Fleischauer, V.E.; Brennessel, W.W.; Neidig, M.L.; Eisenberg, R. Catalytic light-driven generation of hydrogen from water by iron dithiolene complexes. *J. Am. Chem. Soc.* **2016**, *138*, 11654–11663. [CrossRef] [PubMed]
33. Yuan, Y.J.; Chen, D.Q.; Xiong, M.; Zhong, J.S.; Wan, Z.Y.; Zhou, Y.; Liu, S.; Yu, Z.T.; Yang, L.X.; Zou, Z.G. Bandgap engineering of $(AgIn)_xZn_{2(1-x)}S_2$ quantum dot photosensitizers for photocatalytic H_2 generation. *Appl. Catal. B Environ.* **2017**, *204*, 58–66. [CrossRef]
34. Sakai, T.; Mersch, D.; Reisner, E. Photocatalytic hydrogen evolution with a hydrogenase in a mediator-free system under high levels of oxygen. *Angew. Chem.* **2013**, *52*, 12313–12316.
35. Han, Z.; Shen, L.; Brennessel, W.W.; Holland, P.L.; Eisenberg, R. Nickel pyridinethiolate complexes as catalysts for the light-driven production of hydrogen from aqueous solutions in noble-metal-free systems. *J. Am. Chem. Soc.* **2013**, *135*, 14659–14669. [CrossRef] [PubMed]
36. Yuan, Y.J.; Lu, H.W.; Tu, J.R.; Fang, Y.; Yu, Z.T.; Fan, X.X.; Zou, Z.G. A Noble-Metal-Free Nickel (II) Polypyridyl Catalyst for Visible-Light-Driven Hydrogen Production from Water. *ChemPhysChem* **2015**, *16*, 2925–2930. [CrossRef]
37. Kagalwala, H.N.; Chirdon, D.N.; Mills, I.N.; Budwal, N.; Bernhard, S. Light-driven hydrogen generation from microemulsions using metallosurfactant catalysts and oxalic acid. *Inorg. Chem.* **2017**, *56*, 10162–10171. [CrossRef]
38. Yuan, Y.J.; Ye, Z.J.; Lu, H.W.; Hu, B.; Li, Y.H.; Chen, D.Q.; Zhong, J.S.; Yu, Z.T.; Zou, Z.G. Constructing anatase TiO_2 nanosheets with exposed (001) facets/layered MoS_2 two-dimensional nanojunctions for enhanced solar hydrogen generation. *ACS Catal.* **2016**, *6*, 532–541. [CrossRef]
39. Lin, Z.; Xiao, J.; Li, L.; Liu, P.; Wang, C.; Yang, G. Nanodiamond-Embedded p-Type Copper (I) Oxide Nanocrystals for Broad-Spectrum Photocatalytic Hydrogen Evolution. *Adv. Energy Mater.* **2016**, *6*, 1501865. [CrossRef]
40. Wang, Q.; Hisatomi, T.; Jia, Q.; Tokudome, H.; Zhong, M.; Wang, C.; Pan, Z.; Takata, T.; Nakabayashi, M.; Shibata, N.; et al. Scalable water splitting on particulate photocatalyst sheets with a solar-to-hydrogen energy conversion efficiency exceeding 1%. *Nat. Mater.* **2016**, *15*, 611–615. [CrossRef]
41. Liu, L.; Peter, Y.Y.; Chen, X.; Mao, S.S.; Shen, D. Hydrogenation and disorder in engineered black TiO_2. *Phys. Rev. Lett.* **2013**, *111*, 065505.
42. Xu, M.; Gao, Y.; Moreno, E.M.; Kunst, M.; Muhler, M.; Wang, Y.; Idriss, H.; Wöll, C. Photocatalytic activity of bulk TiO_2 anatase and rutile single crystals using infrared absorption spectroscopy. *Phys. Rev. Lett.* **2011**, *106*, 138302. [CrossRef] [PubMed]
43. Li, X.; Li, Z.; Yang, J. Proposed photosynthesis method for producing hydrogen from dissociated water molecules using incident near-infrared light. *Phys. Rev. Lett.* **2014**, *112*, 018301. [CrossRef] [PubMed]
44. Ahmed, M.; Guo, X. A review of metal oxynitrides for photocatalysis. *Inorg. Chem. Front.* **2016**, *3*, 578–590. [CrossRef]
45. Yang, X.; Banerjee, A.; Ahuja, R. Probing the active sites of newly predicted stable Janus scandium dichalcogenides for photocatalytic water-splitting. *Catal. Sci. Technol.* **2019**, *9*, 4981–4989. [CrossRef]
46. Serpone, N.; Emeline, A.; Ryabchuk, V.; Kuznetsov, V. Why do hydrogen and oxygen yields from semiconductor-based photocatalyzed water splitting remain disappointingly low? Intrinsic and extrinsic factors impacting surface redox reactions. *ACS Energy Lett.* **2016**, *1*, 931–948. [CrossRef]

47. Fukuzumi, S.; Hong, D.; Yamada, Y. Bioinspired photocatalytic water reduction and oxidation with earth-abundant metal catalysts. *J. Phys. Chem. Lett.* **2013**, *4*, 3458–3467. [CrossRef]
48. Guzman, F.; Chuang, S.S.; Yang, C. Role of methanol sacrificing reagent in the photocatalytic evolution of hydrogen. *Ind. Eng. Chem. Res* **2013**, *52*, 61–65. [CrossRef]
49. Salzl, S.; Ertl, M.; Knör, G. Evidence for photosensitised hydrogen production from water in the absence of precious metals, redox-mediators and co-catalysts. *Phys. Chem. Chem. Phys.* **2017**, *19*, 8141–8147. [CrossRef]
50. Simon, T.; Bouchonville, N.; Berr, M.J.; Vaneski, A.; Adrović, A.; Volbers, D.; Wyrwich, R.; Döblinger, M.; Susha, A.S.; Rogach, A.L.; et al. Redox shuttle mechanism enhances photocatalytic H_2 generation on Ni-decorated CdS nanorods. *Nat. Mater.* **2014**, *13*, 1013–1018. [CrossRef]
51. Wang, J.; Chen, Y.; Zhou, W.; Tian, G.; Xiao, Y.; Fu, H.; Fu, H. Cubic quantum dot/hexagonal microsphere $ZnIn_2$ S_4 heterophase junctions for exceptional visible-light-driven photocatalytic H_2 evolution. *J. Mater. Chem. A* **2017**, *5*, 8451–8460. [CrossRef]
52. Wang, X.; Maeda, K.; Thomas, A.; Takanabe, K.; Xin, G.; Carlsson, J.M.; Domen, K.; Antonietti, M. A metal-free polymeric photocatalyst for hydrogen production from water under visible light. *Nat. Mater.* **2009**, *8*, 76–80. [CrossRef]
53. Han, Z.; Qiu, F.; Eisenberg, R.; Holland, P.L.; Krauss, T.D. Robust photogeneration of H_2 in water using semiconductor nanocrystals and a nickel catalyst. *Science* **2012**, *338*, 1321–1324. [CrossRef]
54. Xu, J.; Cao, X. Characterization and mechanism of MoS_2/CdS composite photocatalyst used for hydrogen production from water splitting under visible light. *Chem. Eng. J.* **2015**, *260*, 642–648. [CrossRef]
55. Kim, W.; Tachikawa, T.; Majima, T.; Li, C.; Kim, H.J.; Choi, W. Tin-porphyrin sensitized TiO_2 for the production of H_2 under visible light. *Energy Environ. Sci.* **2010**, *3*, 1789–1795. [CrossRef]
56. Ye, C.; Li, J.X.; Li, Z.J.; Li, X.B.; Fan, X.B.; Zhang, L.P.; Chen, B.; Tung, C.H.; Wu, L.Z. Enhanced driving force and charge separation efficiency of protonated *g*-C_3N_4 for photocatalytic O_2 evolution. *ACS Catal.* **2015**, *5*, 6973–6979. [CrossRef]
57. Asahi, R.; Morikawa, T.; Ohwaki, T.; Aoki, K.; Taga, Y. Visible-light photocatalysis in nitrogen-doped titanium oxides. *Science* **2001**, *293*, 269–271. [CrossRef] [PubMed]
58. Yang, X.; Banerjee, A.; Xu, Z.; Wang, Z.; Ahuja, R. Interfacial aspect of ZnTe/In_2Te_3 heterostructures as an efficient catalyst for the hydrogen evolution reaction. *J. Mater. Chem. A* **2019**, *7*, 27441–27449. [CrossRef]
59. Wen, C.Z.; Hu, Q.H.; Guo, Y.N.; Gong, X.Q.; Qiao, S.Z.; Yang, H.G. From titanium oxydifluoride ($TiOF_2$) to titania (TiO_2): phase transition and non-metal doping with enhanced photocatalytic hydrogen (H_2) evolution properties. *Chem. Commun.* **2011**, *47*, 6138–6140. [CrossRef]
60. Yu, J.; Zhang, J.; Jaroniec, M. Preparation and enhanced visible-light photocatalytic H_2-production activity of CdS quantum dots-sensitized $Zn_{1-x}Cd_xS$ solid solution. *Green Chem.* **2010**, *12*, 1611–1614. [CrossRef]
61. Ning, Z.; Tian, H.; Yuan, C.; Fu, Y.; Qin, H.; Sun, L.; Ågren, H. Solar cells sensitized with type-II ZnSe–CdS core/shell colloidal quantum dots. *Chem. Commun.* **2011**, *47*, 1536–1538. [CrossRef]
62. Chen, X.; Liu, L.; Peter, Y.Y.; Mao, S.S. Increasing solar absorption for photocatalysis with black hydrogenated titanium dioxide nanocrystals. *Science* **2011**, *331*, 746–750. [CrossRef] [PubMed]
63. Thimsen, E.; Le Formal, F.; Gratzel, M.; Warren, S.C. Influence of plasmonic Au nanoparticles on the photoactivity of Fe_2O_3 electrodes for water splitting. *Nano Lett.* **2011**, *11*, 35–43. [CrossRef] [PubMed]
64. Wu, H.B.; Hng, H.H.; Lou, X.W. Direct synthesis of anatase TiO_2 nanowires with enhanced photocatalytic activity. *Adv. Mater.* **2012**, *24*, 2567–2571. [CrossRef] [PubMed]
65. Chen, J.S.; Chen, C.; Liu, J.; Xu, R.; Qiao, S.Z.; Lou, X.W. Ellipsoidal hollow nanostructures assembled from anatase TiO_2 nanosheets as a magnetically separable photocatalyst. *Chem. Commun.* **2011**, *47*, 2631–2633. [CrossRef]
66. Meng, F.; Li, J.; Cushing, S.K.; Zhi, M.; Wu, N. Solar hydrogen generation by nanoscale p-n junction of p-type molybdenum disulfide/n-type nitrogen-doped reduced graphene oxide. *J. Am. Chem. Soc.* **2013**, *135*, 10286–10289. [CrossRef]
67. Wang, X.; Xu, Q.; Li, M.; Shen, S.; Wang, X.; Wang, Y.; Feng, Z.; Shi, J.; Han, H.; Li, C. Photocatalytic overall water splitting promoted by an α–β phase junction on Ga_2O_3. *Angew. Chem.* **2012**, *124*, 13266–13269. [CrossRef]
68. Konta, R.; Ishii, T.; Kato, H.; Kudo, A. Photocatalytic Activities of Noble Metal Ion Doped $SrTiO_3$ under Visible Light Irradiation. *J. Phys. Chem. B* **2004**, *108*, 8992–8995. [CrossRef]

69. Maeda, K.; Teramura, K.; Lu, D.; Takata, T.; Saito, N.; Inoue, Y.; Domen, K. Photocatalyst releasing hydrogen from water. *Nature* **2006**, *440*, 295–295. [CrossRef] [PubMed]
70. Maeda, K.; Teramura, K.; Lu, D.; Saito, N.; Inoue, Y.; Domen, K. Noble-metal/Cr_2O_3 core/shell nanoparticles as a cocatalyst for photocatalytic overall water splitting. *Angew. Chem.* **2006**, *118*, 7970–7973. [CrossRef]
71. Maeda, K.; Sakamoto, N.; Ikeda, T.; Ohtsuka, H.; Xiong, A.; Lu, D.; Kanehara, M.; Teranishi, T.; Domen, K. Preparation of Core–Shell-Structured Nanoparticles (with a Noble-Metal or Metal Oxide Core and a Chromia Shell) and Their Application in Water Splitting by Means of Visible Light. *Chem. Eur. J.* **2010**, *16*, 7750–7759. [CrossRef]
72. Qu, Y.; Liao, L.; Cheng, R.; Wang, Y.; Lin, Y.C.; Huang, Y.; Duan, X. Rational design and synthesis of freestanding photoelectric nanodevices as highly efficient photocatalysts. *Nano Lett.* **2010**, *10*, 1941–1949. [PubMed]
73. Yang, Z.; Zhang, J.; Kintner-Meyer, M.C.; Lu, X.; Choi, D.; Lemmon, J.P.; Liu, J. Electrochemical energy storage for green grid. *Chem. Rev.* **2011**, *111*, 3577–3613. [PubMed]
74. Zhou, H.; Qu, Y.; Zeid, T.; Duan, X. Towards highly efficient photocatalysts using semiconductor nanoarchitectures. *Energy Environ. Sci.* **2012**, *5*, 6732–6743.
75. Hochbaum, A.I.; Yang, P. Semiconductor nanowires for energy conversion. *Chem. Rev.* **2010**, *110*, 527–546. [PubMed]
76. Atwater, H.A.; Polman, A. Plasmonics for improved photovoltaic devices. In *Materials for Sustainable Energy: A Collection of Peer-Reviewed Research and Review Articles from Nature Publishing Group*; World Scientific: Singapore, 2011; pp. 1–11.
77. Tafen, D.N.; Long, R.; Prezhdo, O.V. Dimensionality of nanoscale TiO_2 determines the mechanism of photoinduced electron injection from a CdSe nanoparticle. *Nano Lett.* **2014**, *14*, 1790–1796.
78. She, X.; Wu, J.; Xu, H.; Zhong, J.; Wang, Y.; Song, Y.; Nie, K.; Liu, Y.; Yang, Y.; Rodrigues, M.T.F.; et al. High efficiency photocatalytic water splitting using 2D α-Fe_2O_3/g-C_3N_4 Z-scheme catalysts. *Adv. Energy Mater.* **2017**, *7*, 1700025.
79. Han, Q.; Wang, B.; Gao, J.; Cheng, Z.; Zhao, Y.; Zhang, Z.; Qu, L. Atomically thin mesoporous nanomesh of graphitic C_3N_4 for high-efficiency photocatalytic hydrogen evolution. *ACS Nano* **2016**, *10*, 2745–2751.
80. Sivula, K. Metal oxide photoelectrodes for solar fuel production, surface traps, and catalysis. *J. Phys. Chem. Lett.* **2013**, *4*, 1624–1633.
81. Hisatomi, T.; Kubota, J.; Domen, K. Recent advances in semiconductors for photocatalytic and photoelectrochemical water splitting. *Chem. Soc. Rev.* **2014**, *43*, 7520–7535.
82. Nicolosi, V.; Chhowalla, M.; Kanatzidis, M.G.; Strano, M.S.; Coleman, J.N. Liquid exfoliation of layered materials. *Science* **2013**, *340*, 1226419.
83. Son, J.S.; Yu, J.H.; Kwon, S.G.; Lee, J.; Joo, J.; Hyeon, T. Colloidal Synthesis of Ultrathin Two-Dimensional Semiconductor Nanocrystals. *Adv. Mater.* **2011**, *23*, 3214–3219. [PubMed]
84. Oh, S.M.; Patil, S.B.; Jin, X.; Hwang, S.J. Recent applications of 2D inorganic nanosheets for emerging energy storage system. *Chem. Eur. J.* **2018**, *24*, 4757–4773.
85. Zhang, H. Ultrathin two-dimensional nanomaterials. *ACS Nano* **2015**, *9*, 9451–9469.
86. Voiry, D.; Mohite, A.; Chhowalla, M. Phase engineering of transition metal dichalcogenides. *Chem. Soc. Rev.* **2015**, *44*, 2702–2712. [CrossRef]
87. Fan, Z.; Zhang, H. Crystal phase-controlled synthesis, properties and applications of noble metal nanomaterials. *Chem. Soc. Rev.* **2016**, *45*, 63–82. [PubMed]
88. Chhowalla, M.; Voiry, D.; Yang, J.; Shin, H.S.; Loh, K.P. Phase-engineered transition-metal dichalcogenides for energy and electronics. *MRS Bull.* **2015**, *40*, 585.
89. Ambrosi, A.; Sofer, Z.; Pumera, M. 2H $\rightarrow$ 1T phase transition and hydrogen evolution activity of MoS_2, $MoSe_2$, WS_2 and WSe_2 strongly depends on the MX_2 composition. *Chem. Commun.* **2015**, *51*, 8450–8453.
90. Chang, K.; Hai, X.; Pang, H.; Zhang, H.; Shi, L.; Liu, G.; Liu, H.; Zhao, G.; Li, M.; Ye, J. Targeted synthesis of 2H-and 1T-phase MoS_2 monolayers for catalytic hydrogen evolution. *Adv. Mater.* **2016**, *28*, 10033–10041. [PubMed]
91. Qu, Y.; Medina, H.; Wang, S.W.; Wang, Y.C.; Chen, C.W.; Su, T.Y.; Manikandan, A.; Wang, K.; Shih, Y.C.; Chang, J.W.; et al. Wafer Scale Phase-Engineered 1T-and 2H-$MoSe_2$/Mo Core–Shell 3D-Hierarchical Nanostructures toward Efficient Electrocatalytic Hydrogen Evolution Reaction. *Nat. Rev. Mater.* **2016**, *28*, 9831–9838. [CrossRef] [PubMed]

92. Tan, C.; Zhang, H. Wet-chemical synthesis and applications of non-layer structured two-dimensional nanomaterials. *Nat. Commun.* **2015**, *6*, 1–13.
93. Tuller, H.; Nowick, A. Defect structure and electrical properties of nonstoichiometric CeO_2 single crystals. *J. Electrochem. Soc.* **1979**, *126*, 209. [CrossRef]
94. Wells, A. *Structural Inorganic Chemistry*; Oxford University Press: Oxford, UK, 1984.
95. Balendhran, S.; Walia, S.; Nili, H.; Ou, J.Z.; Zhuiykov, S.; Kaner, R.B.; Sriram, S.; Bhaskaran, M.; Kalantar-zadeh, K. Two-dimensional molybdenum trioxide and dichalcogenides. *Adv. Funct. Mater.* **2013**, *23*, 3952–3970. [CrossRef]
96. Enjalbert, R.; Galy, J. A refinement of the structure of V_2O_5. *Acta Crystallogr. C* **1986**, *42*, 1467–1469. [CrossRef]
97. Shklover, V.; Haibach, T.; Ried, F.; Nesper, R.; Novak, P. Crystal Structure of the Product of Mg^{2+} Insertion into V_2O_5 Single Crystals. *J. Sold. State Chem.* **1996**, *123*, 317–323.
98. Qamar, S.; Lei, F.; Liang, L.; Gao, S.; Liu, K.; Sun, Y.; Ni, W.; Xie, Y. Ultrathin TiO_2 flakes optimizing solar light driven CO_2 reduction. *Nano Energy* **2016**, *26*, 692–698. [CrossRef]
99. Lei, F.; Sun, Y.; Liu, K.; Gao, S.; Liang, L.; Pan, B.; Xie, Y. Oxygen vacancies confined in ultrathin indium oxide porous sheets for promoted visible-light water splitting. *J. Am. Chem. Soc.* **2014**, *136*, 6826–6829. [CrossRef] [PubMed]
100. Gao, S.; Sun, Y.; Lei, F.; Liu, J.; Liang, L.; Li, T.; Pan, B.; Zhou, J.; Xie, Y. Freestanding atomically-thin cuprous oxide sheets for improved visible-light photoelectrochemical water splitting. *Nano Energy* **2014**, *8*, 205–213. [CrossRef]
101. Liao, T.; Sun, Z.; Dou, S.X. Theoretically manipulating quantum dots on two-dimensional TiO_2 monolayer for effective visible light absorption. *ACS Appl. Mater. Interfaces* **2017**, *9*, 8255–8262. [CrossRef]
102. Tan, C.; Cao, X.; Wu, X.J.; He, Q.; Yang, J.; Zhang, X.; Chen, J.; Zhao, W.; Han, S.; Nam, G.H.; et al. Recent advances in ultrathin two-dimensional nanomaterials. *Chem. Rev.* **2017**, *117*, 6225–6331. [CrossRef]
103. Han, X.; Kuang, Q.; Jin, M.; Xie, Z.; Zheng, L. Synthesis of titania nanosheets with a high percentage of exposed (001) facets and related photocatalytic properties. *J. Am. Chem. Soc.* **2009**, *131*, 3152–3153. [CrossRef]
104. Yu, J.; Qi, L.; Jaroniec, M. Hydrogen production by photocatalytic water splitting over Pt/TiO_2 nanosheets with exposed (001) facets. *J. Phys. Chem. C* **2010**, *114*, 13118–13125. [CrossRef]
105. Waller, M.R.; Townsend, T.K.; Zhao, J.; Sabio, E.M.; Chamousis, R.L.; Browning, N.D.; Osterloh, F.E. Single-crystal tungsten oxide nanosheets: Photochemical water oxidation in the quantum confinement regime. *Chem. Mater.* **2012**, *24*, 698–704. [CrossRef]
106. Zhou, Y.; Zhang, Y.; Lin, M.; Long, J.; Zhang, Z.; Lin, H.; Wu, J.C.S.; Wang, X. Monolayered Bi_2WO_6 nanosheets mimicking heterojunction interface with open surfaces for photocatalysis. *Nat. Commun.* **2015**, *6*, 1–8. [CrossRef] [PubMed]
107. Sato, J.; Saito, N.; Yamada, Y.; Maeda, K.; Takata, T.; Kondo, J.N.; Hara, M.; Kobayashi, H.; Domen, K.; Inoue, Y. RuO_2-loaded β-Ge_3N_4 as a non-oxide photocatalyst for overall water splitting. *J. Am. Chem. Soc.* **2005**, *127*, 4150–4151. [CrossRef] [PubMed]
108. Maeda, K.; Abe, R.; Domen, K. Role and function of ruthenium species as promoters with TaON-based photocatalysts for oxygen evolution in two-step water splitting under visible light. *J. Phys. Chem. C* **2011**, *115*, 3057–3064. [CrossRef]
109. Abe, R.; Shinmei, K.; Hara, K.; Ohtani, B. Robust dye-sensitized overall water splitting system with two-step photoexcitation of coumarin dyes and metal oxide semiconductors. *Chem. Commun.* **2009**, 3577–3579, doi:10.1039/B905935K . [CrossRef] [PubMed]
110. Youngblood, W.J.; Lee, S.H.A.; Kobayashi, Y.; Hernandez-Pagan, E.A.; Hoertz, P.G.; Moore, T.A.; Moore, A.L.; Gust, D.; Mallouk, T.E. Photoassisted overall water splitting in a visible light-absorbing dye-sensitized photoelectrochemical cell. *J. Am. Chem. Soc.* **2009**, *131*, 926–927. [CrossRef]
111. Cardon, F.; Gomes, W. On the determination of the flat-band potential of a semiconductor in contact with a metal or an electrolyte from the Mott-Schottky plot. *J. Phys. D Appl. Phys.* **1978**, *11*, L63. [CrossRef]
112. Xu, Y.; Schoonen, M.A. The absolute energy positions of conduction and valence bands of selected semiconducting minerals. *Am. Mineral.* **2000**, *85*, 543–556. [CrossRef]
113. Pan, L.; Kim, J.H.; Mayer, M.T.; Son, M.K.; Ummadisingu, A.; Lee, J.S.; Hagfeldt, A.; Luo, J.; Grätzel, M. Boosting the performance of Cu_2O photocathodes for unassisted solar water splitting devices. *Nat. Catal.* **2018**, *1*, 412–420. [CrossRef]

114. Sekizawa, K.; Nonaka, T.; Arai, T.; Morikawa, T. Structural improvement of $CaFe_2O_4$ by metal doping toward enhanced cathodic photocurrent. *ACS Appl. Mater. Interfaces* **2014**, *6*, 10969–10973. [CrossRef]
115. Masudy-Panah, S.; Eugene, Y.J.K.; Khiavi, N.D.; Katal, R.; Gong, X. Aluminum-incorporated p-CuO/n-ZnO photocathode coated with nanocrystal-engineered TiO_2 protective layer for photoelectrochemical water splitting and hydrogen generation. *J. Mater. Chem. A* **2018**, *6*, 11951–11965. [CrossRef]
116. Hong, S.J.; Lee, S.; Jang, J.S.; Lee, J.S. Heterojunction $BiVO_4/WO_3$ electrodes for enhanced photoactivity of water oxidation. *Energy Environ. Sci.* **2011**, *4*, 1781–1787. [CrossRef]
117. Yourey, J.E.; Bartlett, B.M. Electrochemical deposition and photoelectrochemistry of $CuWO_4$, a promising photoanode for water oxidation. *J. Mater. Chem.* **2011**, *21*, 7651–7660. [CrossRef]
118. Ding, K.; Chen, B.; Li, Y.; Zhang, Y.; Chen, Z. Comparative density functional theory study on the electronic and optical properties of $BiMO_4$ (M = V, Nb, Ta). *J. Mater. Chem. A* **2014**, *2*, 8294–8303. [CrossRef]
119. Pihosh, Y.; Turkevych, I.; Mawatari, K.; Uemura, J.; Kazoe, Y.; Kosar, S.; Makita, K.; Sugaya, T.; Matsui, T.; Fujita, D.; et al. Photocatalytic generation of hydrogen by core-shell $WO_3/BiVO_4$ nanorods with ultimate water splitting efficiency. *Sci. Rep.* **2015**, *5*, 11141. [CrossRef]
120. Whittles, T.J.; Veal, T.D.; Savory, C.N.; Welch, A.W.; de Souza Lucas, F.W.; Gibbon, J.T.; Birkett, M.; Potter, R.J.; Scanlon, D.O.; Zakutayev, A.; et al. Core levels, band alignments, and valence-band states in $CuSbS_2$ for solar cell applications. *ACS Appl. Mater. Interfaces* **2017**, *9*, 41916–41926. [CrossRef]
121. Li, J.; Wu, N. Semiconductor-based photocatalysts and photoelectrochemical cells for solar fuel generation: A review. *Catal. Sci. Technol.* **2015**, *5*, 1360–1384. [CrossRef]
122. Prévot, M.S.; Guijarro, N.; Sivula, K. Enhancing the performance of a robust sol–gel-processed p-type delafossite $CuFeO_2$ photocathode for solar water reduction. *ChemSusChem* **2015**, *8*, 1359–1367. [CrossRef]
123. Wang, F.; Septina, W.; Chemseddine, A.; Abdi, F.F.; Friedrich, D.; Bogdanoff, P.; van de Krol, R.; Tilley, S.D.; Berglund, S.P. Gradient self-doped $CuBi_2O_4$ with highly improved charge separation efficiency. *J. Am. Chem. Soc.* **2017**, *139*, 15094–15103. [CrossRef]
124. Aydinol, M.; Kohan, A.; Ceder, G.; Cho, K.; Joannopoulos, J. Ab initio study of lithium intercalation in metal oxides and metal dichalcogenides. *Phys. Rev. B* **1997**, *56*, 1354. [CrossRef]
125. Lopez-Sanchez, O.; Lembke, D.; Kayci, M.; Radenovic, A.; Kis, A. Ultrasensitive photodetectors based on monolayer MoS_2. *Nat. Nanotechnol.* **2013**, *8*, 497–501. [CrossRef] [PubMed]
126. Mak, K.F.; Lee, C.; Hone, J.; Shan, J.; Heinz, T.F. Atomically thin MoS_2: A new direct-gap semiconductor. *Phys. Rev. Lett.* **2010**, *105*, 136805. [CrossRef] [PubMed]
127. Chhowalla, M.; Shin, H.S.; Eda, G.; Li, L.J.; Loh, K.P.; Zhang, H. The chemistry of two-dimensional layered transition metal dichalcogenide nanosheets. *Nat. Chem.* **2013**, *5*, 263–275. [CrossRef] [PubMed]
128. Zeng, Z.; Yin, Z.; Huang, X.; Li, H.; He, Q.; Lu, G.; Boey, F.; Zhang, H. Single-Layer Semiconducting Nanosheets: High-yield preparation and device fabrication. *Angew. Chem.* **2011**, *123*, 11289–11293. [CrossRef]
129. Zong, X.; Xing, Z.; Yu, H.; Bai, Y.; Lu, G.Q.M.; Wang, L. Photocatalytic hydrogen production in a noble-metal-free system catalyzed by in situ grown molybdenum sulfide catalyst. *J. Catal.* **2014**, *310*, 51–56. [CrossRef]
130. Kang, Y.; Gong, Y.; Hu, Z.; Li, Z.; Qiu, Z.; Zhu, X.; Ajayan, P.M.; Fang, Z. Plasmonic hot electron enhanced MoS_2 photocatalysis in hydrogen evolution. *Nanoscale* **2015**, *7*, 4482–4488. [CrossRef]
131. Shi, J.; Ma, D.; Han, G.F.; Zhang, Y.; Ji, Q.; Gao, T.; Sun, J.; Song, X.; Li, C.; Zhang, Y.; et al. Controllable growth and transfer of monolayer MoS_2 on Au foils and its potential application in hydrogen evolution reaction. *ACS Nano* **2014**, *8*, 10196–10204. [CrossRef]
132. Yang, X.; Singh, D.; Xu, Z.; Ahuja, R. Sensing the polar molecules MH_3 (M = N, P, or As) with a Janus NbTeSe monolayer. *New J. Chem.* **2020**, *44*, 7932–7940. [CrossRef]
133. Luo, J.; Zhou, X.; Zhang, J.; Du, Z. Fabrication and characterization of Ag_2CO_3/SnS_2 composites with enhanced visible-light photocatalytic activity for the degradation of organic pollutants. *RSC Adv.* **2015**, *5*, 86705–86712. [CrossRef]
134. Yu, J.; Xu, C.Y.; Ma, F.X.; Hu, S.P.; Zhang, Y.W.; Zhen, L. Monodisperse SnS_2 nanosheets for high-performance photocatalytic hydrogen generation. *ACS Appl. Mater. Interfaces* **2014**, *6*, 22370–22377. [CrossRef] [PubMed]
135. Lin, C.; Zhu, X.; Feng, J.; Wu, C.; Hu, S.; Peng, J.; Guo, Y.; Peng, L.; Zhao, J.; Huang, J.; et al. Hydrogen-incorporated TiS_2 ultrathin nanosheets with ultrahigh conductivity for stamp-transferrable electrodes. *J. Am. Chem. Soc.* **2013**, *135*, 5144–5151.

136. Sang, Y.; Zhao, Z.; Zhao, M.; Hao, P.; Leng, Y.; Liu, H. From UV to near-infrared, WS_2 nanosheet: A novel photocatalyst for full solar light spectrum photodegradation. *Adv. Mater.* **2015**, *27*, 363–369. [PubMed]
137. Wu, Y.; Xu, M.; Chen, X.; Yang, S.; Wu, H.; Pan, J.; Xiong, X. CTAB-assisted synthesis of novel ultrathin $MoSe_2$ nanosheets perpendicular to graphene for the adsorption and photodegradation of organic dyes under visible light. *Nanoscale* **2016**, *8*, 440–450.
138. Li, H.; Wu, J.; Yin, Z.; Zhang, H. Preparation and applications of mechanically exfoliated single-layer and multilayer MoS_2 and WSe_2 nanosheets. *Accounts. Chem. Res.* **2014**, *47*, 1067–1075. [CrossRef]
139. Yang, X.; Singh, D.; Xu, Z.; Wang, Z.; Ahuja, R. An emerging Janus MoSeTe material for potential applications in optoelectronic devices. *J. Mater. Chem. C* **2019**, *7*, 12312–12320.
140. Liu, L.; Li, X.; Xu, L.C.; Liu, R.; Yang, Z. Effect of edge structure on the activity for hydrogen evolution reaction in MoS_2 nanoribbons. *Appl. Surf. Sci.* **2017**, *396*, 138–143.
141. Xie, J.; Zhang, H.; Li, S.; Wang, R.; Sun, X.; Zhou, M.; Zhou, J.; Lou, X.W.; Xie, Y. Defect-rich MoS_2 ultrathin nanosheets with additional active edge sites for enhanced electrocatalytic hydrogen evolution. *Adv. Mater.* **2013**, *25*, 5807–5813. [PubMed]
142. Zhang, X.H.; Li, N.; Wu, J.; Zheng, Y.Z.; Tao, X. Defect-rich O-incorporated 1T-MoS_2 nanosheets for remarkably enhanced visible-light photocatalytic H_2 evolution over CdS: The impact of enriched defects. *Appl. Catal. B Environ.* **2018**, *229*, 227–236.
143. Liu, G.; Li, Z.; Hasan, T.; Chen, X.; Zheng, W.; Feng, W.; Jia, D.; Zhou, Y.; Hu, P. Vertically aligned two-dimensional SnS_2 nanosheets with a strong photon capturing capability for efficient photoelectrochemical water splitting. *J. Mater. Chem. A* **2017**, *5*, 1989–1995.
144. Zhong, Y.; Zhao, G.; Ma, F.; Wu, Y.; Hao, X. Utilizing photocorrosion-recrystallization to prepare a highly stable and efficient CdS/WS_2 nanocomposite photocatalyst for hydrogen evolution. *Appl. Catal. B Environ.* **2016**, *199*, 466–472. [CrossRef]
145. Lv, X.; Wei, W.; Sun, Q.; Li, F.; Huang, B.; Dai, Y. Two-dimensional germanium monochalcogenides for photocatalytic water splitting with high carrier mobility. *Appl. Catal. B Environ.* **2017**, *217*, 275–284. [CrossRef]
146. Kong, S.; Jin, Z.; Liu, H.; Wang, Y. Morphological effect of graphene nanosheets on ultrathin CoS nanosheets and their applications for high-performance Li-ion batteries and photocatalysis. *J. Phys. Chem. C* **2014**, *118*, 25355–25364. [CrossRef]
147. Wu, R.; Xu, Y.; Xu, R.; Huang, Y.; Zhang, B. Ultrathin-nanosheet-based 3D hierarchical porous In_2S_3 microspheres: Chemical transformation synthesis, characterization, and enhanced photocatalytic and photoelectrochemical property. *J. Mater. Chem. A* **2015**, *3*, 1930–1934. [CrossRef]
148. Hao, Y.; Kang, S.Z.; Liu, X.; Li, X.; Qin, L.; Mu, J. An efficient noble-metal-free photocatalyst for visible-light-driven H_2 evolution: Cu/Ni-codoped $Cd_{0.5}Zn_{0.5}S$ nanoplates. *ACS Sustain. Chem. Eng.* **2017**, *5*, 1165–1172. [CrossRef]
149. Mahadik, M.A.; Shinde, P.S.; Cho, M.; Jang, J.S. Metal oxide top layer as an interfacial promoter on a $ZnIn_2S_4/TiO_2$ heterostructure photoanode for enhanced photoelectrochemical performance. *Appl. Catal. B Environ.* **2016**, *184*, 337–346. [CrossRef]
150. Chen, J.; Xin, F.; Yin, X.; Xiang, T.; Wang, Y. Synthesis of hexagonal and cubic $ZnIn_2S_4$ nanosheets for the photocatalytic reduction of CO_2 with methanol. *RSC Adv.* **2015**, *5*, 3833–3839. [CrossRef]
151. Lin, Z.; Ning, S.; Yang, Z.; Zhang, Z.; Huang, S.; Long, J.; Lin, H.; Wang, X. Large-scale preparation of heterometallic chalcogenide $MnSb_2S_4$ monolayer nanosheets with a high visible-light photocatalytic activity for H_2 evolution. *Chem. Commun.* **2016**, *52*, 13381–13384. [CrossRef]
152. Shen, S.; Li, L.; Wu, Z.; Sun, M.; Tang, Z.; Yang, J. In_4SnS_8 ultrathin nanosheets: A ternary sulfide with fast adsorption–visible-light photocatalysis dual function. *RSC Adv.* **2017**, *7*, 4555–4562. [CrossRef]
153. Zhong, J.; Wang, Q.; Chen, D.; Chen, L.; Yu, H.; Lu, H.; Ji, Z. Biomolecule-assisted solvothermal synthesis of 3D hierarchical Cu_2FeSnS_4 microspheres with enhanced photocatalytic activity. *Appl. Surf. Sci.* **2015**, *343*, 28–32. [CrossRef]
154. Sun, Y.; Cheng, H.; Gao, S.; Sun, Z.; Liu, Q.; Liu, Q.; Lei, F.; Yao, T.; He, J.; Wei, S.; et al. Freestanding tin disulfide single-layers realizing efficient visible-light water splitting. *Angew. Chem.* **2012**, *51*, 8727–8731. [CrossRef] [PubMed]
155. Peng, R.; Ma, Y.; Huang, B.; Dai, Y. Two-dimensional Janus PtSSe for photocatalytic water splitting under the visible or infrared light. *J. Mater. Chem. A* **2019**, *7*, 603–610. [CrossRef]

156. Zhuang, H.L.; Hennig, R.G. Single-layer group-III monochalcogenide photocatalysts for water splitting. *Chem. Mater.* **2013**, *25*, 3232–3238. [CrossRef]
157. Li, Y.; Li, Y.L.; Araujo, C.M.; Luo, W.; Ahuja, R. Single-layer MoS_2 as an efficient photocatalyst. *Catal. Sci. Technol.* **2013**, *3*, 2214–2220. [CrossRef]
158. Zhao, P.; Liang, Y.; Ma, Y.; Huang, B.; Dai, Y. Janus chromium dichalcogenide monolayers with low carrier recombination for photocatalytic overall water-splitting under infrared light. *J. Phys. Chem. C* **2019**, *123*, 4186–4192. [CrossRef]
159. Su, M.; Carter, S.; Sherwin, M.; Huntington, A.; Coldren, L. Voltage-controlled wavelength conversion by terahertz electro-optic modulation in double quantum wells. *Appl. Phys. Lett.* **2002**, *81*, 1564–1566. [CrossRef]
160. Sie, E.J.; McIver, J.W.; Lee, Y.H.; Fu, L.; Kong, J.; Gedik, N. Valley-selective optical Stark effect in monolayer WS_2. *Nat. Mater.* **2015**, *14*, 290–294. [CrossRef]
161. Peng, B.; Ang, P.K.; Loh, K.P. Two-dimensional dichalcogenides for light-harvesting applications. *Nano Today* **2015**, *10*, 128–137. [CrossRef]
162. Li, J.; Peng, Y.; Qian, X.; Lin, J. Few-layer Co-doped MoS_2 nanosheets with rich active sites as an efficient cocatalyst for photocatalytic H_2 production over CdS. *Appl. Surf. Sci.* **2018**, *452*, 437–442. [CrossRef]
163. Chen, J.; Wu, X.J.; Yin, L.; Li, B.; Hong, X.; Fan, Z.; Chen, B.; Xue, C.; Zhang, H. One-pot synthesis of CdS nanocrystals hybridized with single-layer transition-metal dichalcogenide nanosheets for efficient photocatalytic hydrogen evolution. *Angew. Chem.* **2015**, *127*, 1226–1230. [CrossRef]
164. Chava, R.K.; Do, J.Y.; Kang, M. Smart hybridization of Au coupled CdS nanorods with few layered MoS_2 nanosheets for high performance photocatalytic hydrogen evolution reaction. *ACS Sustain. Chem. Eng.* **2018**, *6*, 6445–6457. [CrossRef]
165. Ganesan, V.D.S.; Linghu, J.; Zhang, C.; Feng, Y.P.; Shen, L. Heterostructures of phosphorene and transition metal dichalcogenides for excitonic solar cells: A first-principles study. *Appl. Phys. Lett.* **2016**, *108*, 122105. [CrossRef]
166. Liao, J.; Sa, B.; Zhou, J.; Ahuja, R.; Sun, Z. Design of high-efficiency visible-light photocatalysts for water splitting: MoS_2/AlN (GaN) heterostructures. *J. Phys. Chem. C* **2014**, *118*, 17594–17599. [CrossRef]
167. Lu, A.Y.; Zhu, H.; Xiao, J.; Chuu, C.P.; Han, Y.; Chiu, M.H.; Cheng, C.C.; Yang, C.W.; Wei, K.H.; Yang, Y.; et al. Janus monolayers of transition metal dichalcogenides. *Nat. Nanotechnol.* **2017**, *12*, 744–749. [CrossRef] [PubMed]
168. Zhang, J.; Jia, S.; Kholmanov, I.; Dong, L.; Er, D.; Chen, W.; Guo, H.; Jin, Z.; Shenoy, V.B.; Shi, L.; et al. Janus monolayer transition-metal dichalcogenides. *ACS Nano* **2017**, *11*, 8192–8198. [PubMed]
169. Dong, L.; Lou, J.; Shenoy, V.B. Large in-plane and vertical piezoelectricity in Janus transition metal dichalchogenides. *ACS Nano* **2017**, *11*, 8242–8248. [CrossRef]
170. Ma, X.; Wu, X.; Wang, H.; Wang, Y. A Janus MoSSe monolayer: A potential wide solar-spectrum water-splitting photocatalyst with a low carrier recombination rate. *J. Mater. Chem. A* **2018**, *6*, 2295–2301. [CrossRef]
171. Er, D.; Ye, H.; Frey, N.C.; Kumar, H.; Lou, J.; Shenoy, V.B. Prediction of enhanced catalytic activity for hydrogen evolution reaction in Janus transition metal dichalcogenides. *Nano Lett.* **2018**, *18*, 3943–3949. [CrossRef]
172. Ji, Y.; Yang, M.; Lin, H.; Hou, T.; Wang, L.; Li, Y.; Lee, S.T. Janus structures of transition metal dichalcogenides as the heterojunction photocatalysts for water splitting. *J. Phys. Chem. C* **2018**, *122*, 3123–3129.
173. Chen, W.; Hou, X.; Shi, X.; Pan, H. Two-dimensional janus transition metal oxides and chalcogenides: multifunctional properties for photocatalysts, electronics, and energy conversion. *ACS Appl. Mater. Interfaces* **2018**, *10*, 35289–35295. [CrossRef]
174. Yang, X.Y.; Hussain, T.; Wärnå, J.P.A.; Xu, Z.; Ahuja, R. Exploring Janus MoSSe monolayer as a workable media for SOF_6 decompositions sensing based on DFT calculations. *Comp. Mater. Sci.* **2021**, *186*, 109976. [CrossRef]
175. Ran, J.; Gao, G.; Li, F.T.; Ma, T.Y.; Du, A.; Qiao, S.Z. Ti_3C_2 MXene co-catalyst on metal sulfide photo-absorbers for enhanced visible-light photocatalytic hydrogen production. *Nat. Commun.* **2017**, *8*, 1–10. [CrossRef] [PubMed]
176. Guo, Z.; Zhou, J.; Zhu, L.; Sun, Z. MXene: A promising photocatalyst for water splitting. *J. Mater. Chem. A* **2016**, *4*, 11446–11452. [CrossRef]

177. Yang, X.Y.; Luo, W.; Ahuja, R. Fluoride ion batteries: Designing flexible M_2CH_2 (M = Ti or V) MXenes as high-capacity cathode materials. *Nano Energy* **2020**, *74*, 104911. [CrossRef]
178. Naguib, M.; Mochalin, V.N.; Barsoum, M.W.; Gogotsi, Y. 25th anniversary article: MXenes: A new family of two-dimensional materials. *Adv. Mater.* **2014**, *26*, 992–1005. [CrossRef] [PubMed]
179. Urbankowski, P.; Anasori, B.; Makaryan, T.; Er, D.; Kota, S.; Walsh, P.L.; Zhao, M.; Shenoy, V.B.; Barsoum, M.W.; Gogotsi, Y. Synthesis of two-dimensional titanium nitride Ti_4N_3 (MXene). *Nanoscale* **2016**, *8*, 11385–11391. [CrossRef]
180. Dhakal, C.; Aryal, S.; Sakidja, R.; Ching, W.Y. Approximate lattice thermal conductivity of MAX phases at high temperature. *J. Eur. Ceram. Soc.* **2015**, *35*, 3203–3212. [CrossRef]
181. Barsoum, M.W. *MAX Phases: Properties of Machinable Ternary Carbides and Nitrides*; John Wiley & Sons: Hoboken, NJ, USA, 2013.
182. Anasori, B.; Xie, Y.; Beidaghi, M.; Lu, J.; Hosler, B.C.; Hultman, L.; Kent, P.R.; Gogotsi, Y.; Barsoum, M.W. Two-dimensional, ordered, double transition metals carbides (MXenes). *ACS Nano* **2015**, *9*, 9507–9516. [CrossRef]
183. Luo, J.; Zhang, W.; Yuan, H.; Jin, C.; Zhang, L.; Huang, H.; Liang, C.; Xia, Y.; Zhang, J.; Gan, Y.; et al. Pillared structure design of MXene with ultralarge interlayer spacing for high-performance lithium-ion capacitors. *Acs Nano* **2017**, *11*, 2459–2469. [CrossRef]
184. Li, Y.; Deng, X.; Tian, J.; Liang, Z.; Cui, H. Ti_3C_2 MXene-derived Ti_3C_2/TiO_2 nanoflowers for noble-metal-free photocatalytic overall water splitting. *Appl. Mater. Today.* **2018**, *13*, 217–227. [CrossRef]
185. Wu, X.; Wang, Z.; Yu, M.; Xiu, L.; Qiu, J. Stabilizing the MXenes by carbon nanoplating for developing hierarchical nanohybrids with efficient lithium storage and hydrogen evolution capability. *Adv. Mater.* **2017**, *29*, 1607017. [CrossRef] [PubMed]
186. Urbankowski, P.; Anasori, B.; Hantanasirisakul, K.; Yang, L.; Zhang, L.; Haines, B.; May, S.J.; Billinge, S.J.; Gogotsi, Y. 2D molybdenum and vanadium nitrides synthesized by ammoniation of 2D transition metal carbides (MXenes). *Nanoscale* **2017**, *9*, 17722–17730. [CrossRef] [PubMed]
187. Wang, H.; Peng, R.; Hood, Z.D.; Naguib, M.; Adhikari, S.P.; Wu, Z. Titania Composites with 2 D Transition Metal Carbides as Photocatalysts for Hydrogen Production under Visible-Light Irradiation. *ChemSusChem* **2016**, *9*, 1490–1497. [CrossRef] [PubMed]
188. Su, T.; Peng, R.; Hood, Z.D.; Naguib, M.; Ivanov, I.N.; Keum, J.K.; Qin, Z.; Guo, Z.; Wu, Z. One-step synthesis of $Nb_2O_5/C/Nb_2C$ (MXene) composites and their use as photocatalysts for hydrogen evolution. *ChemSusChem* **2018**, *11*, 688–699. [CrossRef]
189. Sun, Y.; Jin, D.; Sun, Y.; Meng, X.; Gao, Y.; Dall'Agnese, Y.; Chen, G.; Wang, X.F. g-$C_3N_4/Ti_3C_2T_x$ (MXenes) composite with oxidized surface groups for efficient photocatalytic hydrogen evolution. *J. Mater. Chem. A* **2018**, *6*, 9124–9131. [CrossRef]
190. Shao, M.; Shao, Y.; Chai, J.; Qu, Y.; Yang, M.; Wang, Z.; Yang, M.; Ip, W.F.; Kwok, C.T.; Shi, X.; et al. Synergistic effect of 2D Ti_2C and g-C_3N_4 for efficient photocatalytic hydrogen production. *J. Mater. Chem. A* **2017**, *5*, 16748–16756. [CrossRef]
191. Pandey, M.; Thygesen, K.S. Two-dimensional MXenes as catalysts for electrochemical hydrogen evolution: A computational screening study. *J. Phys. Chem. C* **2017**, *121*, 13593–13598. [CrossRef]
192. Li, S.; Tuo, P.; Xie, J.; Zhang, X.; Xu, J.; Bao, J.; Pan, B.; Xie, Y. Ultrathin MXene nanosheets with rich fluorine termination groups realizing efficient electrocatalytic hydrogen evolution. *Nano Energy* **2018**, *47*, 512–518. [CrossRef]
193. Zheng, Y.; Liu, J.; Liang, J.; Jaroniec, M.; Qiao, S.Z. Graphitic carbon nitride materials: Controllable synthesis and applications in fuel cells and photocatalysis. *Energy Environ. Sci.* **2012**, *5*, 6717–6731. [CrossRef]
194. Thomas, A.; Fischer, A.; Goettmann, F.; Antonietti, M.; Müller, J.O.; Schlögl, R.; Carlsson, J.M. Graphitic carbon nitride materials: Variation of structure and morphology and their use as metal-free catalysts. *J. Mater. Chem.* **2008**, *18*, 4893–4908. [CrossRef]
195. Di, J.; Xia, J.; Li, X.; Ji, M.; Xu, H.; Chen, Z.; Li, H. Constructing confined surface carbon defects in ultrathin graphitic carbon nitride for photocatalytic free radical manipulation. *Carbon* **2016**, *107*, 1–10.
196. Xing, W.; Tu, W.; Han, Z.; Hu, Y.; Meng, Q.; Chen, G. Template-induced high-crystalline g-C_3N_4 nanosheets for enhanced photocatalytic H_2 evolution. *ACS Energy Lett.* **2018**, *3*, 514–519.
197. Ryu, J.; Jang, Y.J.; Choi, S.; Kang, H.J.; Park, H.; Lee, J.S.; Park, S. All-in-one synthesis of mesoporous silicon nanosheets from natural clay and their applicability to hydrogen evolution. *NPG Asia Mater.* **2016**, *8*, e248.

198. Niu, P.; Zhang, L.; Liu, G.; Cheng, H.M. Graphene-like carbon nitride nanosheets for improved photocatalytic activities. *Adv. Funct. Mater.* **2012**, *22*, 4763–4770.
199. Do, H.Q.; Chandrashekar, E.; Fu, G.C. Nickel/bis (oxazoline)-catalyzed asymmetric Negishi arylations of racemic secondary benzylic electrophiles to generate enantioenriched 1, 1-diarylalkanes. *J. Am. Chem. Soc.* **2013**, *135*, 16288–16291. [PubMed]
200. Yang, S.; Gong, Y.; Zhang, J.; Zhan, L.; Ma, L.; Fang, Z.; Vajtai, R.; Wang, X.; Ajayan, P.M. Exfoliated graphitic carbon nitride nanosheets as efficient catalysts for hydrogen evolution under visible light. *Adv. Mater.* **2013**, *25*, 2452–2456.
201. Lin, Q.; Li, L.; Liang, S.; Liu, M.; Bi, J.; Wu, L. Efficient synthesis of monolayer carbon nitride 2D nanosheet with tunable concentration and enhanced visible-light photocatalytic activities. *Appl. Catal. B Environ.* **2015**, *163*, 135–142.
202. Ou, H.; Lin, L.; Zheng, Y.; Yang, P.; Fang, Y.; Wang, X. Tri-s-triazine-based crystalline carbon nitride nanosheets for an improved hydrogen evolution. *Adv. Mater.* **2017**, *29*, 1700008.
203. She, X.; Wu, J.; Zhong, J.; Xu, H.; Yang, Y.; Vajtai, R.; Lou, J.; Liu, Y.; Du, D.; Li, H.; et al. Oxygenated monolayer carbon nitride for excellent photocatalytic hydrogen evolution and external quantum efficiency. *Nano Energy* **2016**, *27*, 138–146.
204. Zhao, Q.; Fu, L.; Jiang, D.; Xi, Y.; Yang, H. A nanoclay-induced defective g-C_3N_4 photocatalyst for highly efficient catalytic reactions. *Chem. Commun.* **2018**, *54*, 8249–8252.
205. Zhang, J.; Zhang, M.; Yang, C.; Wang, X. Nanospherical carbon nitride frameworks with sharp edges accelerating charge collection and separation at a soft photocatalytic interface. *Nat. Rev. Mater.* **2014**, *26*, 4121–4126. [CrossRef] [PubMed]
206. Xia, P.; Zhu, B.; Yu, J.; Cao, S.; Jaroniec, M. Ultra-thin nanosheet assemblies of graphitic carbon nitride for enhanced photocatalytic CO_2 reduction. *J. Mater. Chem. A* **2017**, *5*, 3230–3238. [CrossRef]
207. Zhang, Z.; Zhang, Y.; Lu, L.; Si, Y.; Zhang, S.; Chen, Y.; Dai, K.; Duan, P.; Duan, L.; Liu, J. Graphitic carbon nitride nanosheet for photocatalytic hydrogen production: The impact of morphology and element composition. *Appl. Surf. Sci.* **2017**, *391*, 369–375. [CrossRef]
208. Kang, Y.; Yang, Y.; Yin, L.C.; Kang, X.; Liu, G.; Cheng, H.M. An amorphous carbon nitride photocatalyst with greatly extended visible-light-responsive range for photocatalytic hydrogen generation. *Adv. Mater.* **2015**, *27*, 4572–4577. [CrossRef] [PubMed]
209. Schwinghammer, K.; Mesch, M.B.; Duppel, V.; Ziegler, C.; Senker, J.; Lotsch, B.V. Crystalline carbon nitride nanosheets for improved visible-light hydrogen evolution. *J. Am. Chem. Soc.* **2014**, *136*, 1730–1733. [CrossRef]
210. Tu, W.; Xu, Y.; Wang, J.; Zhang, B.; Zhou, T.; Yin, S.; Wu, S.; Li, C.; Huang, Y.; Zhou, Y.; et al. Investigating the role of tunable nitrogen vacancies in graphitic carbon nitride nanosheets for efficient visible-light-driven H_2 evolution and CO_2 reduction. *ACS Sustain. Chem. Eng.* **2017**, *5*, 7260–7268. [CrossRef]
211. Liang, Q.; Li, Z.; Huang, Z.H.; Kang, F.; Yang, Q.H. Holey graphitic carbon nitride nanosheets with carbon vacancies for highly improved photocatalytic hydrogen production. *Adv. Funct. Mater.* **2015**, *25*, 6885–6892. [CrossRef]
212. Tonda, S.; Kumar, S.; Kandula, S.; Shanker, V. Fe-doped and-mediated graphitic carbon nitride nanosheets for enhanced photocatalytic performance under natural sunlight. *J. Mater. Chem. A* **2014**, *2*, 6772–6780. [CrossRef]
213. Zhu, Y.P.; Ren, T.Z.; Yuan, Z.Y. Mesoporous phosphorus-doped g-C_3N_4 nanostructured flowers with superior photocatalytic hydrogen evolution performance. *ACS Appl. Mater. Interfaces* **2015**, *7*, 16850–16856. [CrossRef]
214. Rahman, M.Z.; Ran, J.; Tang, Y.; Jaroniec, M.; Qiao, S.Z. Surface activated carbon nitride nanosheets with optimized electro-optical properties for highly efficient photocatalytic hydrogen production. *J. Mater. Chem. A* **2016**, *4*, 2445–2452. [CrossRef]
215. Teng, Z.; Lv, H.; Wang, C.; Xue, H.; Pang, H.; Wang, G. Bandgap engineering of ultrathin graphene-like carbon nitride nanosheets with controllable oxygenous functionalization. *Carbon* **2017**, *113*, 63–75. [CrossRef]
216. Niu, P.; Yin, L.C.; Yang, Y.Q.; Liu, G.; Cheng, H.M. Increasing the visible light absorption of graphitic carbon nitride (Melon) photocatalysts by homogeneous self-modification with nitrogen vacancies. *Adv. Mater.* **2014**, *26*, 8046–8052. [CrossRef]
217. Sun, H.; Zhou, G.; Wang, Y.; Suvorova, A.; Wang, S. A new metal-free carbon hybrid for enhanced photocatalysis. *ACS Appl. Mater. Interfaces* **2014**, *6*, 16745–16754. [CrossRef] [PubMed]

218. Chen, J.; Zhao, D.; Diao, Z.; Wang, M.; Guo, L.; Shen, S. Bifunctional modification of graphitic carbon nitride with $MgFe_2O_4$ for enhanced photocatalytic hydrogen generation. *ACS Appl. Mater. Interfaces* **2015**, *7*, 18843–18848. [CrossRef] [PubMed]
219. Zhao, W.; Wei, Z.; He, H.; Xu, J.; Li, J.; Yang, S.; Sun, C. Supporting 1-D $AgVO_3$ nanoribbons on single layer 2-D graphitic carbon nitride ultrathin nanosheets and their excellent photocatalytic activities. *Appl. Catal. A Gen.* **2015**, *501*, 74–82. [CrossRef]
220. Wang, Z.; Lv, J.; Zhang, J.; Dai, K.; Liang, C. Facile synthesis of Z-scheme $BiVO_4$/porous graphite carbon nitride heterojunction for enhanced visible-light-driven photocatalyst. *Appl. Surf. Sci.* **2018**, *430*, 595–602.
221. Deng, Y.; Tang, L.; Zeng, G.; Wang, J.; Zhou, Y.; Wang, J.; Tang, J.; Wang, L.; Feng, C. Facile fabrication of mediator-free Z-scheme photocatalyst of phosphorous-doped ultrathin graphitic carbon nitride nanosheets and bismuth vanadate composites with enhanced tetracycline degradation under visible light. *J. Colloid. Interf. Sci.* **2018**, *509*, 219–234. [CrossRef] [PubMed]
222. Zhao, H.; Sun, S.; Wu, Y.; Jiang, P.; Dong, Y.; Xu, Z.J. Ternary graphitic carbon nitride/red phosphorus/molybdenum disulfide heterostructure: An efficient and low cost photocatalyst for visible-light-driven H_2 evolution from water. *Carbon* **2017**, *119*, 56–61. [CrossRef]
223. Lu, Y.; Chu, D.; Zhu, M.; Du, Y.; Yang, P. Exfoliated carbon nitride nanosheets decorated with NiS as an efficient noble-metal-free visible-light-driven photocatalyst for hydrogen evolution. *Phys. Chem. Chem. Phys.* **2015**, *17*, 17355–17361. [CrossRef]
224. Zhang, G.; Zang, S.; Wang, X. Layered $Co(OH)_2$ deposited polymeric carbon nitrides for photocatalytic water oxidation. *ACS Catal.* **2015**, *5*, 941–947. [CrossRef]
225. Le, S.; Jiang, T.; Li, Y.; Zhao, Q.; Li, Y.; Fang, W.; Gong, M. Highly efficient visible-light-driven mesoporous graphitic carbon nitride/ZnO nanocomposite photocatalysts. *Appl. Catal. B Environ.* **2017**, *200*, 601–610. [CrossRef]
226. Tian, J.; Ning, R.; Liu, Q.; Asiri, A.M.; Al-Youbi, A.O.; Sun, X. Three-dimensional porous supramolecular architecture from ultrathin *g*-C_3N_4 nanosheets and reduced graphene oxide: Solution self-assembly construction and application as a highly efficient metal-free electrocatalyst for oxygen reduction reaction. *ACS Appl. Mater. Interfaces* **2014**, *6*, 1011–1017. [CrossRef] [PubMed]
227. Akhundi, A.; Habibi-Yangjeh, A. Graphitic carbon nitride nanosheets decorated with $CuCr_2O_4$ nanoparticles: Novel photocatalysts with high performances in visible light degradation of water pollutants. *J. Colloid. Interf. Sci.* **2017**, *504*, 697–710. [CrossRef] [PubMed]
228. Sridharan, K.; Jang, E.; Park, J.H.; Kim, J.H.; Lee, J.H.; Park, T.J. Silver Quantum Cluster (Ag9)-Grafted Graphitic Carbon Nitride Nanosheets for Photocatalytic Hydrogen Generation and Dye Degradation. *Chem. Eur. J.* **2015**, *21*, 9126–9132. [CrossRef] [PubMed]
229. Wu, X.; Lu, C.; Liu, J.; Song, S.; Sun, C. Constructing efficient solar light photocatalytic system with Ag-introduced carbon nitride for organic pollutant elimination. *Appl. Catal. B Environ.* **2017**, *217*, 232–240. [CrossRef]
230. Liang, D.; Jing, T.; Ma, Y.; Hao, J.; Sun, G.; Deng, M. Photocatalytic properties of *g*-C_6N_6/*g*-C_3N_4 heterostructure: A theoretical study. *J. Phys. Chem. C* **2016**, *120*, 24023–24029. [CrossRef]
231. Zhang, X.; Chen, A.; Zhang, Z.; Jiao, M.; Zhou, Z. Rational design of C_2N-based type-II heterojunctions for overall photocatalytic water splitting. *Nanoscale Adv.* **2019**, *1*, 154–161. [CrossRef]
232. Geick, R.; Perry, C.; Rupprecht, G. Normal modes in hexagonal boron nitride. *Phys. Rev.* **1966**, *146*, 543. [CrossRef]
233. Liu, L.; Feng, Y.; Shen, Z. Structural and electronic properties of h-BN. *Phys. Rev. B* **2003**, *68*, 104102. [CrossRef]
234. Wang, G.; Zhi, Y.; Bo, M.; Xiao, S.; Li, Y.; Zhao, W.; Li, Y.; Li, Y.; He, Z. 2D Hexagonal Boron Nitride/Cadmium Sulfide Heterostructure as a Promising Water-Splitting Photocatalyst. *Phys. Status Solidi B* **2020**, *257*, 1900431. [CrossRef]
235. Ci, L.; Song, L.; Jin, C.; Jariwala, D.; Wu, D.; Li, Y.; Srivastava, A.; Wang, Z.; Storr, K.; Balicas, L.; et al. Atomic layers of hybridized boron nitride and graphene domains. *Nat. Mater.* **2010**, *9*, 430–435. [CrossRef] [PubMed]
236. Lu, J.; Zhang, K.; Liu, X.F.; Zhang, H.; Sum, T.C.; Neto, A.H.C.; Loh, K.P. Order–disorder transition in a two-dimensional boron–carbon–nitride alloy. *Nat. Commun.* **2013**, *4*, 1–7. [CrossRef] [PubMed]
237. Huang, C.; Chen, C.; Zhang, M.; Lin, L.; Ye, X.; Lin, S.; Antonietti, M.; Wang, X. Carbon-doped BN nanosheets for metal-free photoredox catalysis. *Nat. Commun.* **2015**, *6*, 7698. [CrossRef] [PubMed]

238. Abdelsalam, H.; Younis, W.; Saroka, V.; Teleb, N.; Yunoki, S.; Zhang, Q. Interaction of hydrated metals with chemically modified hexagonal boron nitride quantum dots: Wastewater treatment and water splitting. *Phys. Chem. Chem. Phys.* **2020**, *22*, 2566–2579. [CrossRef] [PubMed]
239. Li, X.; Zhao, J.; Yang, J. Semihydrogenated BN sheet: A promising visible-light driven photocatalyst for water splitting. *Sci. Rep.* **2013**, *3*, 1858. [CrossRef] [PubMed]
240. Zhang, J.; Zhang, B.; Yu, Y.; Wang, C.M. First-principles insights of electronic and optical properties of F-doped hexagonal boron nitride nanosheets for photo-catalytic water splitting. *EPL Europhys. Lett.* **2019**, *127*, 67003. [CrossRef]
241. Guha, A.; Veettil Vineesh, T.; Sekar, A.; Narayanaru, S.; Sahoo, M.; Nayak, S.; Chakraborty, S.; Narayanan, T.N. Mechanistic insight into enhanced hydrogen evolution reaction activity of ultrathin hexagonal boron nitride-modified Pt electrodes. *ACS Catal.* **2018**, *8*, 6636–6644. [CrossRef]
242. Kaewmaraya, T.; Ngamwongwan, L.; Moontragoon, P.; Jarernboon, W.; Singh, D.; Ahuja, R.; Karto, A.; Hussain, T. Novel green phosphorene as a superior chemical gas sensing material. *J. Hazard. Mater.* **2020**, *401*, 123340. [CrossRef]
243. Brown, A.; Rundqvist, S. Refinement of the crystal structure of black phosphorus. *Acta Crystallogr.* **1965**, *19*, 684–685. [CrossRef]
244. Zhang, X.; Xie, H.; Liu, Z.; Tan, C.; Luo, Z.; Li, H.; Lin, J.; Sun, L.; Chen, W.; Xu, Z.; et al. Black phosphorus quantum dots. *Angew. Chem.* **2015**, *54*, 3653–3657. [CrossRef]
245. Castellanos-Gomez, A.; Vicarelli, L.; Prada, E.; Island, J.O.; Narasimha-Acharya, K.; Blanter, S.I.; Groenendijk, D.J.; Buscema, M.; Steele, G.A.; et al. Isolation and characterization of few-layer black phosphorus. *2D Mater.* **2014**, *1*, 025001. [CrossRef]
246. Liu, H.; Du, Y.; Deng, Y.; Peide, D.Y. Semiconducting black phosphorus: Synthesis, transport properties and electronic applications. *Chem. Soc. Rev.* **2015**, *44*, 2732–2743. [CrossRef] [PubMed]
247. Chhowalla, M.; Jena, D.; Zhang, H. Two-dimensional semiconductors for transistors. *Nat. Rev. Mater.* **2016**, *1*, 1–15. [CrossRef]
248. Li, L.; Yu, Y.; Ye, G.J.; Ge, Q.; Ou, X.; Wu, H.; Feng, D.; Chen, X.H.; Zhang, Y. Black phosphorus field-effect transistors. *Nat. Nanotechnol.* **2014**, *9*, 372. [CrossRef]
249. Hu, J.; Guo, Z.; Mcwilliams, P.E.; Darges, J.E.; Druffel, D.L.; Moran, A.M.; Warren, S.C. Band gap engineering in a 2D material for solar-to-chemical energy conversion. *Nano Lett.* **2016**, *16*, 74–79. [CrossRef]
250. Sa, B.; Li, Y.L.; Qi, J.; Ahuja, R.; Sun, Z. Strain engineering for phosphorene: The potential application as a photocatalyst. *J. Phys. Chem. C* **2014**, *118*, 26560–26568. [CrossRef]
251. Lee, H.U.; Lee, S.C.; Won, J.; Son, B.C.; Choi, S.; Kim, Y.; Park, S.Y.; Kim, H.S.; Lee, Y.C.; Lee, J. Stable semiconductor black phosphorus (BP) @ titanium dioxide (TiO_2) hybrid photocatalysts. *Sci. Rep.* **2015**, *5*, 8691. [CrossRef]
252. Rudenko, A.N.; Katsnelson, M.I. Quasiparticle band structure and tight-binding model for single-and bilayer black phosphorus. *Phys. Rev. B* **2014**, *89*, 201408. [CrossRef]
253. Wang, H.; Yang, X.; Shao, W.; Chen, S.; Xie, J.; Zhang, X.; Wang, J.; Xie, Y. Ultrathin black phosphorus nanosheets for efficient singlet oxygen generation. *J. Am. Chem. Soc.* **2015**, *137*, 11376–11382. [CrossRef]
254. Zhu, M.; Kim, S.; Mao, L.; Fujitsuka, M.; Zhang, J.; Wang, X.; Majima, T. Metal-free photocatalyst for H_2 evolution in visible to near-infrared region: Black phosphorus/graphitic carbon nitride. *J. Am. Chem. Soc.* **2017**, *139*, 13234–13242. [CrossRef]
255. Shukla, V.; Grigoriev, A.; Ahuja, R. Rectifying behavior in twisted bilayer black phosphorus nanojunctions mediated through intrinsic anisotropy. *Nanoscale Adv.* **2020**, *2*, 1493–1501.
256. Férey, G. Hybrid Porous Solids: Past, Present, Future. *Chem. Soc. Rev.* **2008**, *37*, 191–214. [PubMed]
257. James, S.L. Metal-organic frameworks. *Chem. Soc. Rev.* **2003**, *32*, 276–288. [PubMed]
258. Silva, C.G.; Luz, I.; i Xamena, F.X.L.; Corma, A.; García, H. Water stable Zr–benzenedicarboxylate metal–organic frameworks as photocatalysts for hydrogen generation. *Chem. Eur. J.* **2010**, *16*, 11133–11138.
259. Horiuchi, Y.; Toyao, T.; Saito, M.; Mochizuki, K.; Iwata, M.; Higashimura, H.; Anpo, M.; Matsuoka, M. Visible-light-promoted photocatalytic hydrogen production by using an amino-functionalized Ti (IV) metal–organic framework. *J. Phys. Chem. C* **2012**, *116*, 20848–20853.
260. Gao, H.; Zhen, W.; Ma, J.; Lu, G. High efficient solar hydrogen generation by modulation of Co-Ni sulfide (220) surface structure and adjusting adsorption hydrogen energy. *Appl. Catal. B Environ.* **2017**, *206*, 353–363. [CrossRef]

261. Cavka, J.H.; Jakobsen, S.; Olsbye, U.; Guillou, N.; Lamberti, C.; Bordiga, S.; Lillerud, K.P. A new zirconium inorganic building brick forming metal organic frameworks with exceptional stability. *J. Am. Chem. Soc.* **2008**, *130*, 13850–13851. [CrossRef]
262. Feng, X.; Ding, X.; Jiang, D. Covalent organic frameworks. *Chem. Soc. Rev.* **2012**, *41*, 6010–6022.
263. Ding, S.Y.; Wang, W. Covalent organic frameworks (COFs): From design to applications. *Chem. Soc. Rev.* **2013**, *42*, 548–568.
264. Vyas, V.S.; Haase, F.; Stegbauer, L.; Savasci, G.; Podjaski, F.; Ochsenfeld, C.; Lotsch, B.V. A tunable azine covalent organic framework platform for visible light-induced hydrogen generation. *Nat. Commun.* **2015**, *6*, 1–9.
265. Huang, N.; Wang, P.; Jiang, D. Covalent organic frameworks: A materials platform for structural and functional designs. *Nat. Rev. Mater.* **2016**, *1*, 1–19. [CrossRef]
266. Smith, B.J.; Hwang, N.; Chavez, A.D.; Novotney, J.L.; Dichtel, W.R. Growth rates and water stability of 2D boronate ester covalent organic frameworks. *Chem. Commun.* **2015**, *51*, 7532–7535. [CrossRef]
267. Spitler, E.L.; Koo, B.T.; Novotney, J.L.; Colson, J.W.; Uribe-Romo, F.J.; Gutierrez, G.D.; Clancy, P.; Dichtel, W.R. A 2D covalent organic framework with 4.7-nm pores and insight into its interlayer stacking. *J. Am. Chem. Soc.* **2011**, *133*, 19416–19421. [CrossRef] [PubMed]
268. Ghosh, S.; Kouamé, N.A.; Ramos, L.; Remita, S.; Dazzi, A.; Deniset-Besseau, A.; Beaunier, P.; Goubard, F.; Aubert, P.H.; Remita, H. Conducting polymer nanostructures for photocatalysis under visible light. *Nat. Mater.* **2015**, *14*, 505–511. [CrossRef] [PubMed]
269. Pachfule, P.; Acharjya, A.; Roeser, J.; Langenhahn, T.; Schwarze, M.; Schomäcker, R.; Thomas, A.; Schmidt, J. Diacetylene functionalized covalent organic framework (COF) for photocatalytic hydrogen generation. *J. Am. Chem. Soc.* **2018**, *140*, 1423–1427. [CrossRef] [PubMed]
270. Jin, E.; Lan, Z.; Jiang, Q.; Geng, K.; Li, G.; Wang, X.; Jiang, D. 2D sp^2 carbon-conjugated covalent organic frameworks for photocatalytic hydrogen production from water. *Chem* **2019**, *5*, 1632–1647. [CrossRef]
271. López-Magano, A.; Platero-Prats, A.E.; Cabrera, S.; Mas-Ballesté, R.; Alemán, J. Incorporation of photocatalytic Pt (II) complexes into imine-based layered covalent organic frameworks (COFs) through monomer truncation strategy. *Appl. Catal. B Environ.* **2020**, *272*, 119027. [CrossRef]
272. Grabowska, E. Selected perovskite oxides: Characterization, preparation and photocatalytic properties—A review. *Appl. Catal. B Environ.* **2016**, *186*, 97–126. [CrossRef]
273. Kanhere, P.; Chen, Z. A review on visible light active perovskite-based photocatalysts. *Molecules* **2014**, *19*, 19995–20022. [CrossRef]
274. Zhang, G.; Liu, G.; Wang, L.; Irvine, J.T. Inorganic perovskite photocatalysts for solar energy utilization. *Chem. Soc. Rev.* **2016**, *45*, 5951–5984. [CrossRef]
275. Henriques, J.; Caetano, E.; Freire, V.; Da Costa, J.; Albuquerque, E. Structural, electronic, and optical absorption properties of orthorhombic $CaSnO_3$ through ab initio calculations. *J. Phys. Cond. Matter* **2007**, *19*, 106214. [CrossRef]
276. Park, S.; Song, H.J.; Lee, C.W.; Hwang, S.W.; Cho, I.S. Enhanced photocatalytic activity of ultrathin Ba5Nb4O15 two-dimensional nanosheets. *ACS Appl. Mater. Interfaces* **2015**, *7*, 21860–21867. [CrossRef]
277. Wang, C.; Chesman, A.S.; Jasieniak, J.J. Stabilizing the cubic perovskite phase of $CsPbI_3$ nanocrystals by using an alkyl phosphinic acid. *Chem. Commun.* **2017**, *53*, 232–235. [CrossRef] [PubMed]
278. Zhu, Y.; Dai, Y.; Lai, K.; Li, Z.; Huang, B. Optical transition and photocatalytic performance of d1 metallic perovskites. *J. Phys. Chem. C* **2013**, *117*, 5593–5598. [CrossRef]
279. Khan, M.S.; Diao, Z.; Osada, M.; Shen, S. Nitrogen doped ultrathin calcium/sodium niobate perovskite nanosheets for photocatalytic water oxidation. *Sol. Energy Mater. Sol. C* **2020**, *205*, 110283. [CrossRef]
280. Cheng, Z.; Lin, J. Layered organic–inorganic hybrid perovskites: Structure, optical properties, film preparation, patterning and templating engineering. *CrystEngComm* **2010**, *12*, 2646–2662. [CrossRef]
281. Cui, W.; Liu, L.; Feng, L.; Xu, C.; Li, Z.; Lü, S.; Qiu, F. Preparation of $Pt/K_2La_2Ti_3O_{10}$ and its photo-catalytic activity for hydrogen evolution from methanol water solution. *Sci. China Ser. B* **2006**, *49*, 162–168. [CrossRef]
282. Rodionov, I.A.; Sokolova, I.P.; Silyukov, O.I.; Burovikhina, A.A.; Fateev, S.A.; Zvereva, I.A. Protonation and photocatalytic activity of the $Rb_2La_2Ti_3O_{10}$ layered oxide in the reaction of hydrogen production. *Int. J. Photoenergy* **2017**, *2017*, 9628146. [CrossRef]
283. Chen, W.; Chen, X.; Yang, Y.; Yuan, J.; Shangguan, W. Synthesis and performance of layered perovskite-type $H\text{-}ABi_2Ta_2O_9$ (A = Ca, Sr, Ba, $K_{0.5}La_{0.5}$) for photocatalytic water splitting. *Int. J. Hydrogen Energy* **2014**, *39*, 13468–13473. [CrossRef]

284. Li, Y.; Chen, G.; Zhang, H.; Lv, Z. Band structure and photocatalytic activities for H_2 production of $ABi_2Nb_2O_9$ (A = Ca, Sr, Ba). *Int. J. Hydrogen Energy* **2010**, *35*, 2652–2656. [CrossRef]
285. Ebina, Y.; Akatsuka, K.; Fukuda, K.; Sasaki, T. Synthesis and in situ *x*-ray diffraction characterization of two-dimensional perovskite-type oxide colloids with a controlled molecular thickness. *Chem. Mater.* **2012**, *24*, 4201–4208. [CrossRef]
286. Zhang, L.; Hu, C.; Cheng, L.; Ding, W.; Hou, W.; Chen, J. S-doped $HTiNbO_5$ nanosheets: A novel efficient visible-light photocatalyst. *Chin. J. Catal.* **2013**, *34*, 2089–2097. [CrossRef]
287. Compton, O.C.; Carroll, E.C.; Kim, J.Y.; Larsen, D.S.; Osterloh, F.E. Calcium niobate semiconductor nanosheets as catalysts for photochemical hydrogen evolution from water. *J. Phys. Chem. C* **2007**, *111*, 14589–14592. [CrossRef]
288. Stolarczyk, J.K.; Bhattacharyya, S.; Polavarapu, L.; Feldmann, J. Challenges and prospects in solar water splitting and CO_2 reduction with inorganic and hybrid nanostructures. *ACS Catal.* **2018**, *8*, 3602–3635. [CrossRef]
289. Arandiyan, H.; Wang, Y.; Sun, H.; Rezaei, M.; Dai, H. Ordered meso-and macroporous perovskite oxide catalysts for emerging applications. *Chem. Commun.* **2018**, *54*, 6484–6502. [CrossRef]
290. Reddy, V.R.; Hwang, D.W.; Lee, J.S. Effect of Zr substitution for Ti in $KLaTiO_4$ for photocatalytic water splitting. *Catal. Lett.* **2003**, *90*, 39–43. [CrossRef]
291. Sun, X.; Mi, Y.; Jiao, F.; Xu, X. Activating layered perovskite compound Sr_2TiO_4 via La/N codoping for visible light photocatalytic water splitting. *ACS Catal.* **2018**, *8*, 3209–3221. [CrossRef]
292. Baker, D.R.; Kamat, P.V. Photosensitization of TiO_2 nanostructures with CdS quantum dots: particulate versus tubular support architectures. *Adv. Funct. Mater.* **2009**, *19*, 805–811. [CrossRef]
293. Chen, X.; Shen, S.; Guo, L.; Mao, S.S. Semiconductor-based photocatalytic hydrogen generation. *Chem. Rev.* **2010**, *110*, 6503–6570. [CrossRef]
294. Kubacka, A.; Fernandez-Garcia, M.; Colon, G. Advanced nanoarchitectures for solar photocatalytic applications. *Chem. Rev.* **2012**, *112*, 1555–1614. [CrossRef]
295. Guo, C.X.; Li, C.M. A self-assembled hierarchical nanostructure comprising carbon spheres and graphene nanosheets for enhanced supercapacitor performance. *Energy Environ. Sci.* **2011**, *4*, 4504–4507. [CrossRef]
296. Tada, H.; Mitsui, T.; Kiyonaga, T.; Akita, T.; Tanaka, K. All-solid-state Z-scheme in CdS–Au–TiO_2 three-component nanojunction system. *Nat. Mater.* **2006**, *5*, 782–786. [CrossRef] [PubMed]
297. Park, H.; Choi, W.; Hoffmann, M.R. Effects of the preparation method of the ternary CdS/TiO_2/Pt hybrid photocatalysts on visible light-induced hydrogen production. *J. Mater. Chem.* **2008**, *18*, 2379–2385. [CrossRef]
298. Oshima, T.; Lu, D.; Ishitani, O.; Maeda, K. Intercalation of highly dispersed metal nanoclusters into a layered metal oxide for photocatalytic overall water splitting. *Angew. Chem.* **2015**, *127*, 2736–2740. [CrossRef]
299. Zhang, Y.; Tang, Z.R.; Fu, X.; Xu, Y.J. Engineering the unique 2D mat of graphene to achieve graphene-TiO_2 nanocomposite for photocatalytic selective transformation: what advantage does graphene have over its forebear carbon nanotube? *ACS Nano* **2011**, *5*, 7426–7435. [CrossRef]
300. Bera, R.; Kundu, S.; Patra, A. 2D hybrid nanostructure of reduced graphene oxide–CdS nanosheet for enhanced photocatalysis. *ACS Appl. Mater. Interfaces* **2015**, *7*, 13251–13259. [CrossRef] [PubMed]
301. Novoselov, K.S.; Geim, A.K.; Morozov, S.V.; Jiang, D.; Zhang, Y.; Dubonos, S.V.; Grigorieva, I.V.; Firsov, A.A. Electric field effect in atomically thin carbon films. *Science* **2004**, *306*, 666–669. [CrossRef] [PubMed]
302. Pacile, D.; Meyer, J.; Girit, Ç.; Zettl, A. The two-dimensional phase of boron nitride: Few-atomic-layer sheets and suspended membranes. *Appl. Phys. Lett.* **2008**, *92*, 133107. [CrossRef]
303. Li, H.; Yin, Z.; He, Q.; Li, H.; Huang, X.; Lu, G.; Fam, D.W.H.; Tok, A.I.Y.; Zhang, Q.; Zhang, H. Fabrication of single-and multilayer MoS_2 film-based field-effect transistors for sensing NO at room temperature. *Small* **2012**, *8*, 63–67. [CrossRef]
304. Late, D.J.; Doneux, T.; Bougouma, M. Single-layer MoSe2 based NH3 gas sensor. *Appl. Phys. Lett.* **2014**, *105*, 233103. [CrossRef]
305. Li, H.; Lu, G.; Wang, Y.; Yin, Z.; Cong, C.; He, Q.; Wang, L.; Ding, F.; Yu, T.; Zhang, H. Mechanical exfoliation and characterization of single-and few-layer nanosheets of WSe_2, TaS_2, and $TaSe_2$. *Small* **2013**, *9*, 1974–1981. [CrossRef] [PubMed]
306. Pezeshki, A.; Hosseini Shokouh, S.H.; Jeon, P.J.; Shackery, I.; Kim, J.S.; Oh, I.K.; Jun, S.C.; Kim, H.; Im, S. Static and dynamic performance of complementary inverters based on nanosheet α-$MoTe_2$ p-channel and MoS_2 n-channel transistors. *ACS Nano* **2016**, *10*, 1118–1125. [CrossRef] [PubMed]

307. Liu, F.; Zheng, S.; He, X.; Chaturvedi, A.; He, J.; Chow, W.L.; Mion, T.R.; Wang, X.; Zhou, J.; Fu, Q.; et al. Highly sensitive detection of polarized light using anisotropic 2D ReS_2. *Adv. Funct. Mater.* **2016**, *26*, 1169–1177. [CrossRef]
308. Dumcenco, D.O.; Kobayashi, H.; Liu, Z.; Huang, Y.S.; Suenaga, K. Visualization and quantification of transition metal atomic mixing in $Mo_{1-x}W_xS_2$ single layers. *Nat. Commun.* **2013**, *4*, 1–5. [CrossRef] [PubMed]
309. Chen, Y.; Xi, J.; Dumcenco, D.O.; Liu, Z.; Suenaga, K.; Wang, D.; Shuai, Z.; Huang, Y.S.; Xie, L. Tunable band gap photoluminescence from atomically thin transition-metal dichalcogenide alloys. *ACS Nano* **2013**, *7*, 4610–4616. [CrossRef]
310. Chen, Y.; Dumcenco, D.O.; Zhu, Y.; Zhang, X.; Mao, N.; Feng, Q.; Zhang, M.; Zhang, J.; Tan, P.H.; Huang, Y.S.; et al. Composition-dependent Raman modes of $Mo_{1-x}W_xS_2$ monolayer alloys. *Nanoscale* **2014**, *6*, 2833–2839.
311. Liu, F.; Zheng, S.; Chaturvedi, A.; Zólyomi, V.; Zhou, J.; Fu, Q.; Zhu, C.; Yu, P.; Zeng, Q.; Drummond, N.D.; et al. Optoelectronic properties of atomically thin ReSSe with weak interlayer coupling. *Nanoscale* **2016**, *8*, 5826–5834. [CrossRef]
312. Goyal, V.; Teweldebrhan, D.; Balandin, A.A. Mechanically-exfoliated stacks of thin films of Bi_2Te_3 topological insulators with enhanced thermoelectric performance. *Appl. Phys. Lett.* **2010**, *97*, 133117. [CrossRef]
313. Shahil, K.; Hossain, M.; Goyal, V.; Balandin, A. Micro-Raman spectroscopy of mechanically exfoliated few-quintuple layers of Bi_2Te_3, Bi_2Se_3, and Sb_2Te_3 materials. *J. Appl. Phys.* **2012**, *111*, 054305.
314. Du, K.z.; Wang, X.z.; Liu, Y.; Hu, P.; Utama, M.I.B.; Gan, C.K.; Xiong, Q.; Kloc, C. Weak van der Waals stacking, wide-range band gap, and Raman study on ultrathin layers of metal phosphorus trichalcogenides. *ACS Nano* **2016**, *10*, 1738–1743. [CrossRef]
315. Buscema, M.; Groenendijk, D.J.; Blanter, S.I.; Steele, G.A.; Van Der Zant, H.S.; Castellanos-Gomez, A. Fast and broadband photoresponse of few-layer black phosphorus field-effect transistors. *Nano Lett.* **2014**, *14*, 3347–3352. [CrossRef]
316. Liu, F.; You, L.; Seyler, K.L.; Li, X.; Yu, P.; Lin, J.; Wang, X.; Zhou, J.; Wang, H.; He, H.; et al. Room-temperature ferroelectricity in $CuInP_2S_6$ ultrathin flakes. *Nat. Commun.* **2016**, *7*, 1–6. [CrossRef] [PubMed]
317. Huang, Y.; Sutter, E.; Shi, N.N.; Zheng, J.; Yang, T.; Englund, D.; Gao, H.J.; Sutter, P. Reliable exfoliation of large-area high-quality flakes of graphene and other two-dimensional materials. *ACS Nano* **2015**, *9*, 10612–10620. [CrossRef] [PubMed]
318. Desai, S.B.; Madhvapathy, S.R.; Amani, M.; Kiriya, D.; Hettick, M.; Tosun, M.; Zhou, Y.; Dubey, M.; Ager, J.W., III; Chrzan, D.; et al. Gold-mediated exfoliation of ultralarge optoelectronically-perfect monolayers. *Adv. Mater.* **2016**, *28*, 4053–4058. [CrossRef] [PubMed]
319. Coleman, J.N.; Lotya, M.; O'Neill, A.; Bergin, S.D.; King, P.J.; Khan, U.; Young, K.; Gaucher, A.; De, S.; Smith, R.J.; et al. Two-dimensional nanosheets produced by liquid exfoliation of layered materials. *Science* **2011**, *331*, 568–571. [CrossRef] [PubMed]
320. Wang, Q.H.; Kalantar-Zadeh, K.; Kis, A.; Coleman, J.N.; Strano, M.S. Electronics and optoelectronics of two-dimensional transition metal dichalcogenides. *Nat. Nanotechnol.* **2012**, *7*, 699–712. [CrossRef]
321. Smith, R.J.; King, P.J.; Lotya, M.; Wirtz, C.; Khan, U.; De, S.; O'Neill, A.; Duesberg, G.S.; Grunlan, J.C.; Moriarty, G.; et al. Large-scale exfoliation of inorganic layered compounds in aqueous surfactant solutions. *Adv. Mater.* **2011**, *23*, 3944–3948. [CrossRef]
322. Coleman, J.N. Liquid exfoliation of defect-free graphene. *Accounts Chem. Res.* **2013**, *46*, 14–22. [CrossRef]
323. Hernandez, Y.; Nicolosi, V.; Lotya, M.; Blighe, F.M.; Sun, Z.; De, S.; McGovern, I.; Holland, B.; Byrne, M.; Gun'Ko, Y.K.; et al. High-yield production of graphene by liquid-phase exfoliation of graphite. *Nat. Nanotechnol.* **2008**, *3*, 563–568. [CrossRef]
324. O'Neill, A.; Khan, U.; Coleman, J.N. Preparation of high concentration dispersions of exfoliated MoS_2 with increased flake size. *Chem. Mater.* **2012**, *24*, 2414–2421. [CrossRef]
325. Feng, J.; Peng, L.; Wu, C.; Sun, X.; Hu, S.; Lin, C.; Dai, J.; Yang, J.; Xie, Y. Giant moisture responsiveness of VS_2 ultrathin nanosheets for novel touchless positioning interface. *Adv. Mater.* **2012**, *24*, 1969–1974. [CrossRef] [PubMed]

326. Zhou, K.G.; Mao, N.N.; Wang, H.X.; Peng, Y.; Zhang, H.L. A mixed-solvent strategy for efficient exfoliation of inorganic graphene analogues. *Angew. Chem.* **2011**, *123*, 11031–11034. [CrossRef]
327. Yi, M.; Shen, Z. A review on mechanical exfoliation for the scalable production of graphene. *J. Mater. Chem. A* **2015**, *3*, 11700–11715. [CrossRef]
328. Paton, K.R.; Varrla, E.; Backes, C.; Smith, R.J.; Khan, U.; O'Neill, A.; Boland, C.; Lotya, M.; Istrate, O.M.; King, P.; et al. Scalable production of large quantities of defect-free few-layer graphene by shear exfoliation in liquids. *Nat. Mater.* **2014**, *13*, 624–630. [CrossRef] [PubMed]
329. Liu, L.; Shen, Z.; Yi, M.; Zhang, X.; Ma, S. A green, rapid and size-controlled production of high-quality graphene sheets by hydrodynamic forces. *Rsc Adv.* **2014**, *4*, 36464–36470. [CrossRef]
330. Yu, J.; Li, J.; Zhang, W.; Chang, H. Synthesis of high quality two-dimensional materials via chemical vapor deposition. *Chem. Sci.* **2015**, *6*, 6705–6716. [CrossRef]
331. Jones, A.C.; Hitchman, M.L. Overview of chemical vapour deposition. *Chem. Vapor. Depos.* **2009**, *1*, 1–36.
332. Somani, P.R.; Somani, S.P.; Umeno, M. Planer nano-graphenes from camphor by CVD. *Chem. Phys. Lett.* **2006**, *430*, 56–59. [CrossRef]
333. Pollard, A.; Nair, R.; Sabki, S.; Staddon, C.; Perdigao, L.; Hsu, C.; Garfitt, J.; Gangopadhyay, S.; Gleeson, H.; Geim, A.; et al. Formation of monolayer graphene by annealing sacrificial nickel thin films. *J. Phys. Chem. C* **2009**, *113*, 16565–16567. [CrossRef]
334. Reina, A.; Jia, X.; Ho, J.; Nezich, D.; Son, H.; Bulovic, V.; Dresselhaus, M.S.; Kong, J. Large area, few-layer graphene films on arbitrary substrates by chemical vapor deposition. *Nano Lett.* **2009**, *9*, 30–35. [CrossRef]
335. Kim, G.; Jang, A.R.; Jeong, H.Y.; Lee, Z.; Kang, D.J.; Shin, H.S. Growth of high-crystalline, single-layer hexagonal boron nitride on recyclable platinum foil. *Nano Lett.* **2013**, *13*, 1834–1839. [CrossRef] [PubMed]
336. Zhao, Y.; Luo, X.; Zhang, J.; Wu, J.; Bai, X.; Wang, M.; Jia, J.; Peng, H.; Liu, Z.; Quek, S.Y.; et al. Interlayer vibrational modes in few-quintuple-layer Bi_2Te_3 and Bi_2Se_3 two-dimensional crystals: Raman spectroscopy and first-principles studies. *Phys. Rev. B* **2014**, *90*, 245428. [CrossRef]
337. Zheng, W.; Xie, T.; Zhou, Y.; Chen, Y.; Jiang, W.; Zhao, S.; Wu, J.; Jing, Y.; Wu, Y.; Chen, G.; et al. Patterning two-dimensional chalcogenide crystals of Bi_2 Se_3 and In_2Se_3 and efficient photodetectors. *Nat. Commun.* **2015**, *6*, 1–8. [CrossRef] [PubMed]
338. Mannix, A.J.; Zhou, X.F.; Kiraly, B.; Wood, J.D.; Alducin, D.; Myers, B.D.; Liu, X.; Fisher, B.L.; Santiago, U.; Guest, J.R.; et al. Synthesis of borophenes: Anisotropic, two-dimensional boron polymorphs. *Science* **2015**, *350*, 1513–1516. [CrossRef]
339. Gogotsi, Y. Chemical vapour deposition: Transition metal carbides go 2D. *Nat. Mater.* **2015**, *14*, 1079–1080. [CrossRef]
340. Xu, C.; Wang, L.; Liu, Z.; Chen, L.; Guo, J.; Kang, N.; Ma, X.L.; Cheng, H.M.; Ren, W. Large-area high-quality 2D ultrathin Mo_2C superconducting crystals. *Nat. Mater.* **2015**, *14*, 1135–1141. [CrossRef]
341. Fleurence, A.; Friedlein, R.; Ozaki, T.; Kawai, H.; Wang, Y.; Yamada-Takamura, Y. Experimental evidence for epitaxial silicene on diboride thin films. *Phy. Rev. Lett.* **2012**, *108*, 245501. [CrossRef]
342. Zhan, Y.; Liu, Z.; Najmaei, S.; Ajayan, P.M.; Lou, J. Large-area vapor-phase growth and characterization of MoS_2 atomic layers on a SiO_2 substrate. *Small* **2012**, *8*, 966–971. [CrossRef]
343. Zhang, Y.; Zhang, Y.; Ji, Q.; Ju, J.; Yuan, H.; Shi, J.; Gao, T.; Ma, D.; Liu, M.; Chen, Y.; et al. Controlled growth of high-quality monolayer WS_2 layers on sapphire and imaging its grain boundary. *ACS Nano* **2013**, *7*, 8963–8971. [CrossRef]
344. Wang, X.; Gong, Y.; Shi, G.; Chow, W.L.; Keyshar, K.; Ye, G.; Vajtai, R.; Lou, J.; Liu, Z.; Ringe, E.; et al. Chemical vapor deposition growth of crystalline monolayer $MoSe_2$. *ACS Nano* **2014**, *8*, 5125–5131. [CrossRef]
345. Docherty, C.J.; Parkinson, P.; Joyce, H.J.; Chiu, M.H.; Chen, C.H.; Lee, M.Y.; Li, L.J.; Herz, L.M.; Johnston, M.B. Ultrafast transient terahertz conductivity of monolayer MoS_2 and WSe_2 grown by chemical vapor deposition. *ACS Nano* **2014**, *8*, 11147–11153. [CrossRef] [PubMed]
346. Zhang, M.; Zhu, Y.; Wang, X.; Feng, Q.; Qiao, S.; Wen, W.; Chen, Y.; Cui, M.; Zhang, J.; Cai, C.; et al. Controlled synthesis of ZrS_2 monolayer and few layers on hexagonal boron nitride. *J. Am. Chem. Soc.* **2015**, *137*, 7051–7054. [CrossRef] [PubMed]

347. Keyshar, K.; Gong, Y.; Ye, G.; Brunetto, G.; Zhou, W.; Cole, D.P.; Hackenberg, K.; He, Y.; Machado, L.; Kabbani, M.; et al. Chemical vapor deposition of monolayer rhenium disulfide (ReS_2). *Adv. Mater.* **2015**, *27*, 4640–4648. [CrossRef]
348. Liu, L.; Park, J.; Siegel, D.A.; McCarty, K.F.; Clark, K.W.; Deng, W.; Basile, L.; Idrobo, J.C.; Li, A.P.; Gu, G. Heteroepitaxial growth of two-dimensional hexagonal boron nitride templated by graphene edges. *Science* **2014**, *343*, 163–167. [CrossRef] [PubMed]
349. De Parga, A.V.; Calleja, F.; Borca, B.; Passeggi Jr, M.; Hinarejos, J.; Guinea, F.; Miranda, R. Periodically rippled graphene: Growth and spatially resolved electronic structure. *Phy. Rev. Lett.* **2008**, *100*, 056807. [CrossRef]
350. Li, M.Y.; Shi, Y.; Cheng, C.C.; Lu, L.S.; Lin, Y.C.; Tang, H.L.; Tsai, M.L.; Chu, C.W.; Wei, K.H.; He, J.H.; et al. Epitaxial growth of a monolayer WSe_2-MoS_2 lateral p-n junction with an atomically sharp interface. *Science* **2015**, *349*, 524–528. [CrossRef]
351. Yu, Y.; Hu, S.; Su, L.; Huang, L.; Liu, Y.; Jin, Z.; Purezky, A.A.; Geohegan, D.B.; Kim, K.W.; Zhang, Y.; et al. Equally efficient interlayer exciton relaxation and improved absorption in epitaxial and nonepitaxial MoS_2/WS_2 heterostructures. *Nano Lett.* **2015**, *15*, 486–491. [CrossRef]
352. Heo, H.; Sung, J.H.; Jin, G.; Ahn, J.H.; Kim, K.; Lee, M.J.; Cha, S.; Choi, H.; Jo, M.H. Rotation-Misfit-Free Heteroepitaxial Stacking and Stitching Growth of Hexagonal Transition-Metal Dichalcogenide Monolayers by Nucleation Kinetics Controls. *Adv. Mater.* **2015**, *27*, 3803–3810. [CrossRef]
353. Duesberg, G.S. Heterojunctions in 2D semiconductors: A perfect match. *Nat. Mater.* **2014**, *13*, 1075–1076. [CrossRef]
354. Li, M.Y.; Chen, C.H.; Shi, Y.; Li, L.J. Heterostructures based on two-dimensional layered materials and their potential applications. *Mater. Today* **2016**, *19*, 322–335. [CrossRef]
355. Shi, Z.T.; Kang, W.; Xu, J.; Sun, Y.W.; Jiang, M.; Ng, T.W.; Xue, H.T.; Denis, Y.; Zhang, W.; Lee, C.S. Hierarchical nanotubes assembled from MoS_2-carbon monolayer sandwiched superstructure nanosheets for high-performance sodium ion batteries. *Nano Energy* **2016**, *22*, 27–37. [CrossRef]
356. Xie, J.; Zhang, J.; Li, S.; Grote, F.; Zhang, X.; Zhang, H.; Wang, R.; Lei, Y.; Pan, B.; Xie, Y. Controllable disorder engineering in oxygen-incorporated MoS_2 ultrathin nanosheets for efficient hydrogen evolution. *J. Am. Chem. Soc.* **2013**, *135*, 17881–17888. [CrossRef]
357. Cai, L.; He, J.; Liu, Q.; Yao, T.; Chen, L.; Yan, W.; Hu, F.; Jiang, Y.; Zhao, Y.; Hu, T.; et al. Vacancy-induced ferromagnetism of MoS_2 nanosheets. *J. Am. Chem. Soc.* **2015**, *137*, 2622–2627. [CrossRef] [PubMed]
358. Song, H.J.; You, S.; Jia, X.H.; Yang, J. MoS_2 nanosheets decorated with magnetic Fe_3O_4 nanoparticles and their ultrafast adsorption for wastewater treatment. *Ceram. Int.* **2015**, *41*, 13896–13902. [CrossRef]
359. Jeong, S.; Yoo, D.; Jang, J.t.; Kim, M.; Cheon, J. Well-defined colloidal 2-D layered transition-metal chalcogenide nanocrystals via generalized synthetic protocols. *J. Am. Chem. Soc.* **2012**, *134*, 18233–18236. [CrossRef] [PubMed]
360. Gupta, A.; Sakthivel, T.; Seal, S. Recent development in 2D materials beyond graphene. *Prog. Mater. Sci.* **2015**, *73*, 44–126. [CrossRef]
361. Wang, L.; Sun, C.; Xu, L.; Qian, Y. Convenient synthesis and applications of gram scale boron nitride nanosheets. *Catal. Sci. Technol.* **2011**, *1*, 1119–1123. [CrossRef]
362. Zhang, N.; Liu, X.; Yi, R.; Shi, R.; Gao, G.; Qiu, G. Selective and controlled synthesis of single-crystalline yttrium hydroxide/oxide nanosheets and nanotubes. *J. Phys. Chem. C* **2008**, *112*, 17788–17795. [CrossRef]
363. Yang, S.; Gong, Y.; Liu, Z.; Zhan, L.; Hashim, D.P.; Ma, L.; Vajtai, R.; Ajayan, P.M. Bottom-up approach toward single-crystalline VO_2-graphene ribbons as cathodes for ultrafast lithium storage. *Nano Lett.* **2013**, *13*, 1596–1601. [CrossRef]
364. Shen, J.; Dong, P.; Baines, R.; Xu, X.; Zhang, Z.; Ajayan, P.M.; Ye, M. Controlled synthesis and comparison of $NiCo_2S_4$/graphene/2D TMD ternary nanocomposites for high-performance supercapacitors. *Chem. Commun.* **2016**, *52*, 9251–9254. [CrossRef]
365. Shen, J.; Ji, J.; Dong, P.; Baines, R.; Zhang, Z.; Ajayan, P.M.; Ye, M. Novel $FeNi_2S_4$/TMD-based ternary composites for supercapacitor applications. *J. Mater. Chem. A* **2016**, *4*, 8844–8850. [CrossRef]
366. Meng, F.; Hong, Z.; Arndt, J.; Li, M.; Zhi, M.; Yang, F.; Wu, N. Visible light photocatalytic activity of nitrogen-doped $La_2Ti_2O_7$ nanosheets originating from band gap narrowing. *Nano Res.* **2012**, *5*, 213–221. [CrossRef]

367. Ghuman, K.K.; Hoch, L.B.; Szymanski, P.; Loh, J.Y.; Kherani, N.P.; El-Sayed, M.A.; Ozin, G.A.; Singh, C.V. Photoexcited surface frustrated Lewis pairs for heterogeneous photocatalytic CO_2 reduction. *J. Am. Chem. Soc.* **2016**, *138*, 1206–1214. [CrossRef] [PubMed]
368. Hoch, L.B.; Szymanski, P.; Ghuman, K.K.; He, L.; Liao, K.; Qiao, Q.; Reyes, L.M.; Zhu, Y.; El-Sayed, M.A.; Singh, C.V.; et al. Carrier dynamics and the role of surface defects: Designing a photocatalyst for gas-phase CO_2 reduction. *Proc. Natl. Acad. Sci. USA* **2016**, *113*, E8011–E8020. [CrossRef] [PubMed]